The Dissertation Committee for Manuj Nahar Certifies that this is the approved version of the following dissertation:

Highly Conductive, Nanoparticulate Thick Films Processed at Low Processing Temperatures

Committee:

Desiderio Kovar, Supervisor

Paulo J. Ferreira

Michael F. Becker

John W. Keto

David L. Bourell

Highly Conductive, Nanoparticulate Thick Films Processed at Low Processing Temperatures

by

Manuj Nahar, B.Tech; M.S.E.

Dissertation

Presented to the Faculty of the Graduate School of

The University of Texas at Austin

in Partial Fulfillment

of the Requirements

for the Degree of

Doctor of Philosophy

The University of Texas at Austin

August 2012

To my parents

Acknowledgements

I was very lucky to have Dr. Desiderio Kovar as my advisor through this project. Dr. Kovar's constant encouragement, patience, his ability to motivate me when things were not going right, his knowledge of the phenomenon of sintering, and his dedication as an advisor to help me improve are extraordinary. Dr. John W. Keto is a great engineer who also happens to be a great physicist. He was a constant source of new ideas, provided me with a thorough critique of my research, and motivated me to build things. Dr. Michael F. Becker's office blackboard is where many of the solutions to my research problems came together. Discussions with Dr. Bourell regarding sintering and with Dr. Paulo Ferriera for analyzing microscopy results were invaluable. I would also like to thank Dr. Lew Raebenberg and Dr. John B. Goodenough for their discussion on topics unrelated to this work. Jack Clifford has developed in me a love for the machine shop. Mike Ronalter and Adam built beautiful glass chambers for my feeder. Dr. J P Zhou, taught me how to use the TEM. I cannot thank Kris Gleason enough, for the numerous discussions I had with him regarding science and many more pitchers that I had with him at Crown. Ignacio Gallardo was the first to teach me how to use LAM and Nathan Erickson has been very generous in sharing his knowledge. I would like to thank Michael Asoro for being a good colleague in our shared field of sintering and a good friend. For their patience and understanding I thank the present LAM group - Michael Gammage, Guilluame Nosieu, Jean – Gil, and Alex.

I have learnt much more than science in the last 5 years, and for that I would like to thank – Beth Hood, Daven Rauchwerk, Ari Turrentine, Carl Semen, Daniel Carney, Sohaib Alam, Mashal Awais, Iliana Marie Lopez, Alejandra Cerna Rios, Robert Morgan,

Dhruv Mohta, Achint Aggarwal, Vijo Varkey, Anuj Aggarwal, Melissa Rodriguiez, Meagan Wooley, Garima, Ruby, Katie, Markita, Arindam Sarkar, Nishesh Mehta, Ben, Matt, Luke, and Simon. James Mckalske and Camille Jouv for teaching me the guitar. To Claire Davis, I owe a lot. Merci à Claire, pour être une amie, pour la fête du thé, pour le français, and for talking to me about things and for being around for two years.

Thank you Ma, dad, dada, and dadi.

Highly Conductive, Nanoparticulate Thick Films Achieved at Low Processing Temperatures

Manuj Nahar, Ph.D.

The University of Texas at Austin, 2012

Supervisor: Desiderio Kovar

Applications such as device interconnects require thick, patterned films that are currently produced by screen printing pastes consisting of metallic particles and subsequently sintering the films. For Ag films, achieving adequate electrical conductivity requires sintering temperatures in excess of 700˚C. New applications require highly conductive films that can be processed at lower processing temperatures. Although sintering temperatures have been reduced by utilizing finer nanoparticles (NPs) in place of conventional micron-size particles (MPs), realization of theoretically achievable sintering kinetics is yet to be achieved. The major factors that inhibit NP sintering are 1) the presence of organic molecules on the NP surfaces, 2) the dominance of the non-densifying surface diffusion over grain boundary or lattice diffusion 3) agglomeration of NPs, and 4) low initial density of the NPs. Here, we report a film fabrication technique that is capable of eliminating these deleterious factors and produces near fully dense Ag films that exhibit an order of magnitude higher conductivity when compared to other film fabrication techniques at processing temperatures of 150 – 250 °C. The observed results establish the benefits of NP diffusion kinetics to be far more profound when the

deleterious factors to sintering are eliminated. The sintering behavior exhibits two distinct temperature regimes – one above 150 °C where grain boundary diffusion-dominated densification is dominant and one below 100 °C where surface diffusion-dominated coarsening is dominant. An analytical model is developed by fitting the experimental data to the existing models of simultaneous densification and grain growth, and combining this model with existing models of the dependence of conductivity on grain boundary scattering and pore scattering. The combined model successfully describes the evolution of density, grain size and conductivity of nanoparticulate films as a function of annealing treatment, with reasonable accuracy. The model was also used to evaluate the effect of initial NP size and initial relative density of films on the final sintered properties and conductivity of films.

Table of Contents

List of Tables ..... **xi**
List of Figures ..... **xii**
Chapter 1: Introduction **1**
1.1 Motivation 1
1.2 Conventional Approaches 1
1.2.1 Inkjet Printing 2
1.2.2 Dip Pen Nanolithography 3
1.2.3 Aerosol-Based Methods 3
1.3 Laser Ablation of Microparticle Aerosol (LAMA) Process 4
1.4 Objectives and Scope 5
Chapter 2: Background **6**
2.1 Factors that influence conductivity in Conductors 6
2.1.1 Models for calculating the effect of grain boundary and pore scattering on conductivity .. 7
2.2 Densification vs Coarsening 9
2.3 Sintering Mechanisms 11
2.4 Diffusivity 13
2.5 Surface Diffusion and Grain Boundary Diffusion 15
2.6 Stages of Sintering 18
2.7 Grain Growth 19
2.8 Simultaneous Densification and grain growth 23
2.9 Annealing Treatment 25
2.10 Factors that influence sintering 27
Chapter 3: Experimental Procedures **31**
3.1 Deposition Procedure 31
3.1.1 Aerosol Feeding and Detection Setup 32
3.1.1.1 Control of Microparticle Feed Rate 38
3.1.2 Laser ablation cell and the optical setup 39
3.1.3 Residual MP separation using a virtual impactor 42
3.1.4 Supersonic impaction chamber 43
3.2 Post-Deposition Annealing 44
3.3 Area Calculations 45
3.4 Density measurements 45
3.5 Conductivity Measurements 46
3.6 Microscopy 46
3.7 Grain Size Measurements 46
Chapter 4: General Characteristics of the Lines **47**
4.1 Influence of Carrier Gas 47
4.1.1 Nanoparticle Morphology 47
4.1.2 Nanoparticle Morphology in Films 50
4.1.2 Line Morphology 53
4.4 Influence of Feed Rate 54
4.4.1 Nanoparticle Morphology 54
4.4.2 Influence of MP feed rate on macroscopic features of the deposits 57
4.5 Influence of Number of Passes and Deposition Speed 59
4.6 Delamination of Films 60
4.7 Films patterned on Plastic and Paper 63
Chapter 5: Influence of Annealing Treatment **65**
5.1 Effect of Rapid thermal Annealing 66
5.1.1 Microstructure 66

5.1.2 Density 71
5.1.3 Conductivity 73
5.2 Inference on Diffusion Mechanisms 74
5.3 Sintering Kinetics in Grain Boundary Diffusion Dominated Regime 75
5.3.1 Density 76
5.3.2 Conductivity 76
5.4 Sintering Kinetics in the Surface Diffusion Dominant Regime 77
5.4.1 Microstructure 77
5.4.2 Density 79
5.4.3 Conductivity 79
5.5 Two-Step Annealing Treatment 80
5.9 Conclusions 83
Chapter 6:Modeling 85
6.1 Dependence of Conductivity on Density and Grain Size 86
6.2 Dependence of Grain Size and Density on Annealing Temperature and Time 92
6.2.1 Rate of Grain Growth 92
6.2.2 Rate of Densification 94
6.2.3 Grain Growth – Density Trajectory 95
6.3 Dependence of Conductivity on Annealing Treatment 100
6.4 Results of the model 100
6.4.1 Effect of Rapid Thermal Annealing 100
6.4.2 Effect of Two-step Annealing Treatment 108
6.4.3 Influence of NP size 110
6.4.5 Effect of Initial Density 113
6.5 Conclusions 116
Chapter 7: Effect of Agglomeration 118
7.1 Microstructure 119
7.2 Density 122
7.3 Conductivity 124
7.4 Conclusions 125
Chapter 8: Comparative studies with low initial density films consisting of larger NPs 126
8.2 Influence of Temperature 126
8.2.1 Microstructure 127
8.2.2 Density 130
8.2.3 Conductivity 131
8.3 Conclusions 131
Chapter 9: Conclusions 133
Chapter 10: Future Work 136
Appendix A 138
Appendix B 143
References 176
Vita 188

List of Tables

Table 1: Grain growth exponent m for different diffusion mechanisms 22
Table 2: Experimental data used to find R in equation 88
Table 3: D_{gb} values obtained from extrapolations of Guy 96
Table 4: Values of D_s determined in this work at temperatures of interest 98
Table 5: Comparison of Properties of films deposited in He and Ar carrier gas using the direct write LAMA process. 132

List of Figures

Figure 1: Effects of extreme cases of only coarsening (increase in grain size with no change in density) and only densification (reduction in porosity with no change in grain size) on the final microstructure. 10
Figure 2: Schematic representation of six distinct diffusion mechanisms that can contribute to the sintering of crystalline particles. Redrawn from Ref. 12
Figure 3: Published values on diffusivity of silver. Reprinted from Ref. 33. 14
Figure 4: Schematic showing the conventional densification curve of a powder compact and three stages of sintering. Redrawn from Ref. 18
Figure 5: Schematic of grain growth in less dense solids (a) Initial stage, (b) The two sphere system has shrunk and the neck region is pinned, the point of minimum cross section area of the neck, (c) Unpinning stage. Redrawn from Ref. 47. 21
Figure 6: Temperature regimes with different dominant diffusion mechanisms 25
Figure 7: Schematic of the direct write setup 32
Figure 8: Fluidized bed aerosol feeder to aerosolize the MPs. Reprinted from Ref. 26.. 33
Figure 9: Design of the double virtual impactor. Reprinted from Ref. 26. 34
Figure 10 SEM micrograph of feedstock MPs a) before, and b) after the double virtual impactor. The MPs were collected for the same amount of time in both cases. 36
Figure 11: Aerosol Detector. Reprinted from Ref. 26. 37
Figure 12: MP feed rate data vs time at feed rates of a) 10 mg/hr, b) 20 mg/hr, c) 50 mg/hr 39
Figure 13: Drawing showing exploded view of the laser ablation cell (nozzle assembly and horn cell). Reprinted from Ref. 41
Figure 14: Skimmer and virtual impactor assembly. Reprinted from Ref. 64. 43
Figure 15: Influence of carrier gas on NP morphology a) He as the carrier gas, b) Ar as the carrier gas. 48
Figure 16: TEM images of NPs that contain twins. 49
Figure 17: TEM images of films deposited in a) He carrier gas and b) Ar carrier gas 52
Figure 18: Plan-view optical micrograph of a line produced in He carrier gas 53
Figure 19: Cross-sectional profiles of films deposited using He and Ar as the carrier gasses 54
Figure 20:TEM images of agglomerates produced in a) He and b) Ar, produced at a MP feed rate of 50 mg/hr 57
Figure 21: Plan-view optical micrographs of Ag lines produced at feed rates of a) 10 mg/hr, b) 20 mg/hr, and c) 50 mg/hr 59
Figure 22: Top and bottom profiles of a line obtained using an optical profilometer after annealing showing that the bottom profile (red) lifted off the surface of the substrate as result of delamination 60
Figure 23: SEM micrograph of line after annealing showing a region near the center of the profile where delamination is apparent 61

Figure 24: SEM image of a line that was deposited on a masked substrate, annealed and then subsequently brushed to reveal which regions delaminated 62
Figure 25: SEM micrograph of the cross-section of a wide line that survived the industry standard scotch tape test..... 63
Figure 26: Picture of films made on a) thin paper, b) plastic 64
Figure 27: Plan-view microstructures of lines a) as-deposited and rapid thermally annealed at b) 100 ^{o}C, c) 125 ^{o}C, d) 150 ^{o}C, e) 200 ^{o}C, and f) 250 ^{o}C 69
Figure 28: Grain size vs Annealing Temperature for line deposited in He carrier gas 71
Figure 29: Density versus annealing temperature for lines deposited in He carrier gas... 73
Figure 30: Conductivity versus annealing temperature for lines deposited in He carrier gas 74
Figure 31: Conductivity versus annealing time for films annealed at 150 ^{o}C 76
Figure 32: Plan-view SEM images of lines heated at 100 ˚C for a) 5 min, b) 1 hr, and c) 16.5 hrs..... 79
Figure 33: % Conductivity relative to bulk silver versus annealing time for lines annealed at 100 ^{o}C, for a) 0 sec, b) 5 min, c) 60 min, d) 990 min. 80
Figure 34: a) Plan view microstructure of a line after a two-step annealing treatment where it was initially annealed at 100 ^{o}C for 5 min and subsequently annealed at 150 ^{o}C for 5 min. b) Plan view microstructure of a line give a single rapid thermal annealing treatment at 150 ^{o}C for 5 min,..... 82
Figure 35: Comparison of the predicted conductivity using R = 0.554, and measured conductivity..... 89
Figure 36: Plot of relative density (expressed as % conductivity of bulk silver) versus grain size with constant conductivity contours superimposed ranging from 30 – 80% of the bulk conductivity of Ag 91
Figure 37: $ln(D_s)$ vs $1000/T$ plotted for estimated values of D_s. 97
Figure 38: D_s obtained in this work (green). Also plotted are D_s and D_{gb} (black and red, respectively) from Guy[33] 99
Figure 39: Predictions of the model for films annealed at 100 ^{o}C for 5 min. 101
Figure 40: Predictions of the model for films annealed at 100 ^{o}C for 5 min. 102
Figure 41: Predictions of the model for films annealed at 150 ^{o}C for 5 min. 103
Figure 42: Predictions of the model for films annealed at 200 ^{o}C for 5 min. 104
Figure 43: Predictions of the model for films annealed at 250 ^{o}C for 5 min. 105
Figure 44: Comparison between the predicted and experimentally measured values of a) density, b) grain-size, and c) conductivity 108
Figure 45: Predictions of the model for a two-step annealing treatment. 109
Figure 46: Predictions of the model for annealing at 150 ^{o}C with an initial particle size of 60 nm and initial fractional density of 0.7. 111
Figure 47: Predictions of the model for annealing at 150 ^{o}C with initial particle size of 6 nm and an initial fractional density of a) 0.6, and b) 0.5. 115
Figure 48: Plan-view microstructures of lines annealed at 150 ^{o}C. MP feed rates of a) 50 mg/hr, b) 20 mg/hr, c) 10 mg/hr 121
Figure 49: Grain size versus feed rate for films annealed at 150 ^{o}C..... 122

Figure 50: Dependences of the densities of as-deposited and annealed films on MP feed rates 123
Figure 51: Dependences of feed rate on the conductivities of as-deposited and annealed films 124
Figure 52: Plan-view microstructures of lines deposited in Ar as the carrier gas a) as-deposited, and annealed at b) 150 ^{o}C, c) 200 ^{o}C, d) 250 ^{o}C 128
Figure 53: Comparison of grain sizes of sintered films produced using He and Ar carrier gas 129
Figure 54: Comparison of conductivities of lines deposited in He and Ar..... 131
Figure 55: χ^2 vs R..... 139
Figure 56: χ^2 vs Kpre 141

Chapter 1: Introduction

1.1 MOTIVATION

Many new applications[1,2,3] for electronics require inexpensive, temperature-sensitive, non-planar, or foldable substrates[4,5]. Applications for such substrates include high frequency antennas[6] and packaging for temperature-sensitive MEMS devices[7]. These applications contain thick films of patterned conducting lines (>100 μm). Achieving high conductivity by conventional processing routes for producing thick films lines requires sintering at temperatures in excess of 700 ^{o}C[8]. Many temperature-sensitive substrates can withstand temperatures of no higher than 250 ^{o}C, and thus, strategies for reducing the sintering temperatures are needed. While attempts to reduce the sintering temperatures by utilizing finer nanoparticles (NPs) in place of conventional micron-sized particles have been made[9,10,11], realization of theoretically achievable sintering kinetics is yet to be achieved. The realization of lower temperature sintering to achieve adequate conductivity would relax constraints on the kind of substrates that can be utilized and increase applications where lower cost and flexible substrates would be advantageous.

1.2 CONVENTIONAL APPROACHES

The traditional method for depositing thick films is by screen printing of pastes that contain micron-sized powders of metallic materials[12]. The pastes, are then dried and

heated to pyrolyze organic additives and then sintered to bond the metallic powder particles into a conducting lines. Direct write technologies to fabricate conductive lines have attracted a lot of attention in the recent years as an alternative to screen printing. Here we discuss relevant ink-[13], paste-[14] and aerosol-based[15] conventional direct write technologies that have been studied recently.

1.2.1 Inkjet Printing

Traditional ink jet printing works by pushing an ink that consists of a suspension of particles in a polymer solution out of a nozzle to form droplets, either by heating the ink or applying pressure. The nozzle determines the desired position of the droplet and by controlling the relative movement between the nozzle and the substrate, patterned films can be produced. The droplet volume determines the pixel resolution; for example a droplet of 10 pL gives a pixel resolution of 25 μm[16]. Silver particles are used in the inks to ensure good conductivity, and because of its relatively low cost for a noble metal that is resistant to oxidation under ambient conditions. The inks generally contain organic dispersants to prevent the particles from agglomerating and for modifying the surface tension and viscosity of the ink which are critical for achieving controlled jetting. Although conducting organics can be used as a component in the ink to achieve some level of conductivity, the development of metallic-like conductivities requires an annealing process after depositions to remove the organic dispersants and to promote sintering between the powder particles.

1.2.2 Dip Pen Nanolithography

Dip pen nanolithography (DPN)[17,18] uses the same principle as was used by the old-fashioned dip pen that was used in schoolrooms in the 19th century. In DPN, a reservoir of ink is stored on top of a scanning probe tip, which is rastered across the substrate to produce patterned lines. Compared to inkjetting, DPN has the advantage of being more versatile in the choice of ink or the substrate and is capable of patterning complex structures[19]. DPN is however an inherently slow technique[19]. Similar to inkjet inks, the inks for DPN also contain organic dispersants, which need to be removed for applications requiring high conductivity.

1.2.3 Aerosol-Based Methods

Hayashi *et al*.[20,21,22] developed the Gas Deposition Method (GDM), which generates a NP aerosol (mean size ~ 60 nm) by evaporation of material from a hot source. The aerosol is accelerated via a pressure difference through an orifice to impact the nanoparticles onto a substrate and form a film. GDM has the advantage of producing pure NPs that are not coated with organic dispersants. However, it is not clear if the NPs in this process are agglomerated or not. If the NPs are agglomerated, they would exhibit lower sinterability on post deposition processing.

Akedo *et al.*[15] modified the GDM method to use commercially available, micron- and sub-micron sized particles rather than an evaporative source and named this process

the Aerosol Deposition Method (ADM). The ADM process has demonstrated the capability to produce high density patterned thick films.

1.3 LASER ABLATION OF MICROPARTICLE AEROSOL (LAMA) PROCESS

The LAMA process was invented by Becker *et al.*[23] at the University of Texas at Austin. The process relies on generating a shockwave in a microparticle (MP) aerosol using an excimer laser, to convert it to a NP aerosol. The NP aerosol is then supersonically impacted onto a substrate and patterned structures are formed by moving the substrate relative to the nozzle. Albert *et al.*[24] and Huang *et al.*[25] showed the capability of the LAMA process to produce uniformly sized, small NPs that were free of organic dispersants and demonstrated that the process is a promising candidate as a direct write technique to deposit highly conductive lines. Gleason *et al.*[26] showed that the agglomeration behavior of NPs produced by LAMA offered a possibility to further control the characteristics and hence the final properties of the deposited films.

The LAMA process has several advantages over the conventional ink and paste methods, or other aerosol based methods. The unique features of the LAMA process can be summarized as follows:

1. The NPs produced are free of organic dispersants and thus there is no need for post-deposition pyrolysis of the organics.
2. The process is capable of producing small NPs with a narrow size distribution.
3. The process is capable of controlling the state of agglomeration of NPs.

The LAMA process is utilized in this work for fabricating conductive lines and will be discussed in more detail in the sections that follow.

1.4 OBJECTIVES AND SCOPE

The aim of this dissertation is to study the factors necessary to produce patterned, highly conductive films at low processing temperatures using a direct write process. The key to achieving high conductivity lies in the understanding of the sintering behavior of nanoparticulate films. The sintering behavior of nanoparticulate films is affected by several factors such as NP size, NP agglomeration, film density and the operating sintering mechanisms. An understanding and ultimately control of these factors will allow us to obtain films with favorable properties.

Chapter 2: Background

In this chapter, the background information useful to understand the research work is discussed. The factors that influence conductivity and sintering are explained and form the basis for this work. The fundamentals of the sintering phenomenon including the stages of sintering, diffusion mechanisms, diffusion parameters and grain growth are also explained. The aim of this chapter is to provide an understanding of the design of experiments, the observed results, and the inferences made from this research.

2.1 Factors that influence conductivity in Conductors

The resistance to the flow of electrons in a material arises from the scattering of electrons from phonons, defects, impurities, surfaces, grains and pores[27]. While electron-phonon scattering is a material property that determines the intrinsic conductivity of the material, the remaining scattering sources can be manipulated to modify the conductivity of the material.

In the LAMA process, the composition of the produced NPs is the same as the feedstock MPs. Thus, if high purity feedstock is used, the effect of impurities can be neglected. TEM observations of the NPs produced by the LAMA process in the present and previous work show no evidence of dislocations but some twinning is apparent. To simplify the analysis, the effect of scattering of electrons by defects is neglected. Fuchs and Sondheimer[28] showed that the effect of surface scattering of electrons on

conductivity is significant only for thin films and can also be neglected for the thick films discussed in this work.

The major scattering sources affecting the conductivity of films studied in this work are assumed to be grain boundaries and pores. The effect of grain boundary scattering is particularly important when the grain size decreases because of the increase in the fraction of interfaces. For example, the fraction of atoms that lie on interfaces is ~ 50% when the grain size reaches 5 nm. The pores act as scattering centers that are similar to surfaces and thus also can have a significant impact on the conductivity of films.

2.1.1 Models for calculating the effect of grain boundary and pore scattering on conductivity

Maydas and Shatzkes[29] proposed a theoretical model to describe the dependence of electrical conductivity of films on grain boundary scattering. The detailed derivation of the model is lengthy and can be found in Ref [29]. To summarize, the model assumes that grain boundaries are all perpendicular to the plane of the film and partially reflect electrons. The electron reflectivity, *R*, in their model represents the probability for an electron at the Fermi surface to cross a potential barrier caused by the grain boundary and its value is determined by the shape of the Fermi surface and by the potential at the grain boundary. The ratio of grain boundary to bulk conductivity is given by

$$\frac{\sigma_{gb}}{\sigma_{bulk}} = 3[\frac{1}{3} - \frac{1}{2}\alpha + \alpha^2 - \alpha^2 \ln(1 + \frac{1}{\alpha})] \qquad \text{Equation 1}$$

$$\alpha = \frac{\lambda_\infty}{D}\left[\frac{R}{R-1}\right] \qquad \text{Equation 2}$$

where,

σ_{gb} is the grain boundary conductivity,

σ_{bulk} is the bulk conductivity,

λ is the mean free path of electrons in the medium ,

R is the reflection coefficient, and

D is the grain size

R can be obtained by fitting experimental data and gives a measure of the grain boundary scattering.

The contribution of pore scattering to conductivity can be evaluated by applying the Bruggeman effective medium approximation[30] to the conductivity. The effective medium conductivity is given by

$$f_v \left[\frac{1-\sigma_{EM}}{1-2\sigma_{EM}}\right] = (f_v - 1)\left[\frac{\sigma_{gb}-\sigma_{EM}}{\sigma_{gb}+2\sigma_{EM}}\right] \qquad \text{Equation 3}$$

where,

f_v is the void fraction,

σ_{gb} is the grain boundary conductivity, and

σ_{EM} is the effective medium conductivity

The derivation of the approximation is given in Ref [30]. The above two models can be used to calculate the conductivity in thick films that contain porosity.

Since the motivation of this work is to achieve high conductivity, we have chosen to produce films of silver, a high intrinsic conductivity, semi-noble material. The challenge for achieving high conductivity at low processing temperatures lies in minimizing pore scattering and grain boundary scattering i.e. achieving adequate densification and grain growth at those processing temperatures. Both densification and grain growth are directly related to the sintering behavior of the constituent particles. While NPs have shown favorable sintering behavior when compared to their conventional micron-sized counterparts[31], the realization theoretical sintering kinetics is yet to be achieved. The realization of theoretical sintering kinetics of NPs is thus the major consideration in achieving high conductivity at low processing temperatures in thick films.

2.2 DENSIFICATION VS COARSENING

The final properties of a compact of powder, post annealing mainly depend on its final density and grain size. An annealing treatment provides the energy to reduce its excess surface and/or interfacial energy, a phenomenon termed as sintering. This reduction in energy is achieved by diffusional transport of material from regions of high chemical potential to regions of low chemical potential. For polycrystalline materials,

diffusion can occur over multiple paths (sintering mechanisms). While certain sintering mechanisms reduce the excess energy via shrinkage (or densification), which converts surface area to lower energy interfacial area, others result in grain growth (or coarsening), which reduced the total surface area. Microstructural evolution of a compact of powder and thus its final properties are a result of the competition between the densifying and non-densifiying diffusion mechanisms. Figure 1 schematically demonstrates the effect of these mechanisms on the final microstructure.

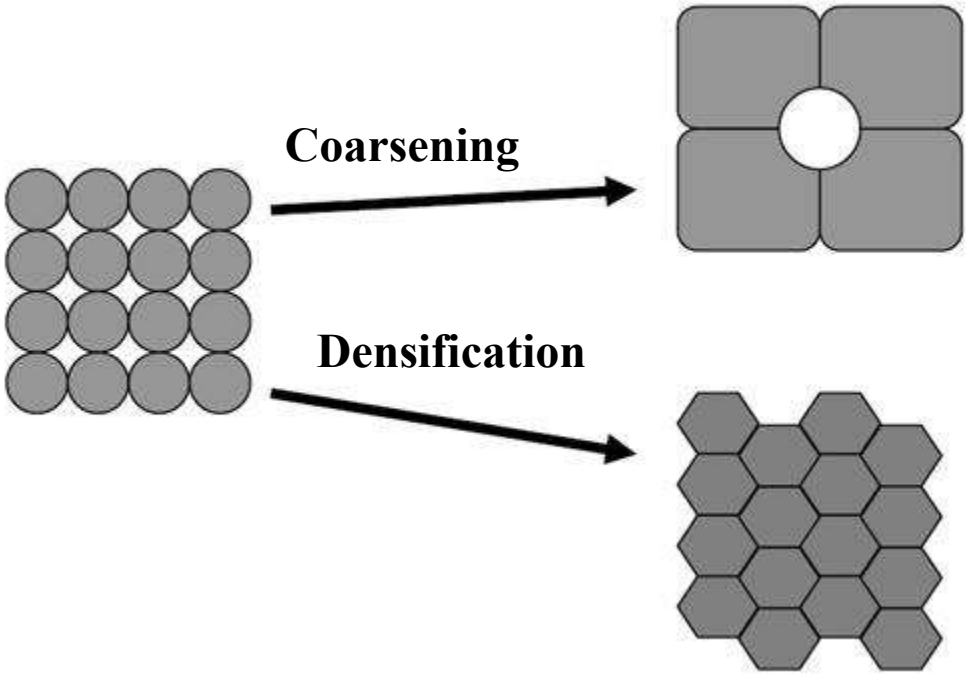

Figure 1: Effects of extreme cases of only coarsening (increase in grain size with no change in density) and only densification (reduction in porosity with no change in grain size) on the final microstructure.

2.3 SINTERING MECHANISMS

Sintering mechanisms are defined by definite paths along which diffusional transport of matter occurs. Since the chemical potential of atoms within the volume, grain boundary, or surface of the particles is higher than that of the atoms at the inter-particle neck (shown in Figure 2), all diffusion paths transport material to the inter-particle neck. Figure 2 schematically illustrates the six known diffusion paths for polycrystalline materials to the neck region between the powder particles. Note that the transport of material from the surface to the interparticle neck does not result in any approach of the center of mass of particles and would result in only coarsening and no densification. Conversely the transport of atoms along grain boundaries or within the volume of the particles results in an approach of the center of mass of particles, resulting in densification.

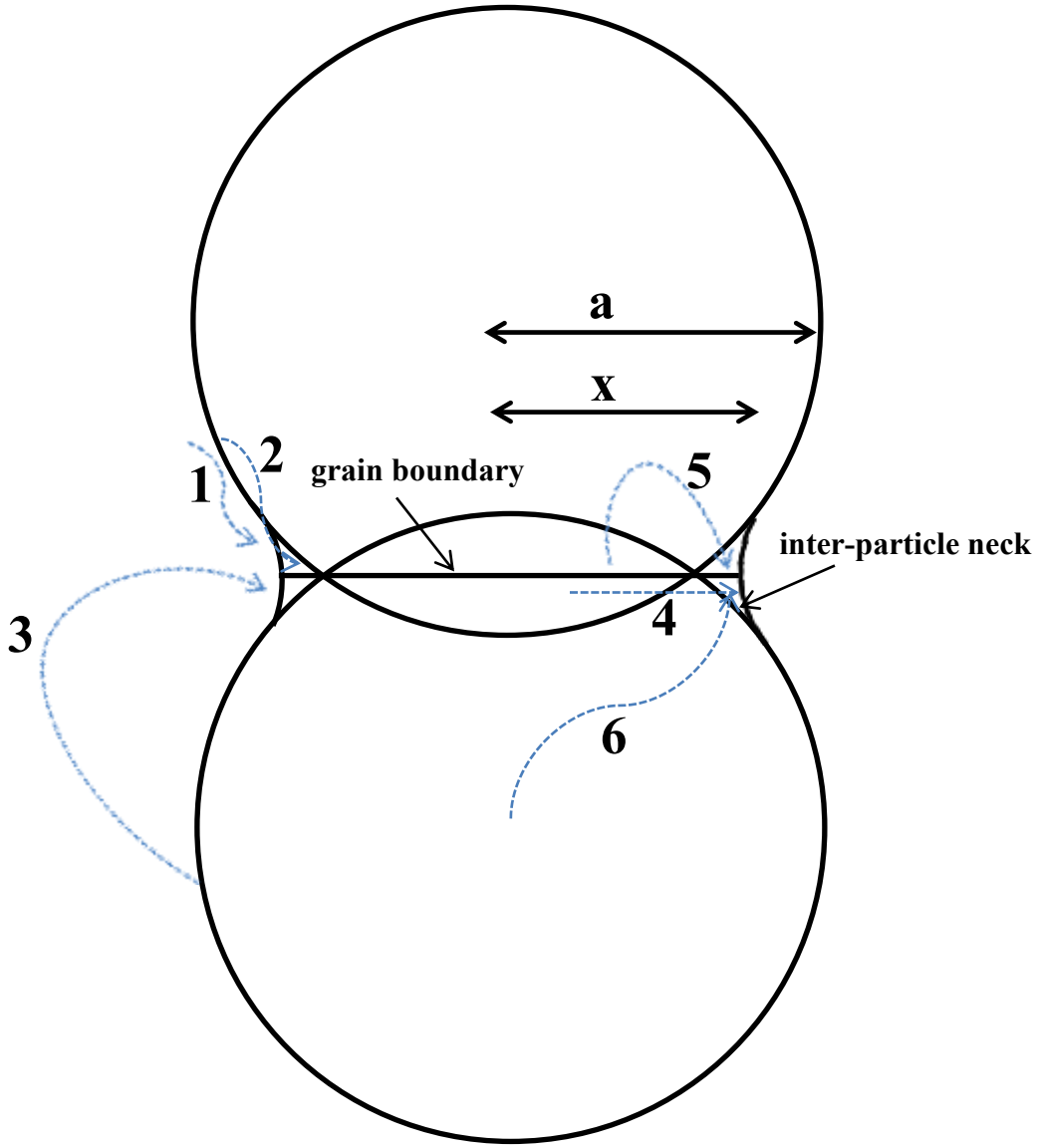

Figure 2: Schematic representation of six distinct diffusion mechanisms that can contribute to the sintering of crystalline particles. Redrawn from Ref. 32.

Consideration of the all of the possible mass transfer path shows that the non-densifying (coarsening) sintering mechanisms are:

1. Surface diffusion
2. Volume diffusion (from the surface)
3. Evaporation condensation

The densifying sintering mechanisms are:

4. Grain boundary diffusion
5. Volume diffusion (from the boundary)
6. Plastic flow

2.4 DIFFUSIVITY

Diffusivity is the fundamental parameter that characterizes any sintering diffusional mechanism. Diffusivity measurements for silver at different temperatures have been conducted previously. Traditionally, these studies involved measuring the silver self-diffusion constant using a radioactive tracer[33]. A traditional plot of diffusivity for Ag is shown in Figure 3.[33] . It is apparent from the figure that at low temperatures surface diffusion and grain boundary diffusion are the dominant operative sintering mechanisms and that other diffusion mechanisms do not contribute significantly to the total mass transport.

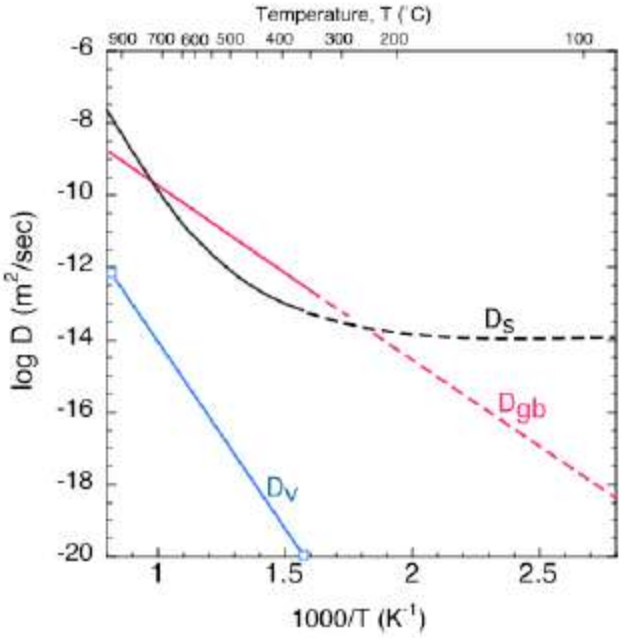

Figure 3: Published values on diffusivity of silver. Reprinted from Ref. 33.

While diffusivity data for temperatures above ~ 300 °C exist and are shown by the solid lines in Fig. 3, low temperature data on bulk Ag does not exist. The dashed lines show the extrapolations to low temperatures, and while the reliability of the extrapolations to make quantitative predictions is questionable, the trends in the values of diffusivity provide useful qualitative insights in the sintering behavior of silver at low temperatures. The trends in diffusivity indicate that at low temperatures only grain boundary diffusion and surface diffusion are the dominant sintering mechanisms. It should also be pointed out that the scatter in diffusion data can be significant. This is particularly true of the surface diffusivity which has reported values[34,35,36,37,33] that vary by 5 orders of magnitude at a given temperature. Thus the data for surface diffusivity

should be more correctly presented as a band with a width of about one order of magnitude.

2.5 Surface Diffusion and Grain Boundary Diffusion

At low temperatures, diffusion via evaporation and condensation is not possible since the vapor pressure of silver is not low enough to allow was evaporation of silver atoms at low temperatures[38]; similarly plastic flow does not contribute to diffusion due to the absence of mobile dislocations at low temperatures[39]. The known data for volume diffusion for the surface and boundary also suggests that these two mechanism are dormant at low temperatures[33]. Since at temperatures of interest for this work (temperatures lower than 250 ^{o}C), surface diffusion and grain boundary diffusion are expected to be the only dominant mechanisms[33], it is worthwhile to explore the theoretical concepts that explain the geometric and structural changes induced in particles by these mechanisms.

Surface diffusion, as shown in Figure 2, occurs by diffusion of atoms from near the particle surface where there is a positive radius of curvature (convex surface) to the neck surface where there is a negative radius of curvature (concave surface). This does not produce a change in the distance between the centers of the particles and hence would not lead to any change in the total volume of the system and would only lead to an increase in the neck radius between the particles. Surface diffusion is thus a coarsening or

non-densifying mechanism. An idealized two particle model describing surface diffusion gives the following dependence of the neck radius to particle radius[40]:

$$\left[\frac{x}{a}\right]^7 = \frac{56 D_S \delta_S \gamma_S \Omega}{kT a^4} . t \qquad \text{Equation 4}$$

where,

x is the neck radius,

a is the particle radius,

D_s is the surface diffusivity,

δ_S is the thickness for surface diffusion,

γ_S is the specific surface energy,

Ω is the atomic volume,

kT has its usual meaning,

t is time.

Grain boundary diffusion, as shown in Figure 2, is the diffusion of atoms from the grain boundary to the neck surface. Grain boundaries are composed of vacancies, interstitials and point defects and are a perfect source and sink of atoms. It is for this reason that grain boundaries act as high diffusivity paths[41]. The transport of atoms from grain boundaries can be accommodated only by the approach of particle centers. Grain boundary diffusion is thus a densifying mechanism. An idealized two particle model describing grain boundary diffusion gives the following dependence of the neck radius to particle radius, and shrinkage with time[42]:

$$\left[\frac{x}{a}\right]^6 = \frac{96 D_{gb}\delta_{gb}\gamma_{gb}\Omega}{kTa^4} \cdot t \qquad \text{Equation 5}$$

$$\left[\frac{\delta L}{L_0}\right]^3 = -\frac{96 D_{gb}\delta_{gb}\gamma_{gb}\Omega}{2^4 kTa^4} \cdot t \qquad \text{Equation 6}$$

where,

x is the neck radius,

a is the particle radius,

D_{gb} is the grain boundary diffusivity,

δ_{gb} is the thickness for grain boundary diffusion

γ_{gb} is the specific grain boundary energy,

Ω is the atomic volume,

kT has its usual meaning,

t is time,

$\frac{\delta L}{L_0}$ is the linear shrinkage.

There is no doubt that the development of two particle models opened the way for a qualitative description of sintering behavior and have led to insights into the effects of various parameters (eg. particle size, temperature, time). However, the equations derived from the highly idealized models[43] often cannot be used to predict experimental behavior for actual powder compacts that contain many particles[44,45].

2.6 STAGES OF SINTERING

Solid state sintering is usually divided into three overlapping stages – initial, intermediate and final. Figure 4 schematically depicts the densification curve expected for conventional powders through these stages over sintering time.

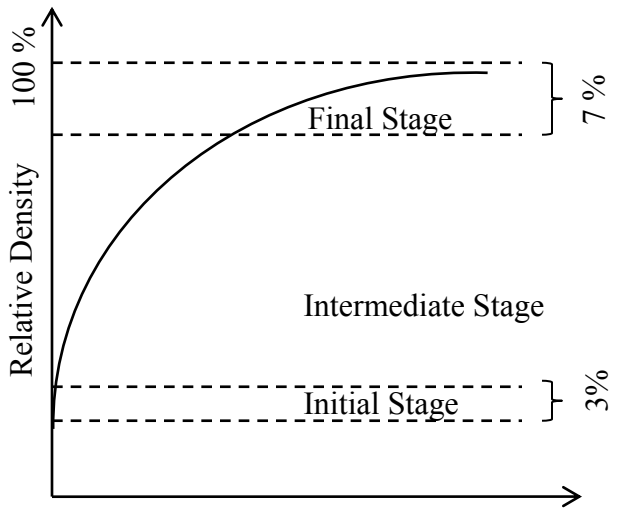

Figure 4: Schematic showing the conventional densification curve of a powder compact and three stages of sintering. Redrawn from Ref. 46.

Initial stage sintering is characterized by the formation of necks between particles. The large differences in surface curvature at the particle surface and neck results in densification and neck growth in the initial stage. Since, the initial stage considers only the neck growth between particles, simplified two-particle models such as those used to derive Equation 4 and 5, may adequately describe the process.

Intermediate stage sintering is assumed to begin when pores have reached their equilibrium shapes as dictated by surface and interfacial tension. The pore structure is still continuous and the densification proceeds simply by pores shrinking and pinching off from each other leaving isolated pores. Coble proposed a geometrical model[47] for intermediate stage sintering of poly-crystalline materials assuming a uniform pore geometry and evaluated the effect of densifying mechanisms. Since the model assumes a uniform pore geometry i.e. same chemical potential everywhere, the non-densifying mechanisms are considered inoperative in this model.

Final stage sintering begins when the pores pinch off and become isolated at the grain corners. The pores then shrink continuously and may disappear completely. Grain growth is likely to happen in the final stage of sintering and models including simultaneous grain growth and densification have been proposed[48].

Since diffusion distances in NPs are very short, the kinetics of sintering are much faster than in conventional micron-sized powders and the stages of sintering may not be individually distinguishable in these systems.

2.7 GRAIN GROWTH

Grain growth is an important aspect of sintering and has a significant influence on the final conductivity of the sintered product. The global driving force for grain growth is the reduction in the total area of the grain boundaries as grains grow. Greskovich and

Lay[49] proposed a simple explanation for the local driving force for grain growth. They considered two randomly oriented, spherical, single crystal grains of radius *R1* and *R2*, as shown in Figure 5. During initial stage sintering, material is transported from the surface and grain boundary to the neck region by diffusion. As the neck radius grows, the grain boundary area also grows. Atoms in the grain boundaries have a higher energy than those in bulk of crystalline grain, so the grain boundary is characterized by a specific energy, γ_{gb}. If this excess free energy per unit area of the grain boundary is *df*, the excess free energy of the grain boundary at an instant can be given as *A df*. Given a constant *df,* the condition for the center of grain boundary being pinned to the center of intersection of the two grains, as shown in Figure 5, can be simply expressed as $dA/dz = 0$ and $d^2A/dz^2 > 0$. The diffusion of matter due to differences in surface curvature can proceed as long as *A df* remains less than the reduction of free energy due to the decrease in surface area because of curvature differences. However, as the neck grows and approaches the diameter of the smaller sphere (this is approximately the end of initial stage sintering), the minimum in grain boundary area shifts towards the smaller particle on the *z* axis. The grain boundary is thus free to move towards the smaller particle at this point. When the density is relatively low that porosity is open, this model provides an adequate description of grain growth.

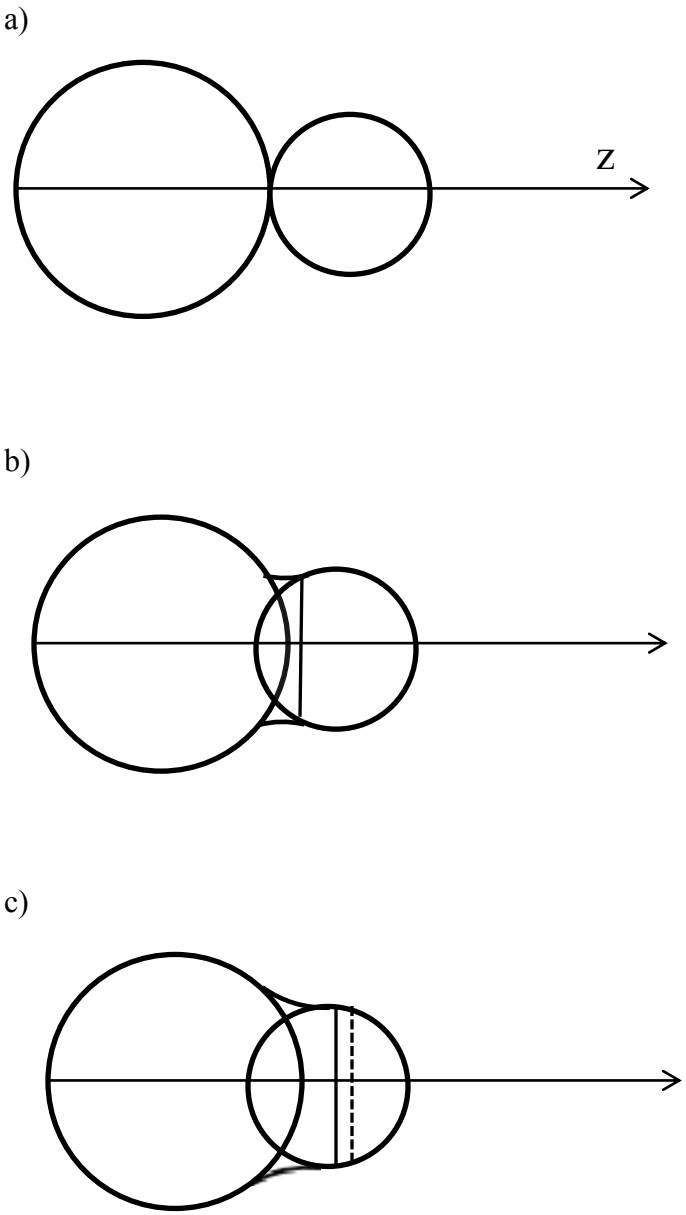

Figure 5: Schematic of grain growth in less dense solids (a) Initial stage, (b) The two sphere system has shrunk and the neck region is pinned, the point of minimum cross section area of the neck, (c) Unpinning stage. Redrawn from Ref. 49.

When the density is increased so that porosity is closed, isolated pores can exert a drag on boundary motion that influence grain growth. The pores can be either completely

immobile, or can be mobile and exert a drag on the grain boundary as it moves. Both mobile and immobile pores can either pin the grain boundary, limiting grain growth; or if the driving force for grain growth is very high, the boundary can break away leaving an isolated pore, which can limit densification. Considering the kinetics of grain boundary interactions, a grain growth equation in its general form can be expressed as[50]:

$$G^m + G_o^m = K \cdot t \qquad \text{Equation 7}$$

where,

G is the grain size,

G_o is the initial grain size,

K is a constant,

t is time,

The value of exponent m varies depending on the mechanism and is tabulated for relevant case in Table 1.

Table 1: Grain growth exponent m for different diffusion mechanisms[50]

Mechanism	Exponent *m*
Pore control	
Surface diffusion	4
Grain Boundary Control	
Pure system	2

2.8 SIMULTANEOUS DENSIFICATION AND GRAIN GROWTH

Microstructure evolution during low temperature sintering involves a competition between grain boundary diffusion and surface diffusion. While grain boundary diffusion reduces the excess surface area via shrinkage (or densification), surface diffusion results in grain growth (or coarsening) and results in reduction of both the surface area and grain boundary area. Particle coarsening caused by surface diffusion can adversely affect the densification rate by lowering the driving force for densification and by increasing the diffusion distances. The inability for many materials to densify completely can be understood in terms of these competing mechanisms.

Since, the extent of both densification and grain growth influence the rate at which the other proceeds, it is important to address the simultaneous occurrence of these phenomenon to make any useful prediction of the final microstructure. Such a theory of simultaneous grain growth and densification was proposed by Yan, Cannon and Chowdhry[48] for final stage sintering. In this theory it is assumed that densification results from the material transport between pores and grain boundaries by grain boundary diffusion, and grain growth is controlled by pore mobility which is limited by surface diffusion. The overall behavior of this system is controlled by the parameter Γ, which is given by

$$\Gamma = \frac{3}{176}\frac{D_s \delta_s \gamma_{gb}}{D_{gb}\delta_{gb}\gamma_s} \qquad \text{Equation 8}$$

where, D_s is surface diffusivity, D_{gb} is grain boundary diffusivity, δ_s is the effective surface depth, δ_{gb} is the effective grain boundary depth, and γ_s and γ_{gb} are the surface and grain boundary energies, respectively. When $\Gamma > 1$, coarsening is expected to dominate, whereas densification is expected to dominate the initial stages of sintering when $\Gamma < 1$.

This theory can be used to predict that the extent of grain coarsening and the achievable final density from the controlling mechanisms. From Yan *et al.'s* analysis it is apparent that, at a given temperature, the dominance of densification or coarsening are determined by ratio of diffusivities (D_s/D_g), since the other factors that influence the parameter Γ are not strongly dependent on temperature. As shown in Figure 6 there exists a low temperature regime below temperature T_c where coarsening (surface diffusion-dominated) is dominant and a temperature T_d above which densification (grain boundary diffusion dominated) is dominant. In the temperature regime between T_c and T_d, there is a significant influence from both surface diffusion and grain boundary diffusion. The physical significance of T_d is that it is the minimum temperature at which a powder compact can be processed to achieve near theoretical densities at low temperatures in reasonable processing times; the regime T_c-T_d yields densities less than the theoretically achievable densities; below T_c there is no densification observed but significant grain growth occurs. Thus the values of T_c and T_d can be used to design the appropriate processing treatment to achieve the desired final density and microstructure in the sintered body.

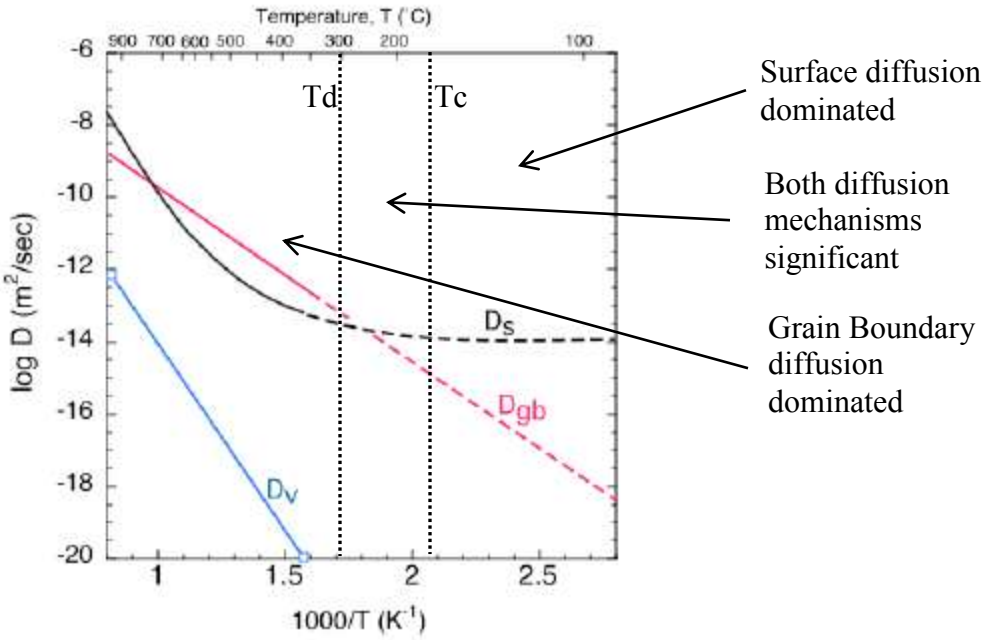

Figure 6: Temperature regimes with different dominant diffusion mechanisms

The above discussion shows that, by knowing the temperatures T_c and T_d, it is possible to control the final sintered density and microstructure and hence the final property of the sintered compact.

2.9 ANNEALING TREATMENT

The annealing treatment given to a powder compact depends on the processing temperature and time, and the heating rate and can be used to control the final microstructure and density of the powder compact. Conventionally, annealing treatments are performed in furnaces with a slow heating rate (~ 5 K/min[51]). Although the heating

rate is not typically varied significantly during sintering studies, it has been shown to have an effect on the final sintered product in previous studies[51,52,53] .

The expected effect of heating rate can be seen in any diffusional process since the flux of material transported is directly proportional to time. With respect to low temperature sintering of metals, a slow heating rate implies more time spent in the surface diffusion dominant regime (where $\Gamma > 1$). Thus, when the temperature eventually reaches the stage where grain boundary diffusion is dominant (where $\Gamma < 1$) at higher temperatures, the driving force for densification is reduced relative to the starting microstructure. If densification is the primary objective of the sintering treatment, as is in our case, a rational annealing treatment would bypass the low temperature surface diffusion stage completely by heating rapidly to a temperature where grain boundary diffusion is dominant. Rapid thermal annealing also offers the ability to do a two-step annealing treatment such that the first annealing treatment is done below T_c for a certain time such that driving force for densification is reduced for the second annealing treatment above T_d, where the grains grow with no or little densification. Such a two-step annealing treatment offers more control than a slow heating rate annealing treatment and also reduces the time for processing. It should be noted that a design of annealing treatment requires knowledge of the values of diffusivities.

2.10 FACTORS THAT INFLUENCE SINTERING

Particle size: Particle size has a strong influence on the kinetics of sintering which can be well explained by Herring's scaling laws[54]. When powders with similar shapes and different sizes are sintered under the same experimental conditions, Herring's scaling law predicts

$$\frac{R_2}{R_1} = \lambda^{-m} \qquad \text{Equation 9}$$

where λ is the ratio of the particle radii for two powders with different mean radii, R_1 and R_2 are the rates of sintering of these two powders, and m is the exponent corresponding to a particular diffusion mechanism. The exponent m=4 for both of the diffusion mechanisms of interest, surface diffusion and grain boundary diffusion[54]. Had the exponents been different, a transition from one dominant diffusion mechanism to another would be predicted as the particle size is increased. However, because the exponents are equal for both diffusion mechanisms, Herring's scaling law predicts that one of the diffusion mechanisms will be dominant, independent of the size of the particle.

Particle size distribution: There has been considerable experimental evidence that a non-uniform particle size distribution is detrimental to achieving high densification. Yan *et al.*[48] analytically examined this phenomena based on a force balance between driving force for grain growth and the drag force due to pores which leads to pore separation from grain boundaries. They argued that since the intergranular pores become entrapped

(assuming that the diffusion of the gas species entrapped within the pores is negligible through the solid), the density at which pores and grain boundaries become separated can be considered as the final density. They showed that pore separation will occur if the driving force for grain growth is larger than the drag force exerted by the pores. The driving force for grain growth increases with a broader grain size distribution since there is a greater fraction of very small, energetically unfavorable grains, and thus the final achievable density is lower for a large grain size distribution. It is logical to assume that a uniform particle size distribution would lead to a more uniform grain size distribution and thus greater densification.

State of agglomeration: The presence of agglomerates in powders reduces the packing efficiency and suppresses the sinterability. The presence of agglomerates also leads to heterogeneous packing in the green body. This heterogeneous packing can result in differential sintering, where different regions of the body shrink at different rates[55] leading to the development of large pores and poor final densities. The deleterious effect of agglomeration on sintering has been investigated qualitatively by several researchers and has shown to decrease densification rates by as much as a factor of 10[56].

Green density: The final density of a sintered powder depends on the number of sinterable pores which can be removed via grain boundary diffusion. A sinterable pore is one that has a low coordination number, and the population of the sinterable pores thus decreases with green density. For micron sized ceramic powders, a green density of about

58% is reported to be the minimum required to achieve complete densification[57]. The effect of green density on final densification is influenced by both time and temperature: The temperature and the time required to reach complete densification decrease when the green density is increased.

Dominant sintering mechanism: Sintering kinetics, final achievable density and microstructural evolution are all dependent on the dominant sintering mechanism. The effect of a single dominant sintering mechanism was shown in Figure 1. However, in reality more than one sintering mechanism can be dominant over a range of temperatures. Since sintering is a diffusional process the dominant sintering mechanisms are a function of temperature and their effects can to some extent be controlled by the controlling the heating rate[58].

Influence of organic capping: The presence of organics is known to inhibit low temperature sintering, especially in NPs[59], because the pyrolysis temperature of the organic capping is generally higher than the temperature at which sintering begins. It is for this reason that ink and paste based methods fail to achieve high relative densities in the sintered product at low temperatures.

The above discussion points out the major factors that inhibit NP sintering are:

1) The presence of organic molecules on the NP surfaces,

2) The dominance of non-densifying surface diffusion over grain boundary or lattice diffusion

3) Agglomeration of NPs, and

4) Low initial density of the NP compacts.

To observe the maximum beneficial effects of low temperature sintering it is important that these deleterious factors to sintering be minimized. It is for this reason that this work focuses a great deal on developing a process to produce near ideal powder compacts. Moreover, the effects of low temperature sintering are more likely to be observed for nanoparticulate powder, since the sintering kinetics would allow the observation of these effects in reasonable times.

Chapter 3: Experimental Procedures

This chapter describes the details of the experimental setup and procedures used for this research. Section 3.1 introduces the direct write setup and the control of process parameters. Section 3.2 describes the setup for the annealing treatment of the prepared samples. Section 3.3 -3.6 gives details of the procedures for the measurement of cross-sectional area, conductivity and density. Finally, Sections 3.7-3.8 describe the tools used for microscopy and grain size measurements.

3.1 Deposition Procedure

The use of the laser ablation of microparticle aerosol (LAMA) process to direct write nanostructured, patterned films of silver has been reported previously[60,61]. For this study we have used the same basic setup, with some modifications. The schematic of the setup used for this work is shown in Figure 7.

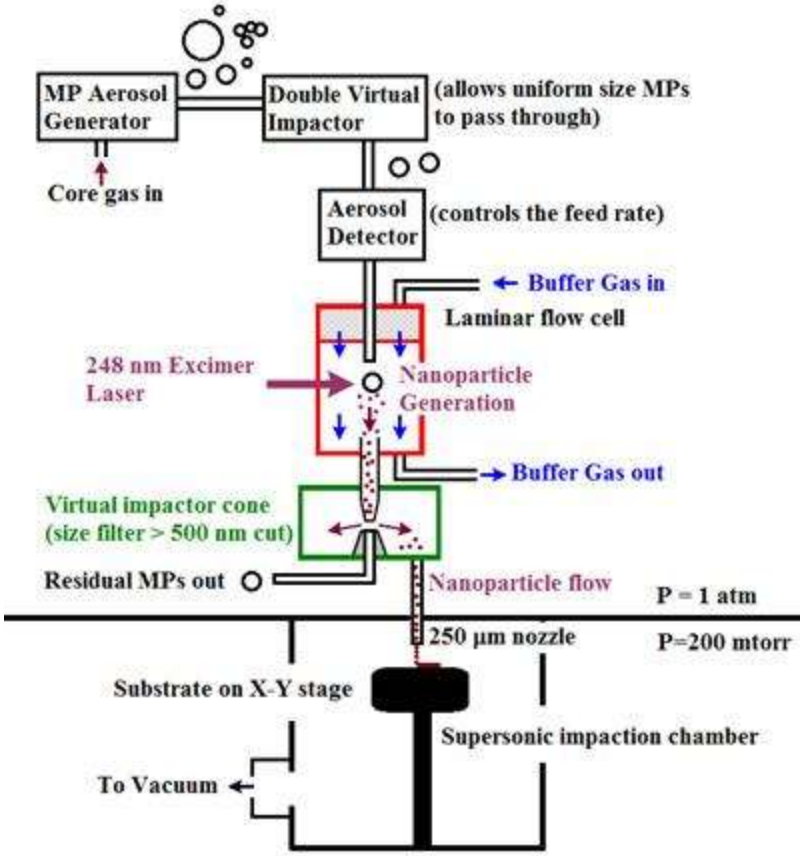

Figure 7: Schematic of the direct write setup

The following sections discuss the individual parts of the direct write setup and outline the details of the deposition process.

3.1.1 Aerosol Feeding and Detection Setup

Most of the previous work where Ag was directly written using the LAMA process utilized a fluidized bed with an integrated settling chamber to create the aerosol of

microparticles that is necessary to perform LAMA[24,25,62,63]. A schematic of this feeder is shown in Figure 8.

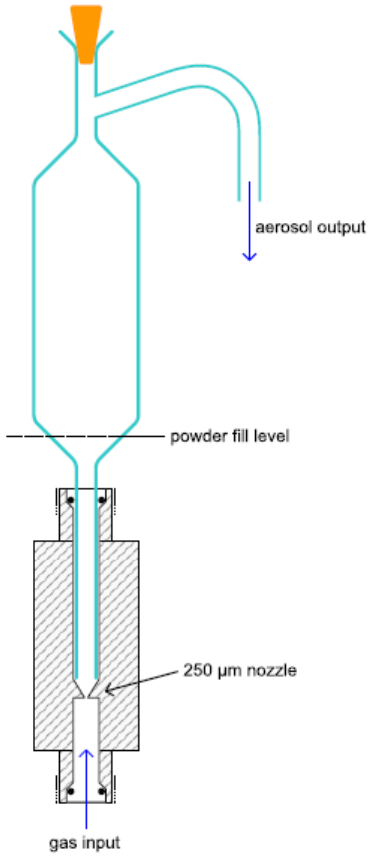

Figure 8: Fluidized bed aerosol feeder to aerosolize the MPs. Reprinted from Ref. 26.

While the fluidized bed aerosol feeder has been shown to be an effective means for producing a MP aerosol, Gleason[26] showed that it is not an ideal feeder for the LAMA process. In particular, he showed that fed a non-uniform size distribution of MPs and if the MPs were agglomerated, these agglomerates were also passed through the feeder[26]. Since agglomerated MPs have a tendency to produce agglomerated NPs in the LAMA

process[26], it was desirable to remove MP agglomerates prior to ablation. A double virtual impactor design proposed by Chen *et al.*[64] and subsequently used by Gleason *et al.*[26] has been shown to be capable of removing agglomerates, large particles, and small particles so that a uniform size distribution of individual MPs can be fed into the LAMA apparatus. In the present study we used this fluidized bed aerosol equipped with a double virrual impactor, which is shown in Figure 9.

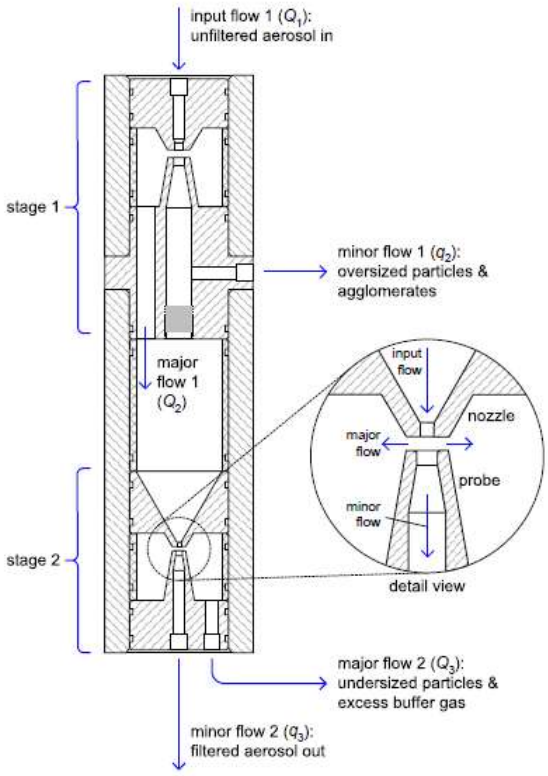

Figure 9: Design of the double virtual impactor. Reprinted from Ref. 26.

The double virtual impactor works in two stages, the first stage removes the larger sized MPs (> 1.8 μm) and agglomerates and the second stage removes the undersized MPs (<

0.8 μm). Thus, the double virtual impactor allows only feedstock that is between 0.8 μm and 1.8 μm to pass through. SEM images of the feedstock MPs shown with and without the double virtual impactor in place are shown in Figure 10. From these micrographs, it is clear that the double virtual impactor is very effective at removing agglomerates, large MPs and small MPs, but at the cost of eliminating a large fraction of the feedstock particles.

a)

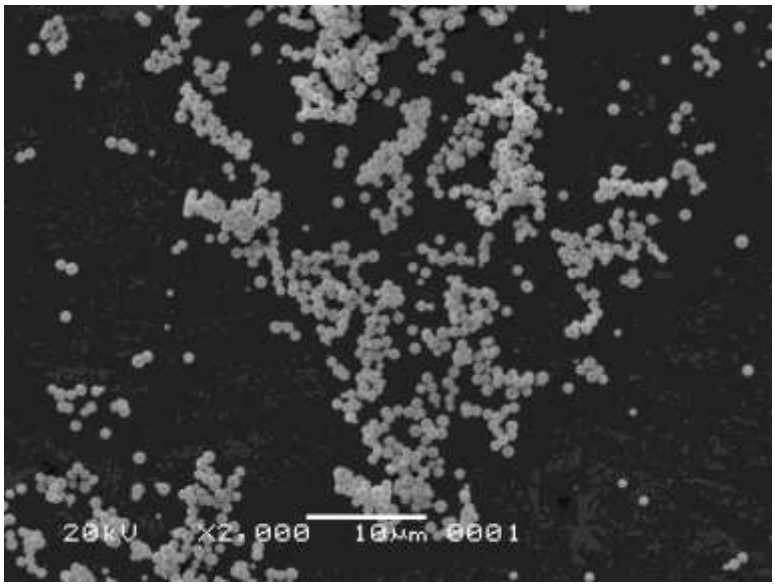

b)

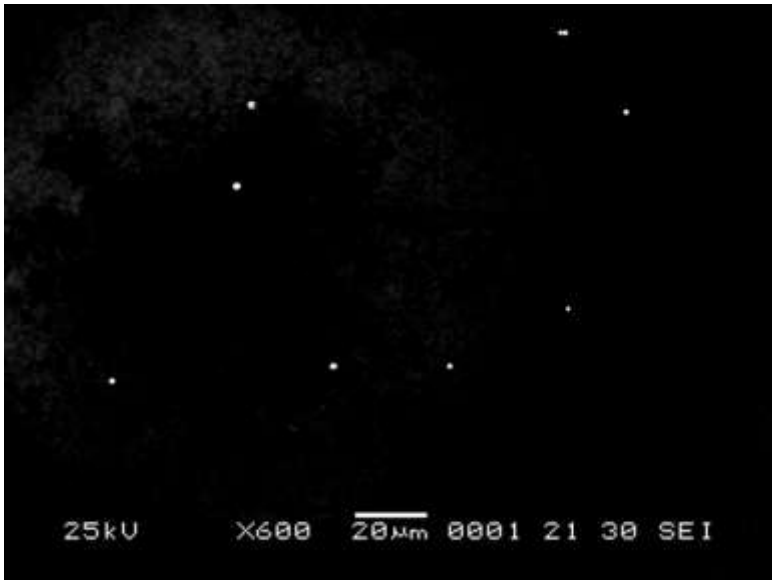

Figure 10 SEM micrograph of feedstock MPs a) before, and b) after the double virtual impactor. The MPs were collected for the same amount of time in both cases.

Gleason's *et al*[26]. showed that the final state of agglomeration of NPs produced by the LAMA process is directly related to the feed density of the MP aerosol. As the feed density is increased, a transition is observed from the production of mostly individual NPs to the production of small agglomerates. As the feed density is increased further, the size and fraction of agglomerates is increased. Thus, the feed density must be carefully controlled to produce a uniform distribution of individual NPs[26]. To accomplish this, Gleason designed and built an aerosol detector, shown in Figure 11, to measure the scattering of a He-Ne laser by the MP aerosol and from this, measure the MP feed density. The feeder parameters are then adjusted to control the MP feed rate. Gleason *et al.'s* MP feeder, double virtual impactor, and aerosol detector were used in the present work to control the MP feed density.

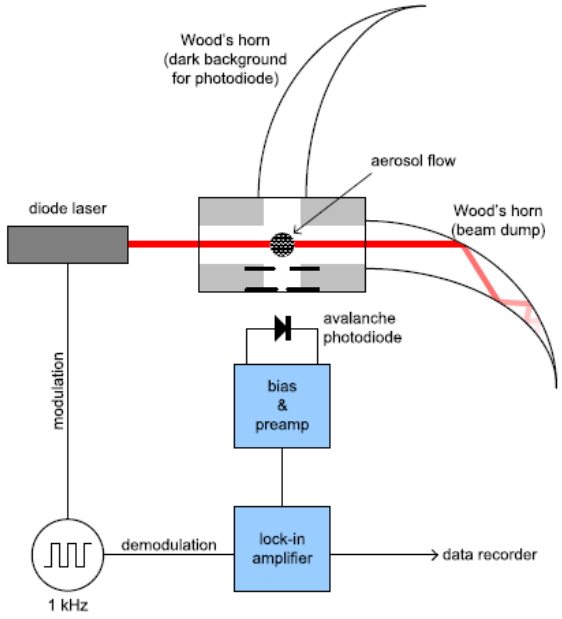

Figure 11: Aerosol Detector. Reprinted from Ref. 26.

3.1.1.1 CONTROL OF MICROPARTICLE FEED RATE

Three different MP feed rates of 10 mg/hr, 20 mg/hr and 50 mg/hr corresponding to a MP feed density of 0.85, 1.7 and 4.25 mg/cm^3, were utilized for this study. A MP feed rate of 10 mg/hr has been shown to produce a majority of single NPs and some dimers[26]. As the feed rate is increased to 20 and then 50 mg/hr, the number and size of the agglomerates has been shown to increase. The as deposited film density is expected to decrease with increasing fraction and size of agglomerates because agglomerates have a relatively low packing density. Figure 12 shows the feed rate with time for different feed rates attainable in the present setup. It is apparent from Figure 12 that the variation in feed rate scales with the feed rate so that as the mean feed rate in increased, the variation in the absolute value of the feed rate increases proportionally. However, note that the relative variation in feed rate as measured by the ratio of variation in feed rate to the mean feed rate remains constant at about 50%.

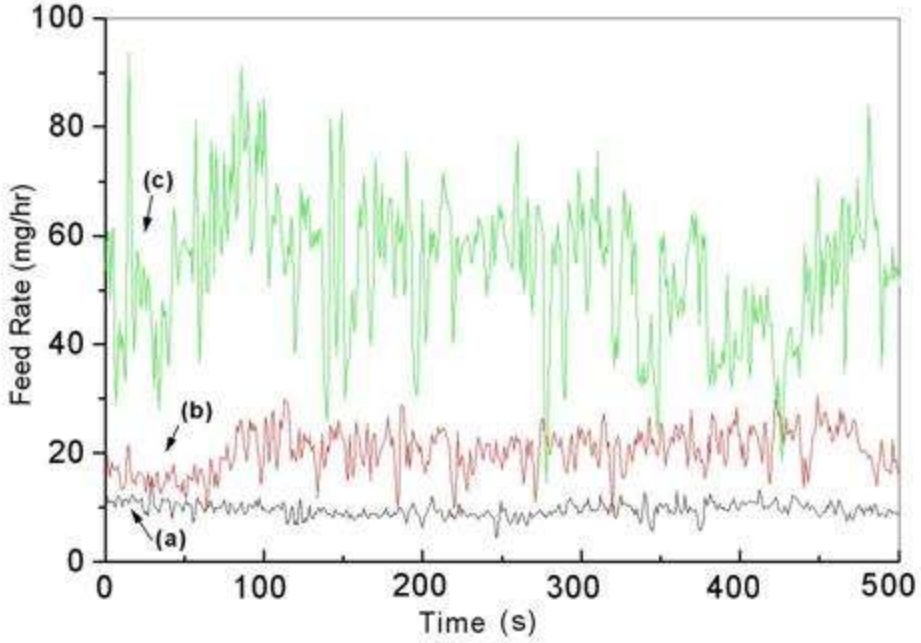

Figure 12: MP feed rate data vs time at feed rates of a) 10 mg/hr, b) 20 mg/hr, c) 50 mg/hr

3.1.2 Laser ablation cell and the optical setup

A KrF excimer laser (PM-848, Lumonics, Nepean, Canada) operating at 248 nm and with a maximum 200 Hz repetition rate, a 12 ns pulse width and a maximum specified power output of 80 W is used for the laser ablation. A pair of anti-reflection-coated cylindrical lenses of focal lengths 110 cm and 14 cm are used to independently adjust the horizontal and vertical foci, respectively, and two dual-tilt mirrors are used to align the beam. A laser energy of 300 mJ is used and the focus is adjusted to a 2 mm wide by 4.0 mm tall spot at the ablation zone, corresponding to a laser fluence of 3.75

J/cm^2. This value of fluence significantly exceeds the breakdown threshold for Ag MPs (0.8 J/cm^2)[65].

The ablation zone resides at the center of the laser ablation cell. The MP aerosol is fed into the ablation zone using a He (99.99% purity) or Ar (99.98% purity) carrier gas through a nozzle. Laminar flow of aerosol is maintained by surrounding the flow of aerosol with a buffer gas of the same linear velocity. The gas velocity of the center flow, Q_{center}, which carries the aerosol, is fixed such that MPs are ablated by the laser only once.

$$Q_{center} = A_{center} \cdot f \cdot h \qquad \text{Equation 10}$$

where, A_{center} is the area of the feed nozzle, f is the frequency of the laser and h is the height of the ablation zone. The corresponding velocity of the coaxial flow, $Q_{coaxial}$ to ensure a laminar flow in the horn cell has the same mean velocity as Q_{center} given by:

$$Q_{coaxial} = Q_{center} \cdot (A_{outer}/A_{center} - 1) \qquad \text{Equation 11}$$

where,

A_{outer} is the area of the outer flow.

Figure 13 shows the design of the laser ablation cell.

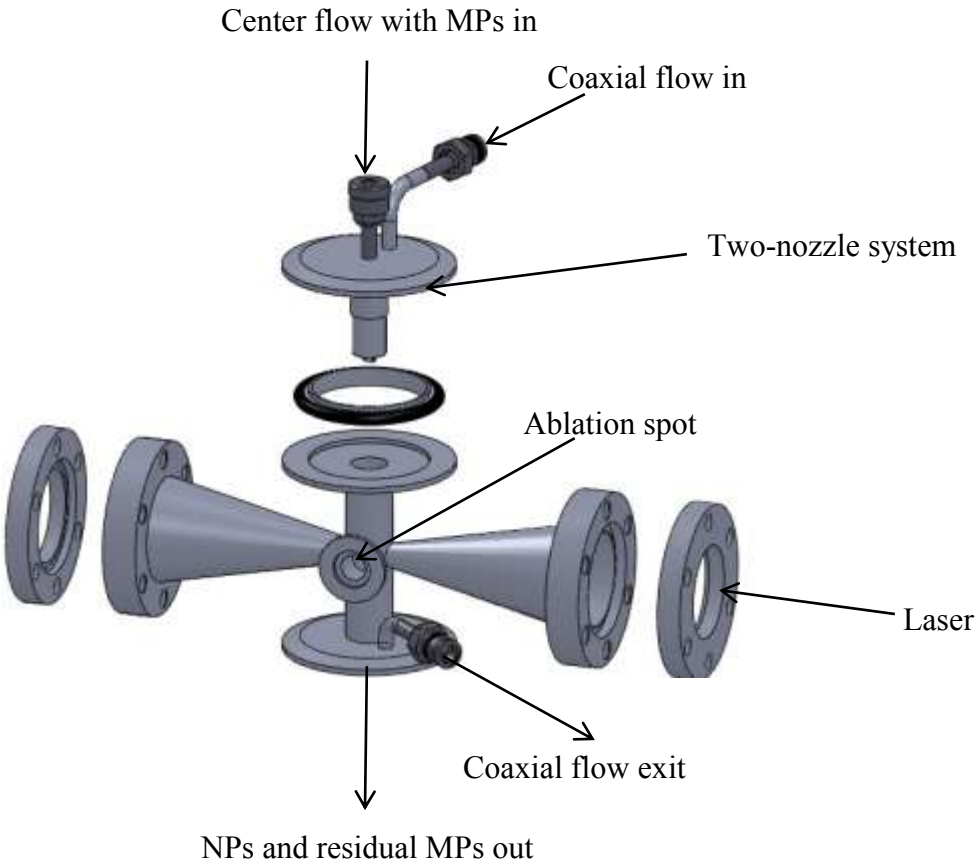

Figure 13: Drawing showing exploded view of the laser ablation cell (nozzle assembly and horn cell). Reprinted from Ref. 66.

3.1.3 Residual MP separation using a virtual impactor

The ablated aerosol containing residual MPs and NPs are fed through a skimmer to a virtual impactor. The virtual impactor is a cone with an orifice in its center. Fine particles in the aerosol travel with the gas and flow around the cone; while larger particles with a higher momentum, originally on the axis of the orifice, enter the orifice. The cut off size for particles to bypass the virtual impactor is set by the height of the cone relative to the jet nozzle. For this work, it has been set at 500 nm so that the virtual impactor successfully removes MPs and large NP agglomerates. A small gas flow of 100 sccm is maintained through the virtual impactor so that particles do not build up inside the virtual impactor. An exploded view of the of the ablation cell and skimmer and virtual impactor assembly is shown in Figure 14.

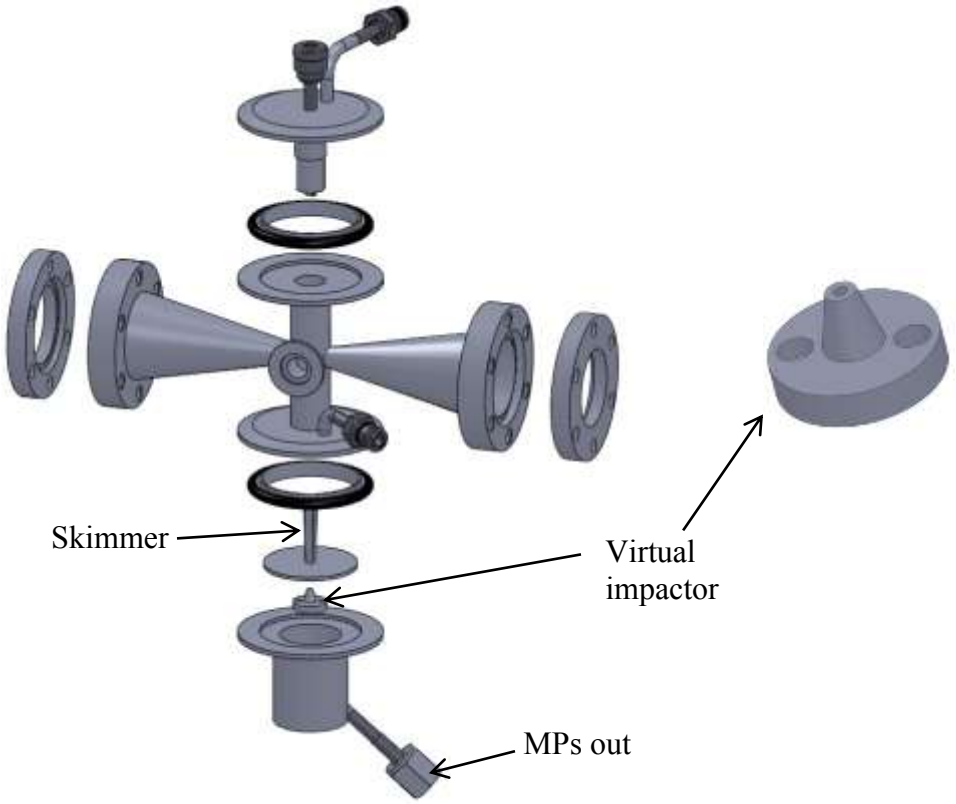

Figure 14: Skimmer and virtual impactor assembly. Reprinted from Ref. 66.

3.1.4 Supersonic impaction chamber

The aerosol that exits the virtual impactor consists of NPs, and at higher feed rates, smaller NP agglomerates. The ablation cell and virtual impactor are held at atmospheric pressure while a mechanical vacuum equipped with a Root's blower (Model 80, Edwards Ltd., Sanborn, NY) are used to maintain a pressure of 250 mTorr in the deposition chamber. The pressure difference between the ablation cell and the deposition chamber serves to accelerate the NP aerosol through the 250 μm orifice nozzle that separates the chambers. The NP deposition velocity has been determined previously[67] for Ag NPs and

ranges from 300 - 1200 m/sec, depending on whether He or Ar gas is used in the aerosol. The nozzle-to-substrate distance can be varied by adjusting the nozzle height. The substrate is fixed to an X-Y stage that moves the substrate position with respect to the deposition nozzle. The X-Y stage is controlled via a graphical programming environment (Labview, National Instruments, Austin, TX) which enables controlled patterning of the film geometry. The thickness of the film is controlled by the writing speed of the stage which can be varied from 7.9 - 635 μm/s, and the aerosol feed density, which is controlled by the aerosol feeder (See section 3.1.1.).

3.2 POST-DEPOSITION ANNEALING

A PID-controlled hot plate was used as a constant temperature source to rapid thermal anneal the samples in this work. A copper plate (diameter = 75 mm) was placed on the hot plate to provide a constant temperature heat source and temperature was monitored at three different positions using a K-Type thermocouple to ensure uniformity of temperature across the plate; measurements showed that the accuracy in temperature was ± 3 ˚C across the surface. The hot plate was allowed to stabilize for 2 hours before each annealing treatment. The samples were rapid thermally annealed by simply dropping them on the copper plate. After the annealing treatment the samples were immediately moved to a large conductive surface to quickly cool them to room temperature.

3.3 AREA CALCULATIONS

An optical profilometer (Model 20, Zeta Instruments, San Jose, California, USA) was used to measure the cross sectional area of the deposited lines before and after annealing. Area was measured at 100 μm intervals along the length of the lines (corresponding to 100 measurements on each line). The areas were averaged to calculate the mean area of each deposited lines.

3.4 DENSITY MEASUREMENTS

The low mass of the deposited lines made it difficult to measure their mass directly. To overcome this challenge, the density of the films was measured indirectly by depositing them onto a substrate, measuring the dimensions of the deposit using the optical profilometer to determine its volume, and then dissolving the deposit into a known volume of nitric acid. The concentration of the solution was determined against a standard using inductively coupled spectroscopy. Three standards of concentration 50.7 μg/L, 150.12 μg/L, and 250 μg/L were prepared and a confidence of 99 % was determined in the concentration of standards. The mass of the deposit was then determined from the known concentration and volume of the solution. Finally, the density was calculated from the ratio of the mass/volume of the deposit.

3.5 CONDUCTIVITY MEASUREMENTS

A four point probe setup was built using a micro-ohmmeter (Model 4338 B, Agilent Technologies, Santa Clara, CA), 4 micro-positioners and an optical microscope attached with a digital camera to capture an image of the probe positions. The outer probes and inner probes were both connected to the micro-ohmmeter and were used to pass a low level AC current (1 μA to 10 mA) and measure the voltage drop. One of the inner probes was kept fixed and the other was positioned at different position and several measurements were taken to measure the conductivity. The values of conductivity from each sample had a repeatability of ~ 99%.

3.6 MICROSCOPY

A high resolution TEM (2010F, JEOL, Tokyo, Japan), operated at 120 KV in brightfield mode was used to characterize the as-produced NPs. The plan view of the as-deposited and annealed lines was characterized using high resolution SEM (Strata™ DB235, FEI, Portland, OR).

3.7 GRAIN SIZE MEASUREMENTS

Grain size distributions were measured by analyzing 100 – 275 grains using image processing software (ImageJ 1.41, NIH, Bethesda, MD).[68] The area of individual grains was measured by tracing the grains using the freehand sketch tool built into Image J 1.41 and the individual grain areas were measured.

Chapter 4: General Characteristics of the Lines

This chapter discusses the influence of the process parameters on NP morphology, film morphology, and the general characteristics of the deposited lines.

4.1 Influence of Carrier Gas

4.1.1 Nanoparticle Morphology

Figure 15 shows the TEM images of NPs produced in He and Ar carrier gas. The mean NP size was found to increase when using a heavier carrier gas; a mean size of ~ 6 nm was measured when using He as the carrier gas and a mean size of ~35 nm was measured when using Ar as the carrier gas. No defects were observed in the majority of the NPs, but some twinning was visible in some of the NPs, as shown in Figure 16. These results are consistent with results from previous work[24,25,2669].

a)

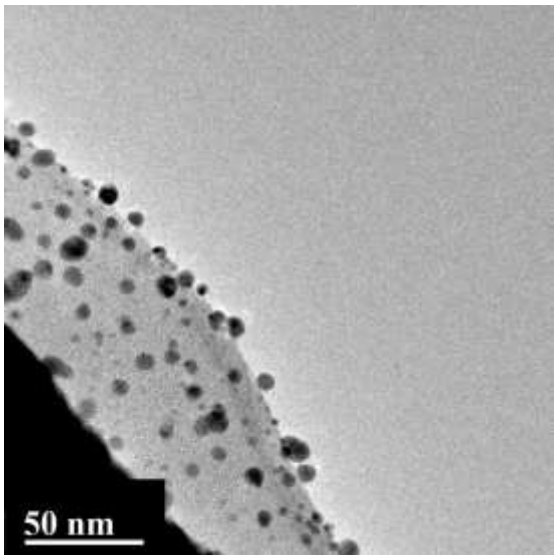

b)

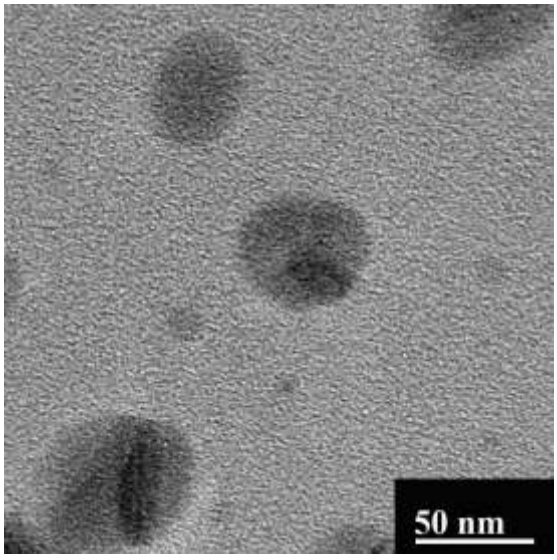

Figure 15: Influence of carrier gas on NP morphology a) He as the carrier gas, b) Ar as the carrier gas.

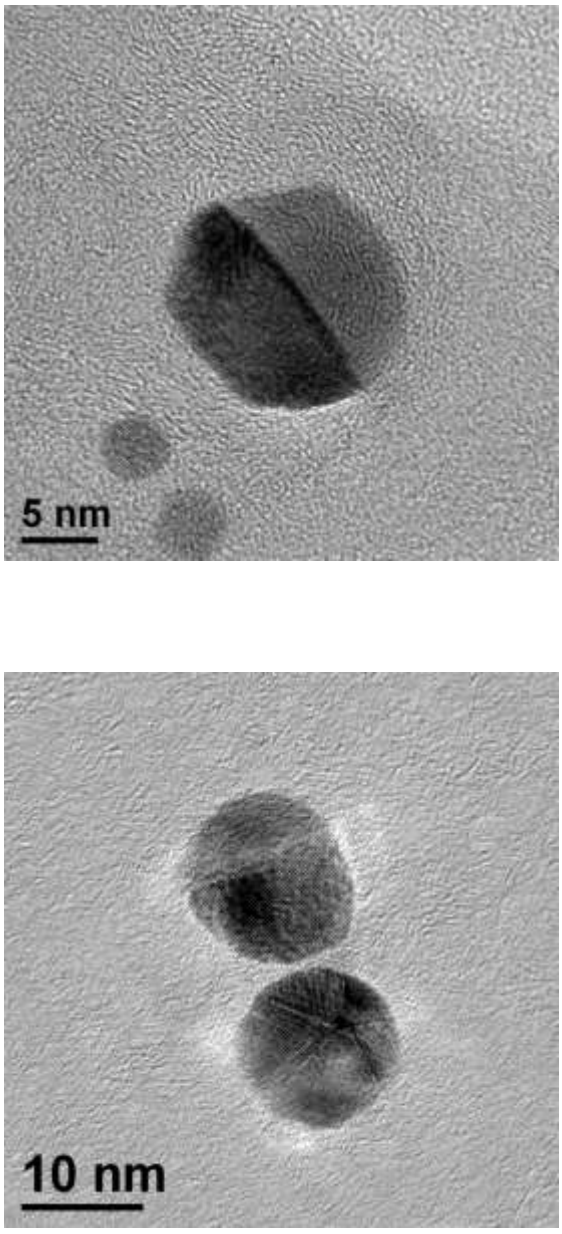

Figure 16: TEM images of NPs that contain twins.

4.1.2 Nanoparticle Morphology in Films

Thin films were deposited on a TEM grid to image the grain morphology of impacted films. To produce films with that were sufficiently thin to remain electron-transparent,, the films were deposited by rastering the substrate once with MP feed rate of 10 mg/hr. This is the same feed rate used to produce thicker films that were produced in multiple passes for conductivity and sintering studies. Figure 17 shows the TEM images of the films deposited in He and Ar. The films deposited in He appear much denser than those deposited in Ar, which is expected because of the higher impaction velocity of smaller NPs in He carrier gas[25,60].

a)

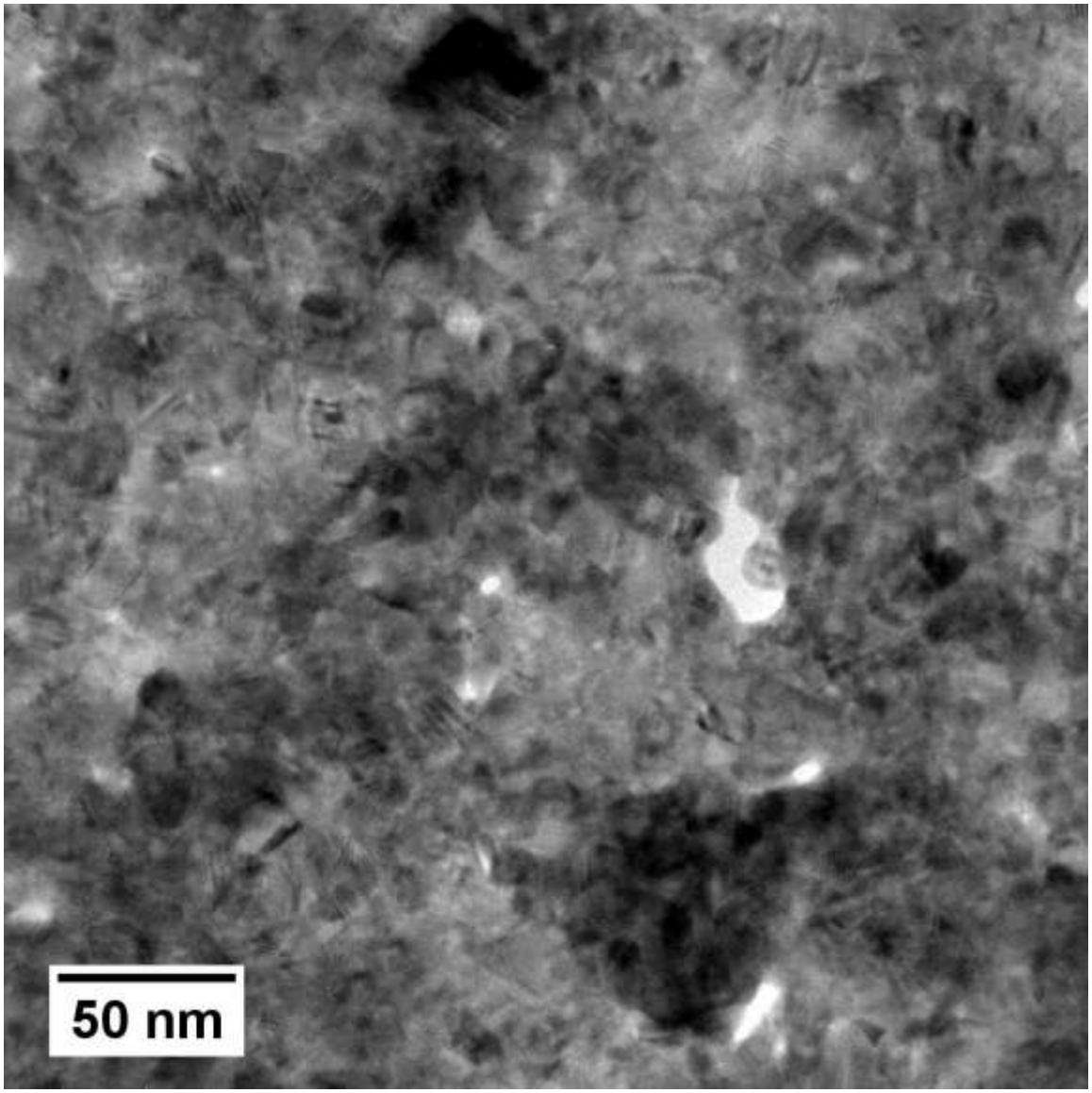

Figure 17: TEM images of films deposited in a) He carrier gas and b) Ar carrier gas

b)

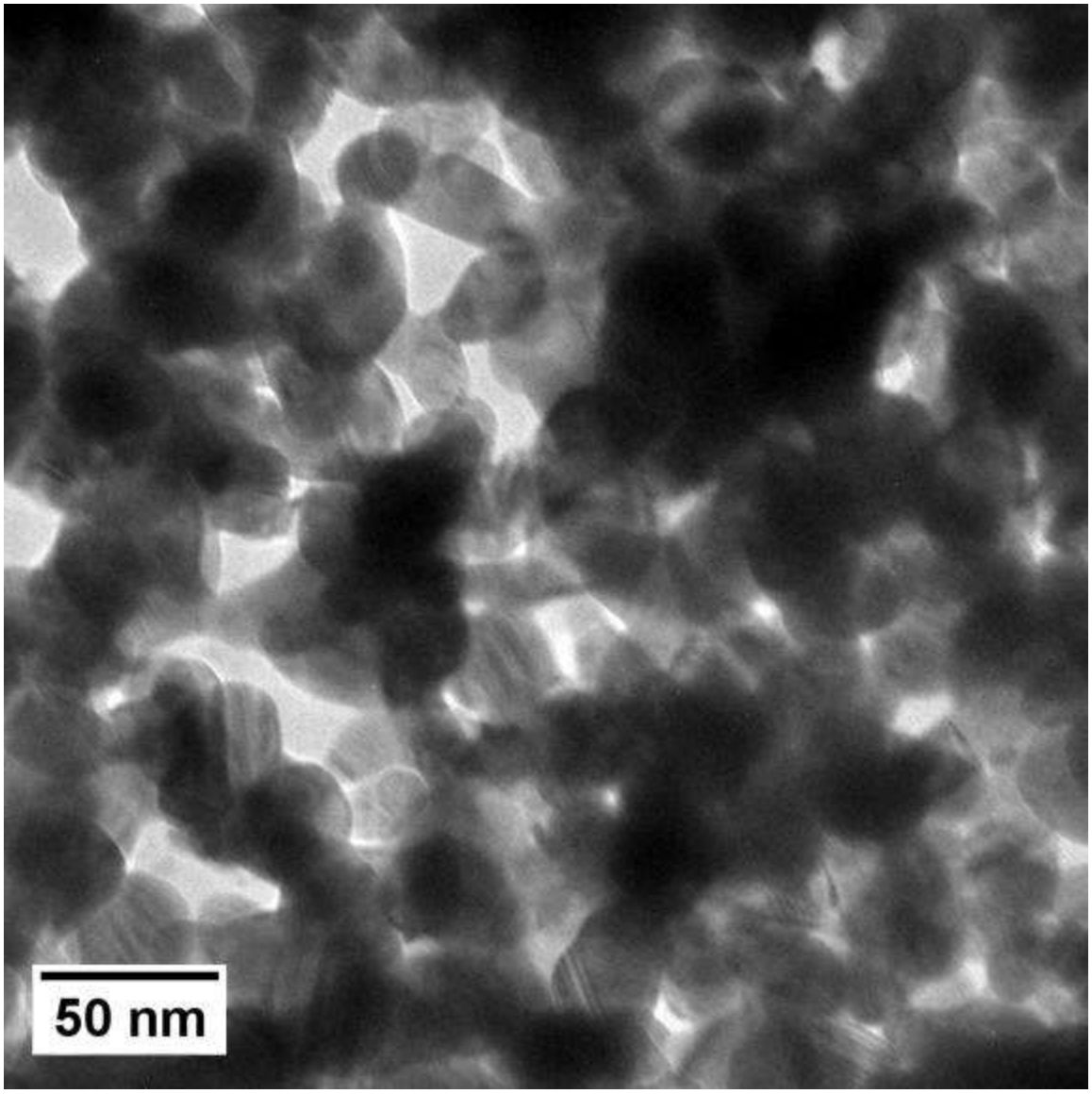

Figure 17: TEM images of films deposited in a) He carrier gas and b) Ar carrier gas

4.1.2 Line Morphology

A plan-view optical micrograph of a line produced in He carrier gas at low feed rates but with 32 passes is shown in Figure 18. Figure 19 shows the profile of lines produced in He and Ar. Lines produced in both He and Ar show a pseudo-gaussian profile, however the lines produced in He have a much larger height and lower full width at half maximum (FWHM) compared to the lines produced in Ar. The lower FWHM of lines produced in He is a result of more aerodynamic focusing that occurs for smaller NPs in He[70].

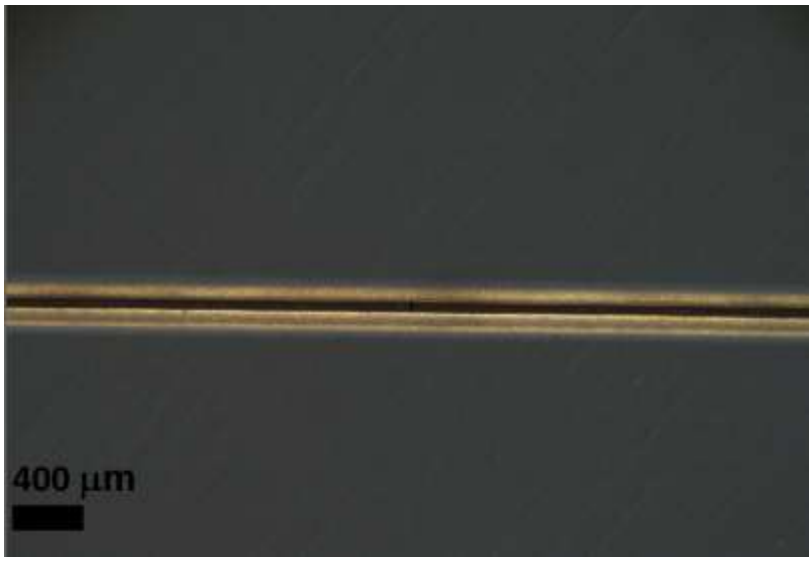

Figure 18: Plan-view optical micrograph of a line produced in He carrier gas

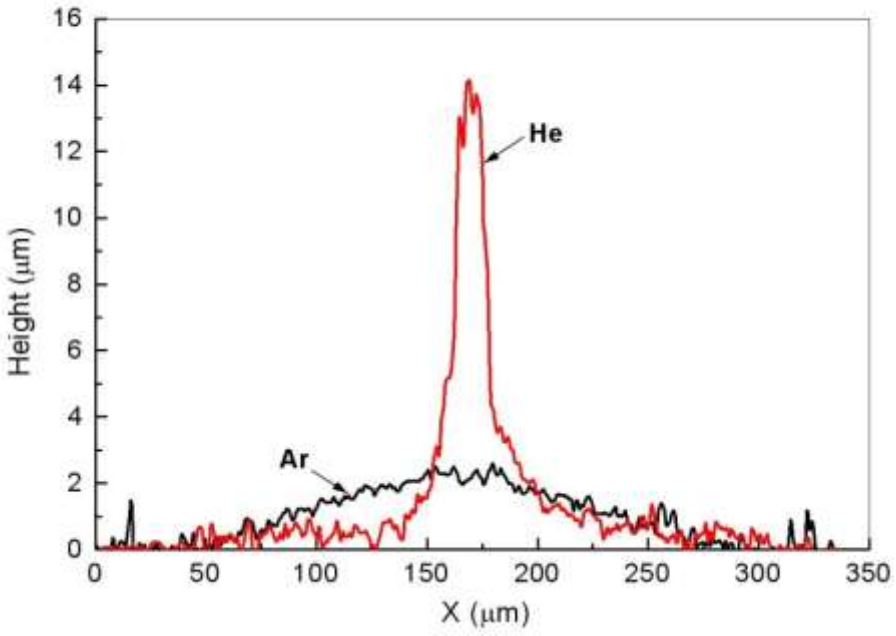

Figure 19: Cross-sectional profiles of films deposited using He and Ar as the carrier gasses

4.4 Influence of Feed Rate

4.4.1 Nanoparticle Morphology

A systematic study of the degree of agglomeration with feed density of MPs has been reported by Gleason[26] Figure 20 shows the TEM micrographs of NPs produced for the current work at feed rates higher than 10 mg/hr. The constituent NPs in the agglomerates are of the same mean size as the individual NPs formed at lower feed rates

(shown in Figure 16). The NPs show significant neck growth in the agglomerates, indicating either room temperature sintering occurs or sintering occurred as a result of heat generated from the LAMA process. Given the size of the necks in the sintered agglomerates, the agglomerates that are produced can be considered "hard," i.e. they do not break on impaction.

Heat can be generated in the LAMA process during impaction, during shockwave generation or by stray radiation produced by scattering during ablation. To test whether impaction was the reason for the observed NP sintering, agglomerated NPs were collected using an electrostatic setup, where the NPs were impacted at much lower velocities (less than 100 m/sec) and where heating effects would therefore not be expected to be significant. The details of the setup are described elsewhere[71]. Figure 20 shows an example of an agglomerate collected electrostatically which shows that the agglomerate consists of sintered NPs. This suggests that sintering did not occur due to heating from impaction. Heating during shockwave generation is also not likely since NPs cool very quickly after ablation and are expected to retain their charge caused by thermal and photoionization from the laser and therefore not agglomerate before they cool. Room temperature sintering has been observed in NPs previously[72] and the NPs produced in our work bear a striking resemblance with NP agglomerates produced at room temperature reported by Weber *et al.*[73], suggesting that room temperature sintering is likely responsible for our observed agglomerate morphologies. It is possible that scattered radiation from the ablation process also contributes to the sintering of NPs in the LAMA process, but we did not measure this effect separately in our studies.

a)

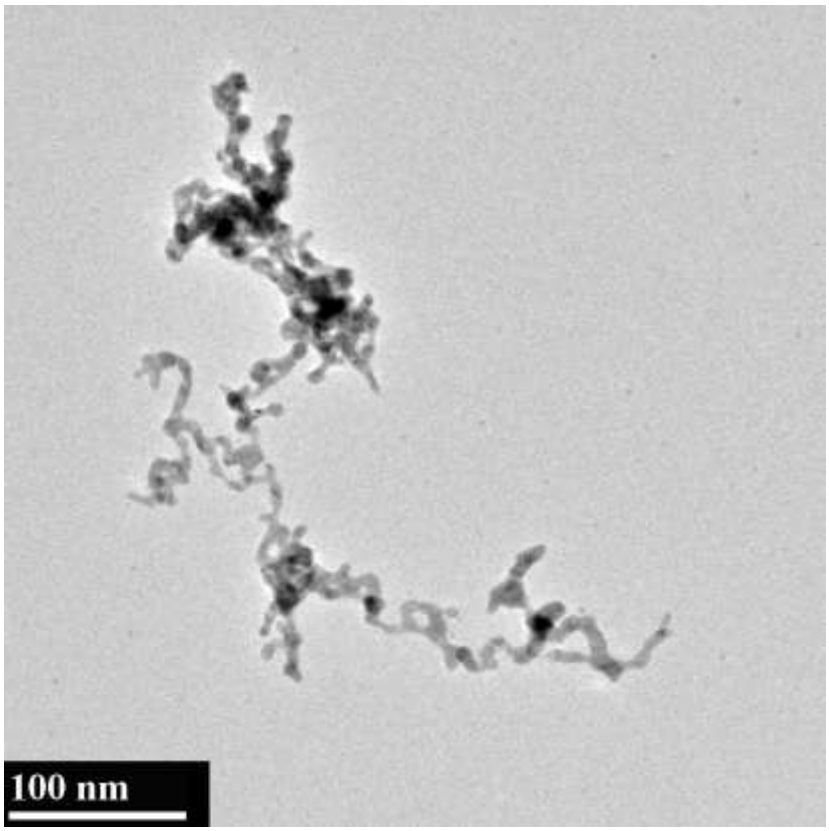

Figure 20: TEM images of agglomerates produced in a) He and b) Ar, produced at a MP feed rate of 50 mg/hr

b)

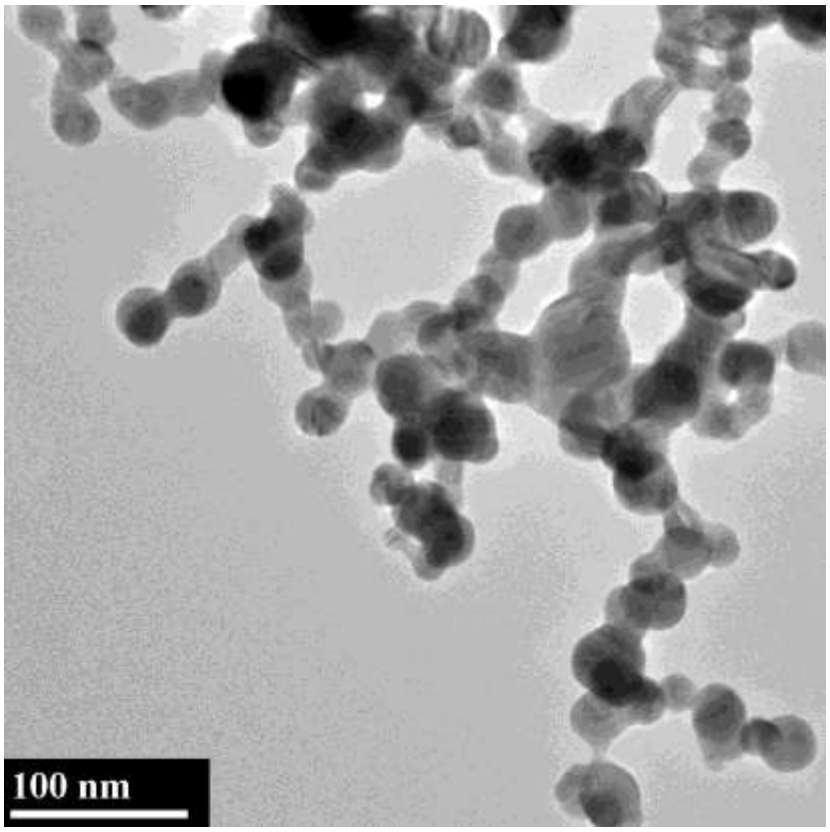

Figure 20:TEM images of agglomerates produced in a) He and b) Ar, produced at a MP feed rate of 50 mg/hr

4.4.2 Influence of MP feed rate on macroscopic features of the deposits

Figure 21 shows plan-view optical images of lines made at different feed rates. While the lines produced at a feed rate of 10 mg/hr do not show any large agglomerates, the films produced at a higher feed rate show large agglomerates, which appear in these optical images as dark, irregularly shaped spots. The largest of these agglomerates are

possibly the result of build up of powder inside of the virtual impactor. As the build up grows, it can become unstable, fracture, and then become entrained in the flow gas so that it is subsequently is deposited within the films.

a)

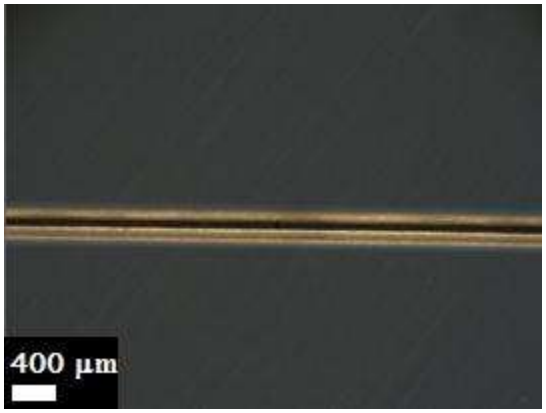

b)

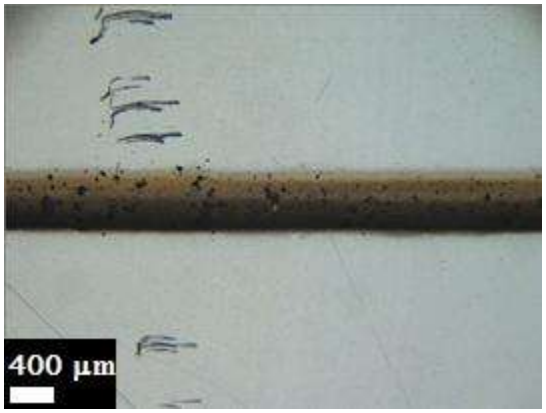

Figure 21: Plan-view optical micrographs of Ag lines produced at feed rates of a) 10 mg/hr, b) 20 mg/hr, and c) 50 mg/hr

c)

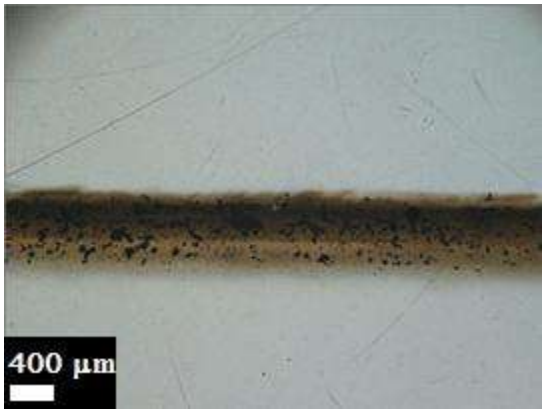

Figure 21: Plan-view optical micrographs of Ag lines produced at feed rates of a) 10 mg/hr, b) 20 mg/hr, and c) 50 mg/hr

4.5 INFLUENCE OF NUMBER OF PASSES AND DEPOSITION SPEED

The number of deposition passes and deposition speed were found to have an effect on the uniformity of the cross-sectional area of the lines. As the deposition speed or the number of passes was decreased, the uniformity in cross-sectional area decreased. We did not attempt to quantify the non-uniformity. However we performed sufficient experiments to determine empirically that at a speed of 635 mm/s and 32 passes, the lines were fairly uniform in cross-section area. This then became the standard condition used to deposit the majority of the films used for sintering and conductivity measurements.

4.6 Delamination of Films

Figure 22 shows the height versus position for cross sections of the lines before and after annealing and Figure 23 shows a low magnification SEM micrograph of a film after annealing. These figures show that, upon annealing, the films delaminated in the region near the center of the cross-section. However, the edges of the films where they were the thinnest maintained good adhesion with the substrate.

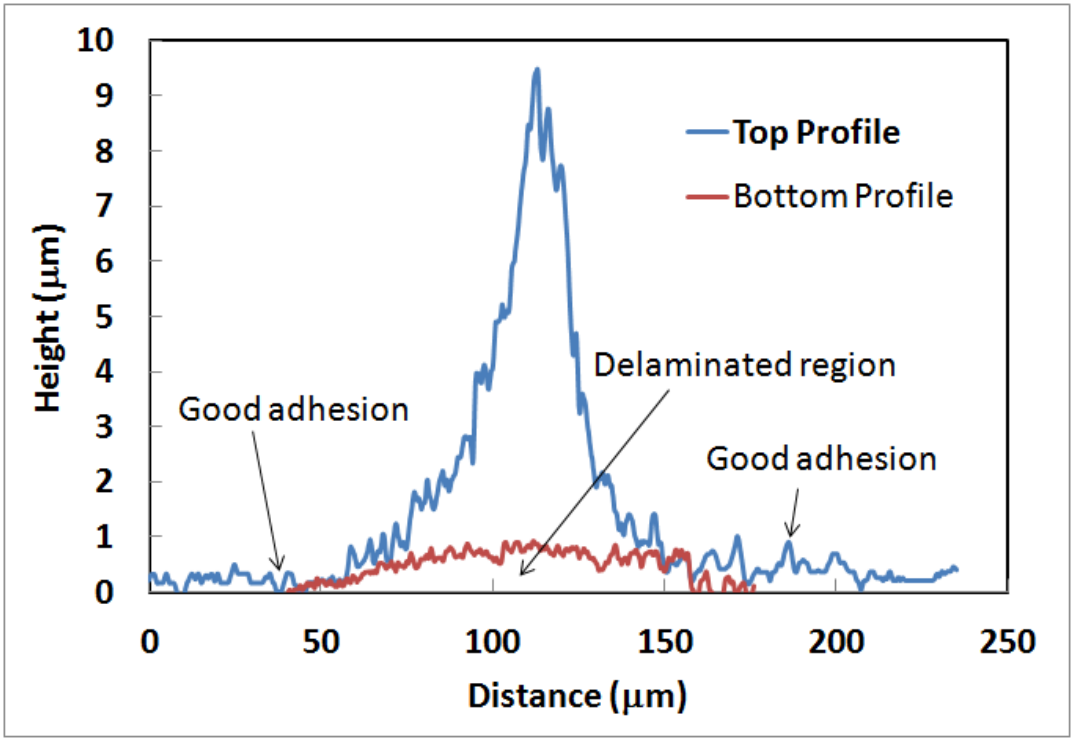

Figure 22: Top and bottom profiles of a line obtained using an optical profilometer after annealing showing that the bottom profile (red) lifted off the surface of the substrate as result of delamination

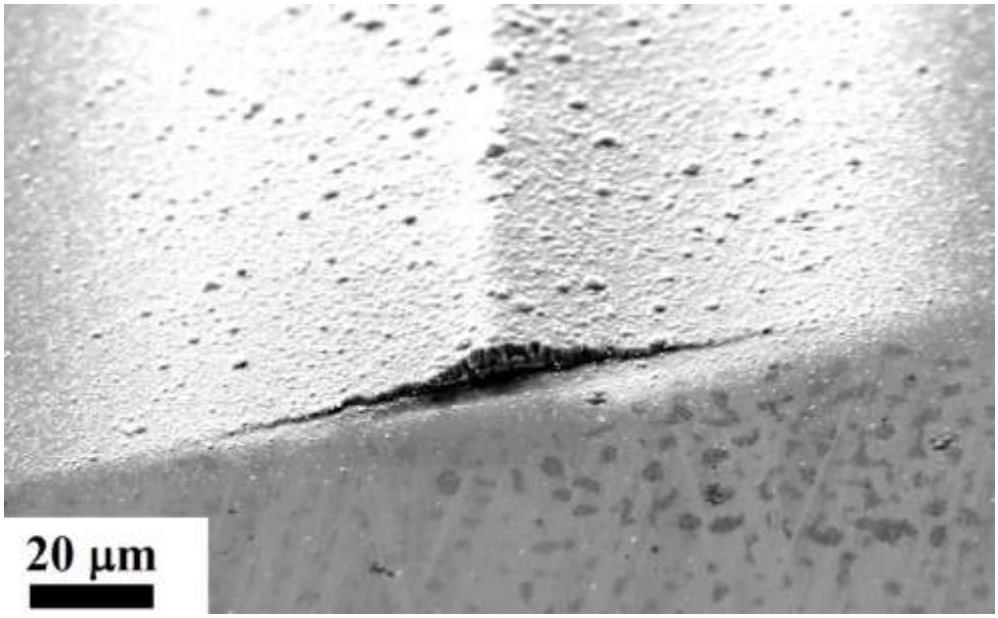

Figure 23: SEM micrograph of line after annealing showing a region near the center of the profile where delamination is apparent

This effect of thickness on the delaminated area was studied by depositing a line on a masked substrate. Figure 24 shows a plan-view SEM micrograph of one such line, and it is apparent from the figure that only the thickest portions of the line delaminated.

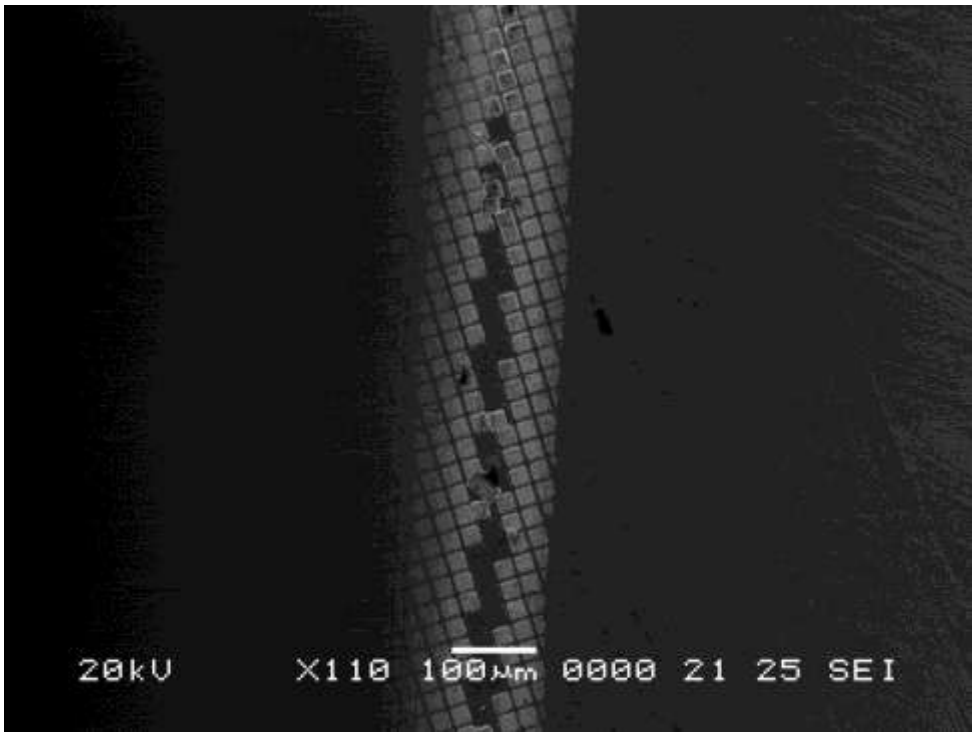

Figure 24: SEM image of a line that was deposited on a masked substrate, annealed and then subsequently brushed to reveal which regions delaminated

From a technological perspective, when the lines are wide enough (greater than 500 μm), they maintain good adhesion to the substrate and survive the industry standard scotch tape test[74]. Figure 25 gives an example of a wide line which delaminated in the region near the center of the cross-section but that was wide enough that the thinner bonded regions of the film provide enough support to survive the scotch tape test.

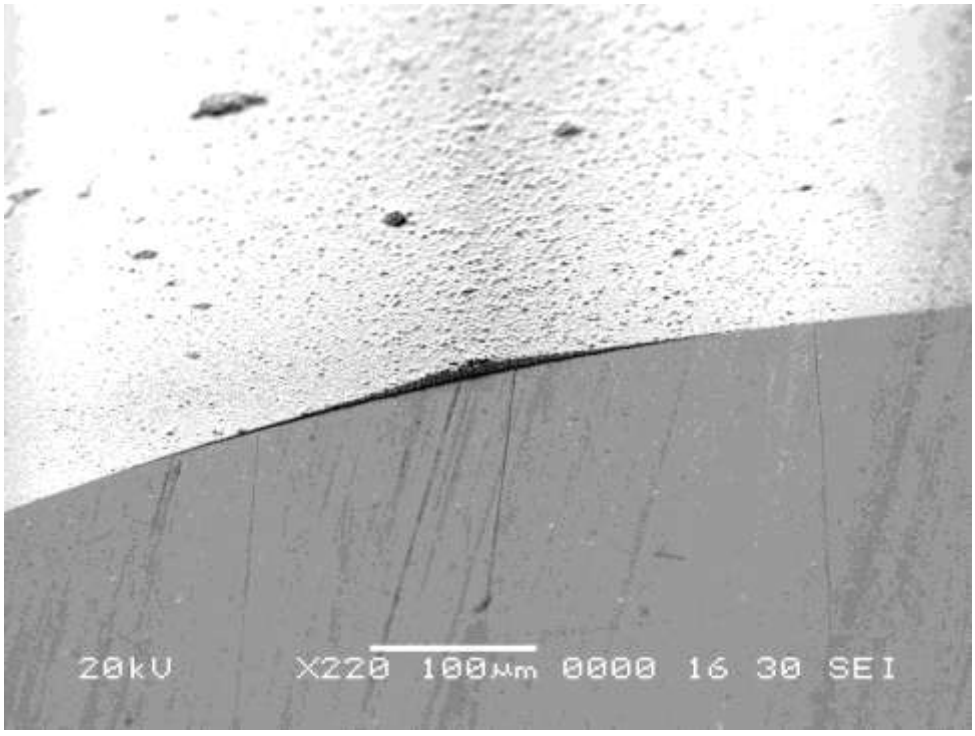

Figure 25: SEM micrograph of the cross-section of a wide line that survived the industry standard scotch tape test

4.7 FILMS PATTERNED ON PLASTIC AND PAPER

To demonstrate the capability to pattern films on low temperature substrates, lines were deposited on plastics and paper. Figure 26 shows an image of two such films. These films maintain their conductivity after folding and unfolding the substrates.

 b) 

Figure 26: Pictures of films made on a) thin paper, b) plastic

Chapter 5: Influence of Annealing Treatment

As discussed in Chapter 4, patterned lines produced in He carrier gas at a MP feed rate of 10 mg/hr produce unagglomerated NPs with a 6 nm mean particle size. The velocity of NPs in a He carrier gas is 900-1200 m/s and, at these high velocities, the deposited films are packed to high densities. The films produced with these deposition conditions do not suffer from factors that inhibit sintering such as NP agglomeration and low initial density, and thus the films are ideal for realizing the true sintering behavior of NPs. Moreover, the small dimensions of NPs produced in He make it possible to observe low temperature sintering in reasonable times, in accordance with the Herring's law[54].

This chapter presents an experimental study of the effect of annealing temperature on the final properties of such sintered films – density, microstructure and conductivity. Inferences about the dominant diffusion mechanism at different temperature ranges for low temperatures are made from the experimental data and are reported in Section 5.4. The kinetics of sintering is experimentally evaluated in Sections 5.5 and 5.6. The effects of a two-step annealing treatment on the final microstructure and conductivity are evaluated in Section 5.7.

5.1 Effect of Rapid thermal Annealing

Samples were rapid thermally annealed for 5 minutes at 5 different temperatures ranging from 75 ^{o}C – 250 ^{o}C. Lines were deposited onto glass substrates to measure changes in density and conductivity, and samples were made on Si substrates to observe microstructural changes.

5.1.1 Microstructure

Plan-view SEM images of the as-deposited and annealed samples are shown in Figure 27. The microstructure exhibits relatively low levels of porosity. The grain sizes of the as-deposited films and films annealed at 100 ^{o}C and below are too small to be measured accurately using SEM and thus were not evaluated.

a)

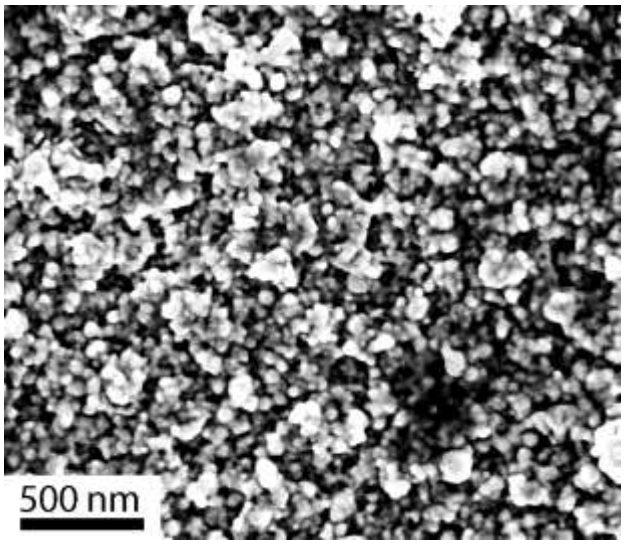

b)

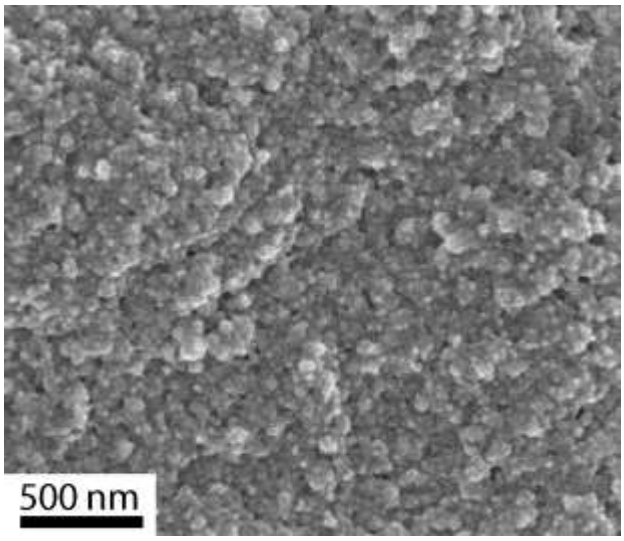

Figure 27: Plan-view microstructures of lines a) as-deposited and rapid thermally annealed at b) 100 ^{o}C, c) 125 ^{o}C, d) 150 ^{o}C, e) 200 ^{o}C, and f) 250 ^{o}C

c)

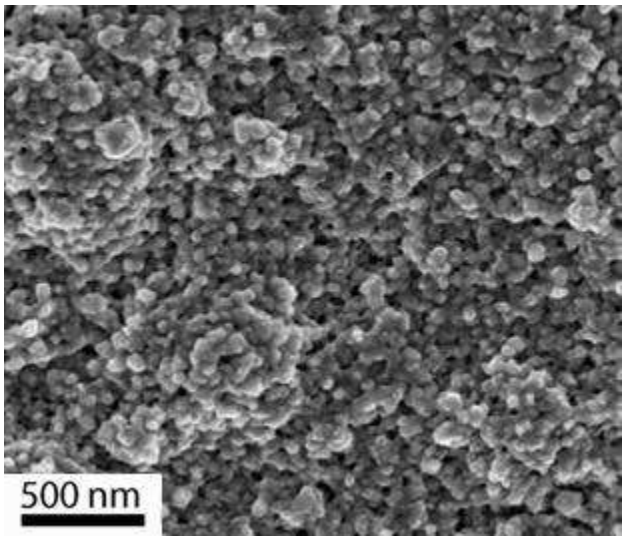

d)

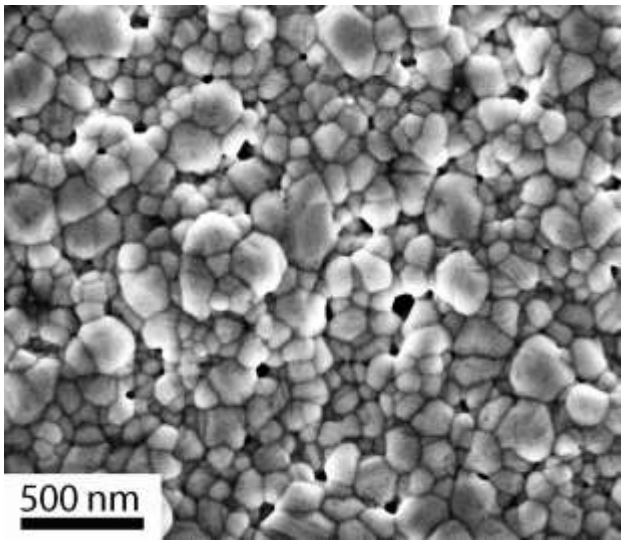

Figure 27: Plan-view microstructures of lines a) as-deposited and rapid thermally annealed at b) 100 ^{o}C, c) 125 ^{o}C, d) 150 ^{o}C, e) 200 ^{o}C, and f) 250 ^{o}C

e)

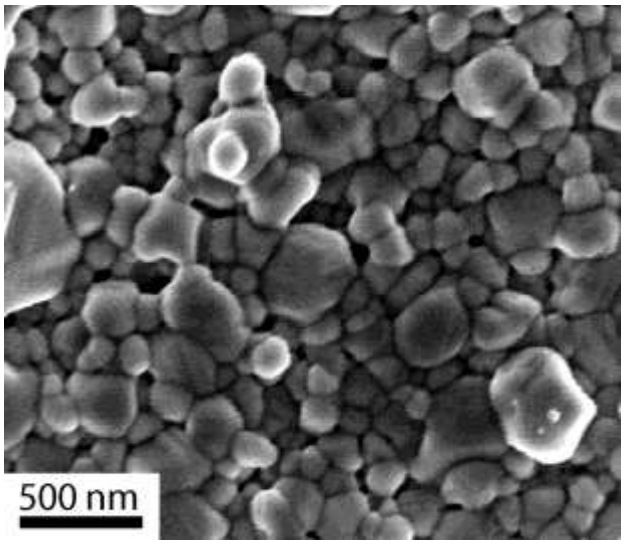

f)

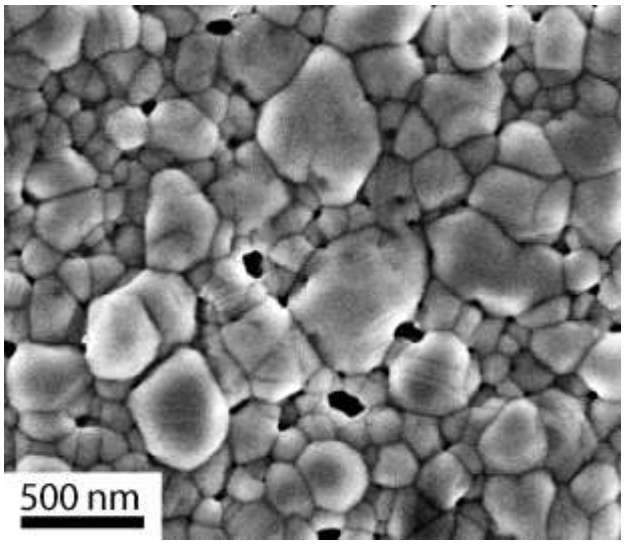

Figure 27: Plan-view microstructures of lines a) as-deposited and rapid thermally annealed at b) 100 ^{o}C, c) 125 ^{o}C, d) 150 ^{o}C, e) 200 ^{o}C, and f) 250 ^{o}C

Figure 28 shows the effect of annealing temperature on grain size. The mean grain size of the as-deposited sample was taken to be 6 nm based on our observations from

TEM of individual NPs produced by LAMA under similar processing conditions (It is assumed that the particle size does not change upon impaction.). The mean grain size of the samples annealed at 100 ^{o}C was measured to be ~ 23 nm. Note that the error in measuring the grain size for this sample was much higher compared to those measured subsequent to annealing at higher temperatures because of the difficulty in imaging such fine grains using a SEM.

Both the conductivities and the densities of samples annealed at temperatures below 100 ^{o}C showed no difference compared to the conductivities and densitites measured in as-deposited lines. In contrast, the relative conductivity of the sample annealed at 100 ^{o}C increased slightly by 2.7 % (from 19.58 to 20.25% conductivity of bulk Ag), and is discussed in more detail in Section 5.1.3. Although we cannot observe measurable changes in the grain sizes for samples annealed at 75 ^{o}C, the small change in conductivity at this annealing temperature is consistent with either very small or no change in grain size during annealing at this temperature.

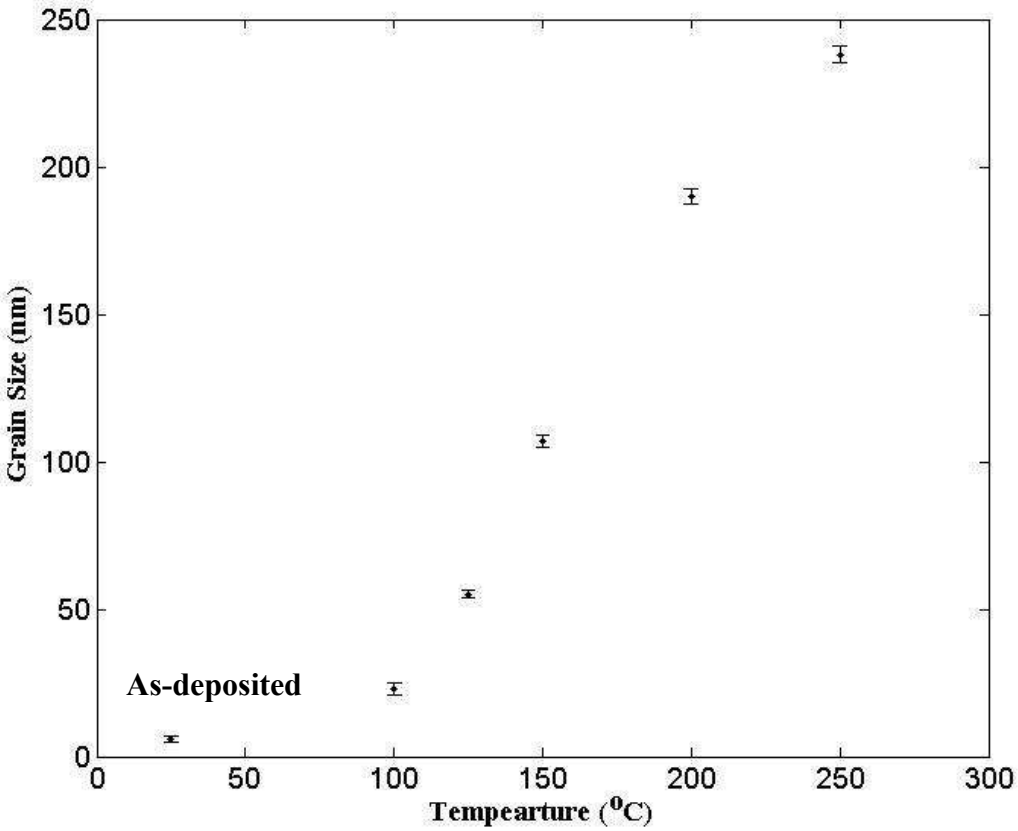

Figure 28: Grain size vs Annealing Temperature for line deposited in He carrier gas

It is apparent from Figure 27 and Figure 28 that significant microstructural changes are observed at annealing temperatures of 125 ^{o}C and up, as the grain size increases abruptly at this temperature.

5.1.2 Density

The relative density of the as-deposited samples was measured to be 70% of the bulk density for Ag. Because the lines are bonded to the substrate, they are not free to shrink

in the plane of the substrate; they can only reduce their volume by decreasing their thickness in the out of plane dimension. Thus, to determine the density of the annealed samples, the change in cross-sectional area after annealing was measured using an optical profilometer. The relative density of the annealed samples was determined from,

$$\rho / \rho_{Ag} = 70\% \cdot (A_i/A_f) \qquad \text{Equation 12}$$

where ρ is the density of the line, ρ_{Ag} is the density of Ag, A_f is the final cross-sectional area after annealing, and A_i is the cross-sectional area of the as-deposited film. The as-deposited relative density is taken to be 70% for samples deposited using helium based on our experimental measurements, as discussed previously.

Figure 29 shows relative density versus annealing temperature for lines deposited using helium. While the densities of samples remain unchanged at temperatures lower than 100 ^{o}C, there is significant densification beginning at 125 ^{o}C and increasing with annealing temperature. Above 150 ^{o}C, the lines densify to near theoretical densities (>95% of theoretical density). It should be noted that there is a minimum change in density that is detectable due to the resolution limitations of the optical profilometer and associated difficulties in accurately measuring the location of the bottom of the line by imaging through the transparent substrate. In practice this minimum detectable change in relative density is ~ 10 %. This experimental uncertainty places an upper bound on the temperature at which densification occurs; samples annealed below 100 ^{o}C may exhibit changes in density that are below the detection limits.

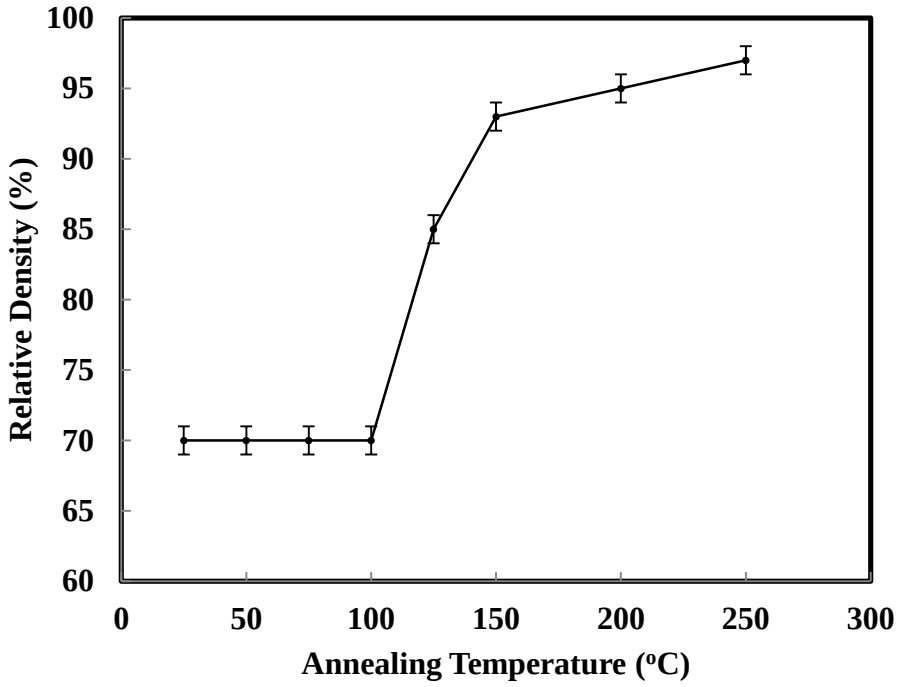

Figure 29: Density versus annealing temperature for lines deposited in He carrier gas

5.1.3 Conductivity

The measured conductivities of the as-deposited and annealed samples as a function of temperature are shown in Figure 30. It is apparent from the figure that the conductivities of the silver films do not show any significant change until an annealing temperature of 100 °C is reached. For lines annealed at temperatures above 100°C, the conductivity increases quickly, reaching ~ 31 % for lines annealed at 125 °C and ~ 46 % for lines annealed at 150 °C. The conductivity for lines annealed above 150 °C are

dramatically higher than lines and films processed in this temperature range (150-250 ^{o}C) using other methods[75].

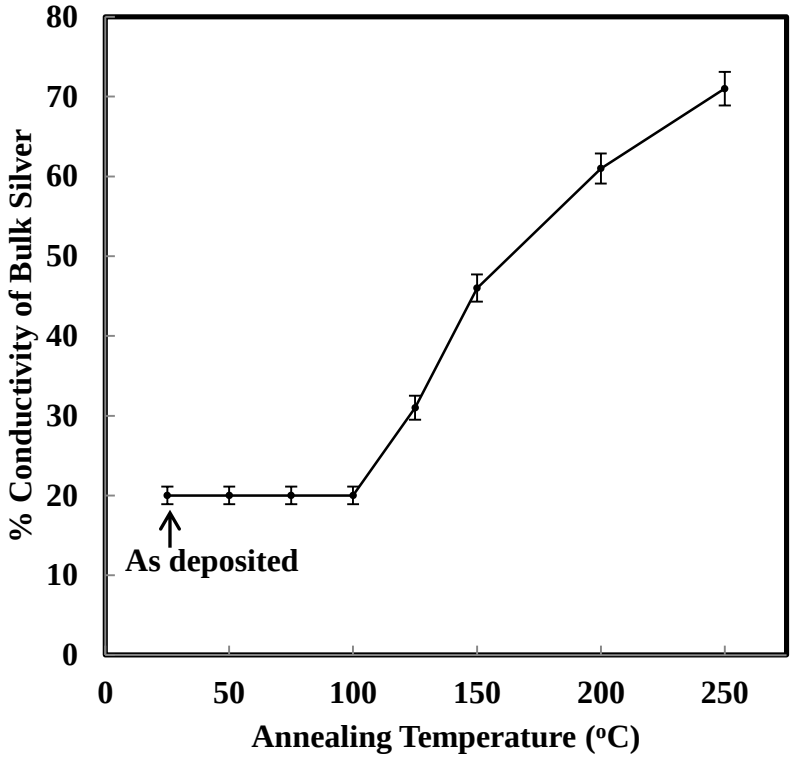

Figure 30: Conductivity versus annealing temperature for lines deposited in He carrier gas

5.2 Inference on Diffusion Mechanisms

From Section 5.1, it is apparent that the densities, conductivities and the grain sizes of the silver lines do not change significantly until annealing temperatures of at least

100 °C are reached. Appreciable changes are observed for films annealed at 125 °C, and even larger changes are observed for films annealed at 150 °C and higher. The observed experimental data suggests that two distinct temperature transitions occur, first at about 100˚C, and again at about 150˚C. From the analysis presented in Chapter 2, we predicted that two distinct temperature transitions should occur that were associated with transitions from surface diffusion-dominated sintering at low temperature to grain boundary diffusion-dominated sintering at higher temperatures and we termed these transitions T_c and T_d. The abrupt change in sintered density and the associated increase in conductivity, suggests that the temperature T_d is ~150 °C and the observation of no appreciable densification at 100 °C suggests T_c is ~100 °C for silver.

5.3 SINTERING KINETICS IN GRAIN BOUNDARY DIFFUSION DOMINATED REGIME

In the previous section we established that T_d is ~ 150 °C. An evaluation of the conductivities and densities of films annealed at T_d as a function of time should give further insights into the kinetics of sintering in the grain boundary diffusion-dominated regime. To assess these changes, films consisting of non-agglomerated NPs produced by maintaining a feed rate of 10 mg/hr were produced on glass and Si substrates and were rapid thermally annealed at 150 °C. The final densities and conductivities of the sintered films were evaluated as a function of annealing time.

5.3.1 Density

The density of the films increased to 93 % relative density in the first 2 sec of annealing at 150 °C and remained virtually unchanged thereafter. This shows that virtually all of the densification occurs very quickly at 150˚C.

5.3.2 Conductivity

Figure 31 shows a plot of conductivity of the film measured at different annealing times.

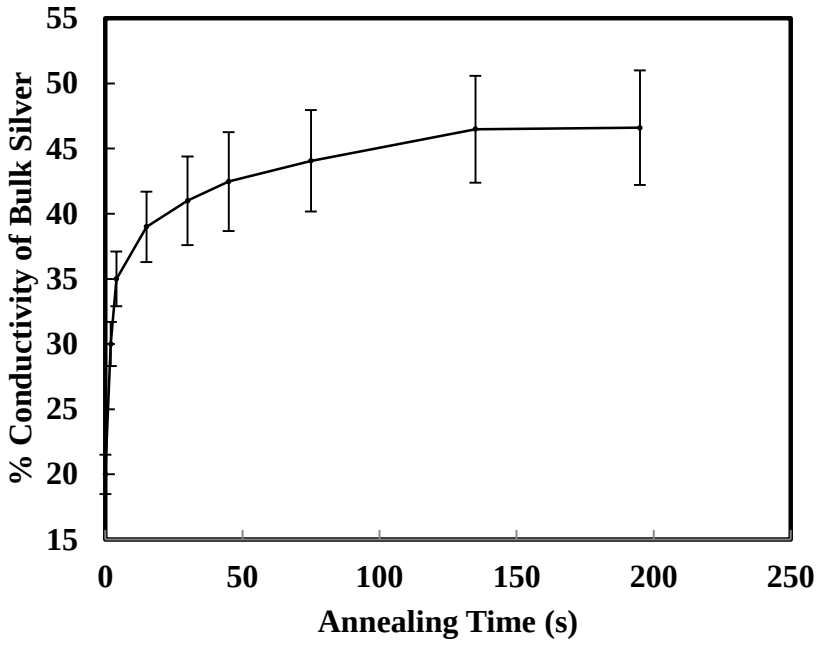

Figure 31: Conductivity versus annealing time for films annealed at 150 °C

From the density and conductivity data, it is apparent that almost all of the densification occurs within the first 2 seconds of annealing. Subsequent increases in conductivity after the first 2 seconds are due to grain growth.

5.4 SINTERING KINETICS IN THE SURFACE DIFFUSION DOMINANT REGIME

In Section 5.2 we established that T_c is ~ 100 ^{o}C. An evaluation of the microstructures, conductivities and densities of lines annealed at T_c as a function of time should give further insights into the kinetics of sintering in the surface diffusion-dominated regime. Lines consisting of non-agglomerated NPs produced by maintaining a feed rate of 10 mg/hr were produced on glass and Si substrates and were annealed at 100 ^{o}C and held at three different holding times of 5 min, 1 hr and 16.5 hrs. The microstructures, densities and conductivities of the sintered lines were evaluated as a function of holding time.

5.4.1 Microstructure

The plan-view SEM images of the annealed samples are shown in Figure 32. While the grain size is too small to be measured accurately for annealing times of 5 minutes, it is clearly evident that significant grain growth for samples heated for 1 hour and 16.5 hours.

a)

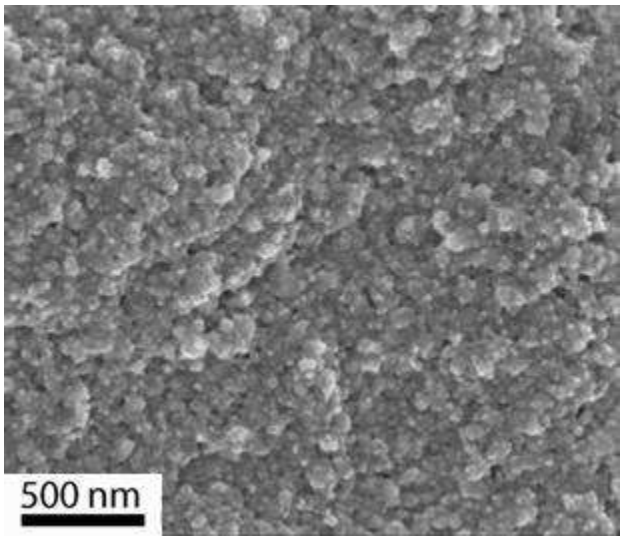

b)

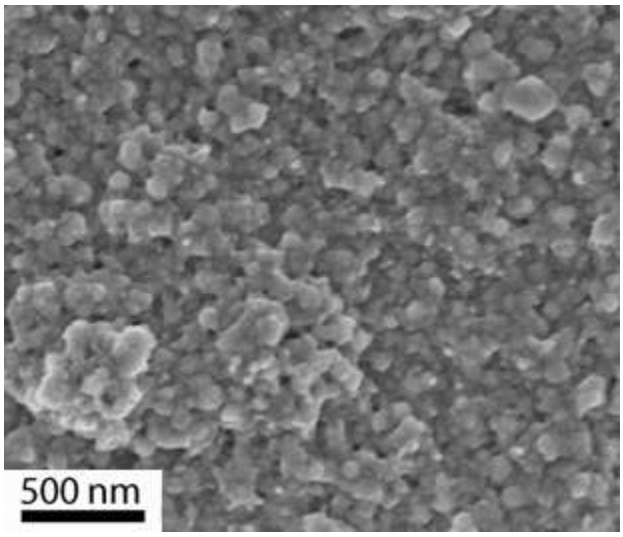

Figure 32: Plan-view SEM images of lines heated at 100 ˚C for a) 5 min, b) 1 hr, and c) 16.5 hrs

c)

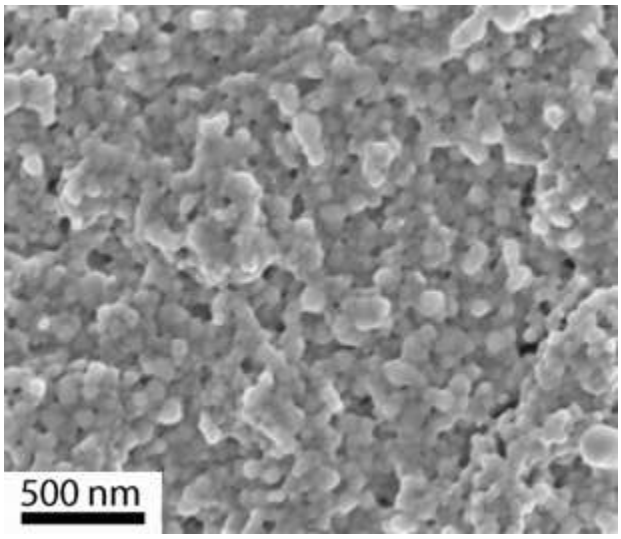

Figure 32: Plan-view SEM images of lines heated at 100 ˚C for a) 5 min, b) 1 hr, and c) 16.5 hrs

5.4.2 Density

The annealed samples showed no measureable change in density for any of the annealing times, confirming the dominance of surface diffusion.

5.4.3 Conductivity

Figure 33 shows the measured conductivities a function of annealing time for lines annealed at 100˚C.

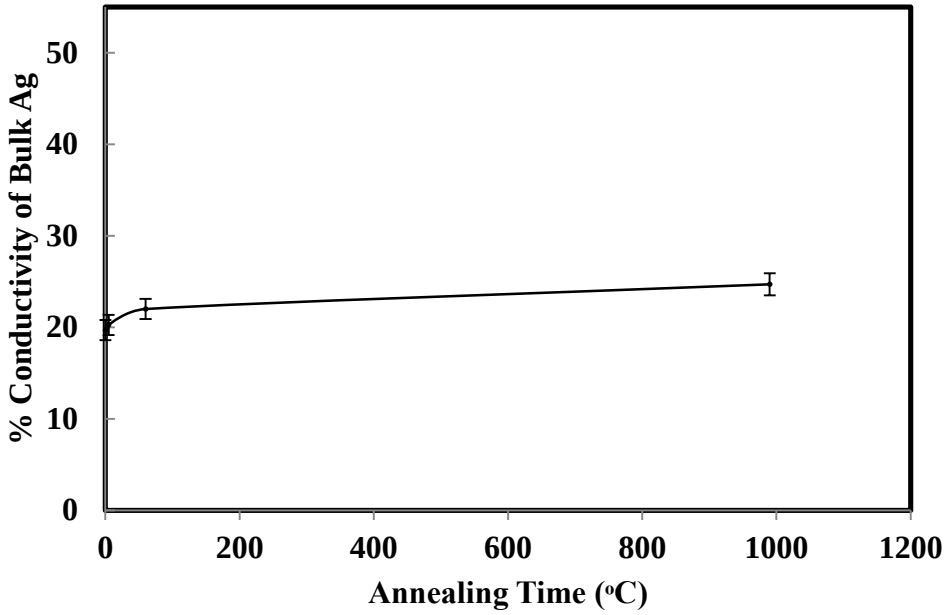

Figure 33: % Conductivity relative to bulk silver versus annealing time for lines annealed at 100 °C, for a) 0 sec, b) 5 min, c) 60 min, d) 990 min.

The above results show clearly that no densification occurs at temperatures lower than 100 °C, and that the slight increase in conductivity that is observed is due only to grain growth. The results thus confirm that Γ is much lesser than 1 at °100 °C.

5.5 TWO-STEP ANNEALING TREATMENT

An annealing treatment in the low temperature surface diffusion-dominated regime will change the driving force for further sintering in the grain boundary diffusion dominated regime. The reduction in the driving force is dependent on the sintering kinetics, which is in-turn governed by the surface diffusivity D_s, and the time spent in the

low temperature regime. The effect of heating rate on sintering can be used to evaluate this effect. However, D_s increases with temperature and thus the maximum reduction in the driving force is expected at *Tc*. This suggests that a more controlled experiment to evaluate this effect is a two- step annealing treatment. We therefore performed annealing treatments first at 100 ^{o}C (T_c) for 5 min, and then subsequently for 5 min at 150 ^{o}C (T_d). The final relative densities of the lines after the two-step annealing were found to be 80%. This compares to a measured relative density of 93% when the lines were subjected to a single-step annealing temperature at only 150 ^{o}C. Similarly the conductivities of the lines were found to be 37% after the two step- annealing treatment, compared to 46% for films annealed at 150 ^{o}C only. The final microstructures of the lines after both annealing treatments is shown in Figure 34 a). From these micrographs, it is apparent that the grain sizes are finer for lines subjected to the two-step annealing treatment compared to films annealed at 150 ^{o}C only.

a)

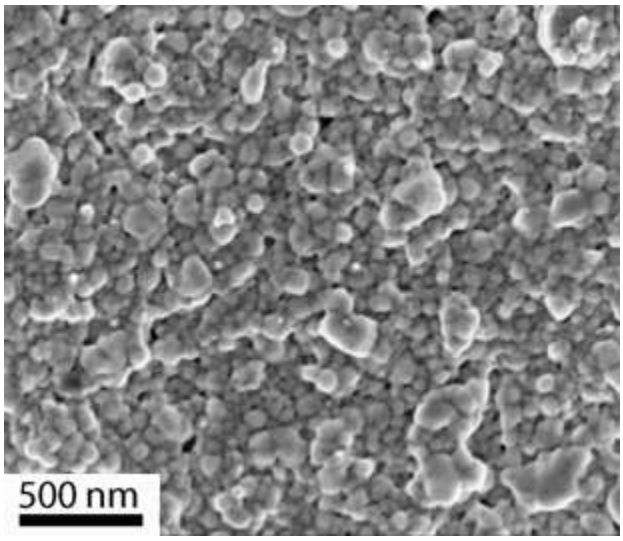

b)

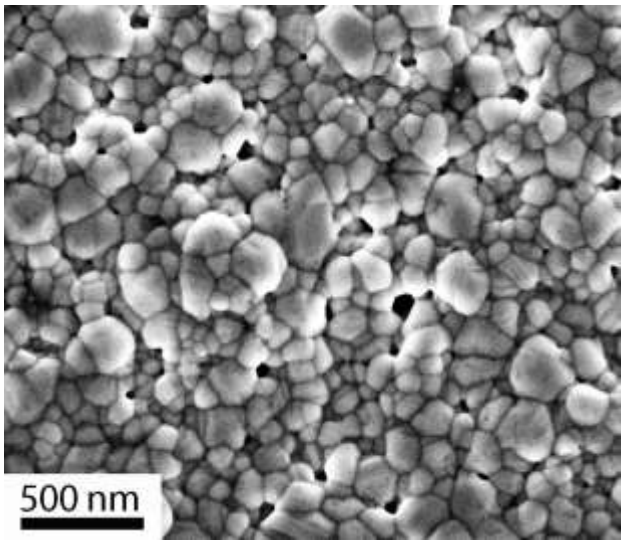

Figure 34: a) Plan view microstructure of a line after a two-step annealing treatment where it was initially annealed at 100 °C for 5 min and subsequently annealed at 150 °C for 5 min. b) Plan view microstructure of a line give a single rapid thermal annealing treatment at 150 °C for 5 min,

5.9 CONCLUSIONS

In this chapter we have presented an experimental study of the effects of low temperature annealing treatment on the evolution of microstructures and conductivities of nanoparticulate silver thick films. The experimental work reported in this chapter utilizes organic dispersant-free, non-agglomerated, high initial density nanoparticulate films. The results establish that two distinct temperature transitions exist; one transition occurs at about 100 ^{o}C and a second transition occurs at about 150 ^{o}C. These critical temperatures are associated with transitions from surface to grain boundary-dominated sintering. Lines do not show any measurable densification at temperatures below 100 ^{o}C but densify to near full densities when rapid thermally annealed at temperatures of 150 ^{o}C or above. The films annealed at 150˚C exhibited much higher conductivities compared to films processed from powders at similar temperatures using other processes that produce powder particles that are capped by organics, agglomerated, or have lower initial densities. An evaluation of the sintering kinetics in the grain boundary diffusion dominated regime suggests that nearly all of the densification occurs within 2 seconds, followed by grain growth.

The effects of a two-step annealing treatment on the final microstructures, densities and conductivities were studied. Lines were given an initial annealing treatment in the surface diffusion dominant regime and a second treatment in the grain boundary diffusion dominant regime. The results show that annealing in the surface diffusion dominant regime reduces the driving force for further densification and grain growth in

the grain boundary diffusion dominant regime. These experiments provide a qualitative understanding of the effect of heating rate on the properties of the sintered products.

Chapter 6: Modeling

This chapter presents a model describing the evolution of conductivity and microstructure as a function of critical characteristics of the annealing treatment. The evolution of microstructure is described in terms of grain size, density, and grain size-density trajectory. This model allows individual processing parameters to be evaluated to determine their influence on sintering and conductivity. It is important to point out that experimentally it is usually not possible to isolate individual influences because processing parameters usually result in multiple simultaneous effects. Thus, the model allows information that cannot be obtained purely from experiments to be studied.

The sintering processes are complex and theoretical models require parameters that are not easily obtained[44]. In this study, this issue is addressed by using a fitting parameter to model the sintering behavior of real systems. The patterned films produced in this work are well suited for developing a comprehensive model that is capable of predicting the full range of possible sintering behaviors since, unlike other processing routes, they do not suffer from major deleterious factors that inhibit sintering. The fitting parameters extracted from the experimental data from such films are therefore likely to represent the true sintering behavior. Furthermore, the use of very fine NPs in our work allows us to observe the effects of annealing at low temperatures in reasonable times.

6.1 Dependence of Conductivity on Density and Grain Size

Grain boundaries and pores are assumed to be the only major electron scattering sources for thick films[27], and thus, the conductivity of the films are assumed to be dependent only on the bulk conductivity, density and grain size[27]. Note, we neglect the effect of other defects such as dislocations on electron scattering in this work because no significant defects other than some twinning were observed in the films.

The effect of density on conductivity can be evaluated by applying the Bruggeman effective medium approximation[30], which gives the effective medium conductivity:

$$f_v\left[\frac{1-\sigma_{EM}}{1-2\sigma_{EM}}\right] = (f_v - 1)\left[\frac{\sigma_{gb}-\sigma_{EM}}{\sigma_{gb}+2\sigma_{EM}}\right] \qquad \text{Equation 13}$$

where,

f_v is the void fraction, and f_v = 1-ρ, where ρ is the fractional density

σ_{gb} is the grain boundary conductivity,

σ_{EM} is the effective medium conductivity

Equation 13 gives two roots, one of which has a non-physical value and should be ignored[30].

The effect of grain size on conductivity can be evaluated from the dependence of grain boundary scattering on conductivity proposed by Maydas and Shatzkes[29]. The ratio of grain boundary conductivity, σ_{gb}, to bulk conductivity, σ_{bulk}, is given by:

$$\frac{\sigma_{gb}}{\sigma_{bulk}} = 3[\frac{1}{3} - \frac{1}{2}\alpha + \alpha^2 - \alpha^2 \ln(1 + \frac{1}{\alpha})] \quad \text{Equation 14}$$

where,

$$\alpha = \frac{\lambda}{D}\left[\frac{R}{R-1}\right] \quad \text{Equation 15}$$

λ is the mean free path of electrons in the medium,

R is the reflection coefficient, and

D is the grain size

R can be fitted to experimental data and gives a measure of the grain boundary scattering[76]. These two models can be combined and used to calculate the conductivity of thick films with known density and grain size. Note, Equation 14 utilizes the mean free path of electrons for bulk Ag. While the mean free path is known to be 51±1 nm for coarse-grained Ag, the mean free path is not known accurately for Ag with finer grains[8,77,78,79]. We therefore use the conductivity, grain size and density data for films only with grain sizes larger than 50 nm to fit the reflection coefficient for our annealed films. As shown in Chapter 5, this corresponds to films annealed above 125 °C. Table 2

summarizes the annealing temperatures, conductivities, grain sizes and density data used to obtain *R*:

Table 2: Experimental data used to find *R* in Equation 14.

Annealing Temperature (°C)	Grain Size (nm)	Relative Density (%)	% conductivity of Bulk Silver
125	55 ± 1.2	85	31 ± 1.5
150	107 ± 1.89	93	47 ± 1.7
200	190 ± 2.44	95	61 ± 1.8
250	238 ± 2.88	97	71 ± 2.1

A value of R = 0.558 ± 0.0128 was obtained using a least squares fit of the experimentally obtained values of conductivity and the predicted values of conductivity obtained using Equations 13-15 and from the experimentally known values of density and grain size. Once R is known, the conductivity can be predicted using Equations 13-15. The procedure for calculating the error in the fitting parameter R is given in Appendix A.

Figure 35 shows this prediction and on the same plot, results from experiments are shown. The figure shows that there is excellent agreement between the model predictions and the experiments when R = 0.558 is used.

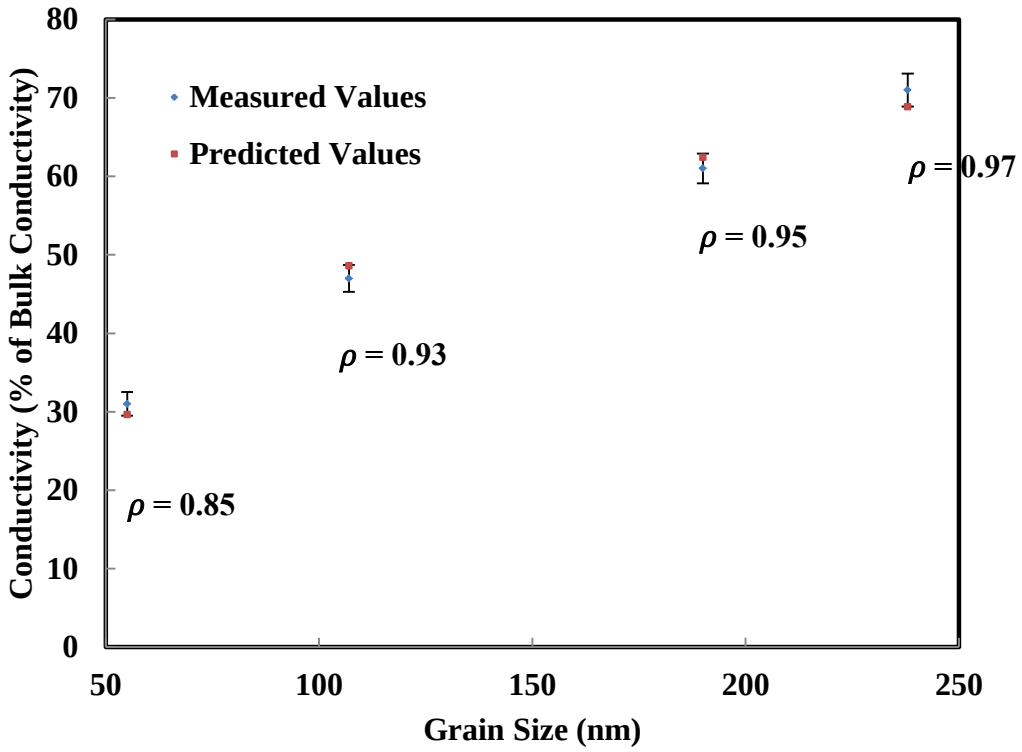

Figure 35: Comparison of the predicted conductivity using R = 0.558, and measured conductivity

With the value of *R* determined, it is possible to use Equations 13- 15 to compute the conductivity of thick films of silver as function of grain size and density. Figure 36 shows such a plot with constant conductivity contours superimposed on the plot. This plot reinforces the concept that the conductivity for thick films is determined by both the relative density of the film and the grain size. Grain size has a more dominant effect at fine grain sizes and density has a larger effect for coarser grain sizes.

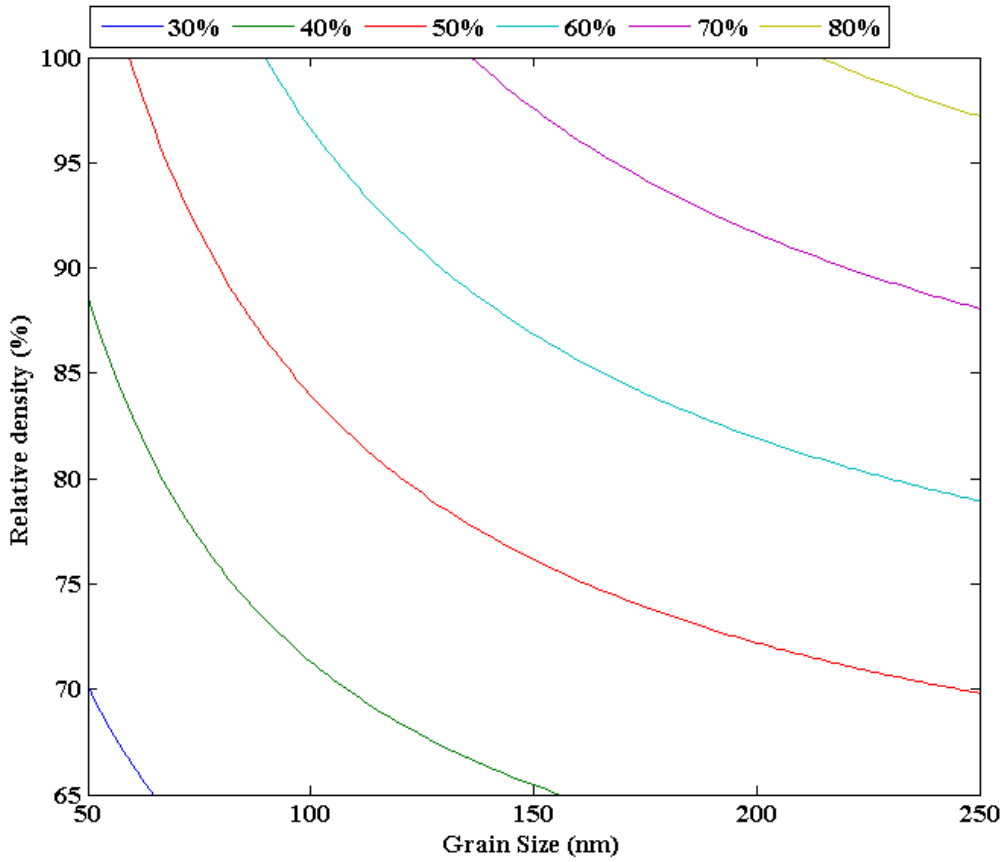

Figure 36: Plot of relative density (expressed as % conductivity of bulk silver) versus grain size with constant conductivity contours superimposed ranging from 30 – 80% of the bulk conductivity of Ag

Since, the final density and grain size of an annealed powder compact is directly related to the annealing temperature and time of annealing, these curves can aid in the design of the annealing treatment that can achieve the desired conductivity. In the next section we use theoretical considerations to evaluate the effects of annealing treatment on the grain size and density.

6.2 Dependence of Grain Size and Density on Annealing Temperature and Time

In the intermediate and final stages of solid state sintering, both grain growth and densification occur simultaneously. It is thus essential to consider both processes to understand and control sintering. A theory of simultaneous densification and grain growth was given by Yan *et al*[48]. They predicted the grain size-density trajectory (Grain size versus density) based on existing models of grain growth and densification[47,50]. We use a similar analysis, but also compute the grain size and density as a function of time. It should be noted that grain growth and densification processes are complex and that previously developed models have failed to provide a quantitative description of sintering[44,45]. We attempt to overcome this problem by using a fitting parameter to fit the quantitative predictions made by the model to our experimental data. The following sections discuss the details of the existing theoretical models and our analysis.

6.2.1 Rate of Grain Growth

A simplified model considers the change in grain size with time assuming grain boundary migration that is limited by surface diffusion-controlled pore drag from spherical pores[50]. The rate of grain growth is given by

$$\frac{dG}{dt} = \frac{F_b D_S \delta_S \Omega}{N_A \pi k T r^4} \qquad \text{Equation 16}$$

where,

F_b is the force per unit area of pore-free boundary, given by

$$F_b = \frac{\alpha \gamma_{gb}}{G} \qquad \text{Equation 17}$$

α is a geometrical constant[80], $\alpha \sim 2$

G is the grain size

N_a is the number of pores per boundary, given by[81] :

$$N_a = \frac{24}{\pi G^2} \qquad \text{Equation 18}$$

r is the radius of the pore given by[81]

$$r = r = G\left(\frac{1-\rho}{48}\right)^{1/3} \qquad \text{Equation 19}$$

$$\frac{dG}{dt} = \frac{F_b D_s \delta_s \Omega}{N_A \pi k T r^4} \qquad \text{Equation 16}$$

can thus be written as

$$\frac{dG}{dt} = \frac{K1}{(1-\rho)^{4/3} G^3} \qquad \text{Equation 20}$$

where

$$Kl = \frac{\alpha \gamma_{gb} D_s \delta_s \Omega (48)^{4/3}}{24 k T (1-\rho)^{4/3}} \qquad \text{Equation 21}$$

and ρ is the fractional density.

6.2.2 Rate of Densification

A geometrical model was used by Coble[50,] to describe the rate of densification by grain boundary diffusion. The model assumes each grain to be a tetrakaidecahedron, and that the pores are continuous and cylindrical. Coble derived a relationship for the rate of densification, $\frac{d\rho}{dt}$, given by

$$\frac{1}{\rho}\frac{d\rho}{dt} = \frac{4}{3}\left[\frac{D_{gb}\delta_{gb}\gamma_s\Omega}{\rho(1-\rho)^{1/2}G^4T}\right] \qquad \text{Equation 22}$$

An analogous model for grain boundary diffusion during the final stage of sintering has not been developed, but it is expected that the rate of densification would have a similar expression to Equation 22, except for a different pre-factor[50]. In our case, the films are annealed from the intermediate stage sintering all the way to the final stage, and a theoretical evaluation of a pre-factor is not feasible. We thus use the pre-factor (*Kpre*) as our fitting parameter.

Equation 22 can be written as

$$\frac{d\rho}{dt} = \frac{Kpre.4}{3}\left[\frac{D_{gb}\cdot\delta_{gb}\cdot\gamma_s\cdot\Omega}{(1-\rho)^{1/2}\cdot G^4\cdot k\cdot T}\right] \quad \text{or}$$

$$\frac{d\rho}{dt} = \left[\frac{Kpre\cdot K2}{G^4(1-\rho)^{1/2}}\right] \qquad \text{Equation 23}$$

where

$$K2 = \frac{4}{3}\left[\frac{D_{gb}\delta_{gb}\gamma_s\Omega}{k\cdot T}\right] \qquad \text{Equation 24}$$

6.2.3 Grain Growth – Density Trajectory

Using Equations 20, 21, 23 and 24, and using separation of variables we can write

$$\frac{d\rho}{(1-\rho)^{5/6}} = \frac{Kpre \cdot K2}{K1}\frac{dG}{G} \qquad \text{Equation 25}$$

Integrating both sides, we obtain

$$\mathbf{6}\left[(\mathbf{1}-\boldsymbol{\rho})^{\mathbf{1/6}} - (\mathbf{1}-\boldsymbol{\rho_o})^{\mathbf{1/6}}\right] = \frac{\boldsymbol{Kpre \cdot K2}}{\boldsymbol{K1}}\boldsymbol{ln}\left(\frac{\boldsymbol{G}}{\boldsymbol{G_o}}\right) \qquad \text{Equation 26}$$

where ρ_o, is the initial fractional density

and G_o is the initial grain size

Equation 26 gives the grain size – density trajectory. Since we know the values of density and grain size after annealing for 300 sec at different temperatures, it is possible to determine the ratio $\frac{Kpre \cdot K2}{K1}$ at different temperatures. This ratio alone determines the grain size - density trajectory.

While the ratio determines the grain size-density trajectory, the actual values of density and grain size can be evaluated only if we know the values of (*Kpre·K2*) and *K1*. The values of *K2* can be calculated from the known constants and using the grain boundary diffusivity data from Guy[33]. The values of D_{gb} extrapolated from this data are tabulated in Table 3.

Table 3: D_{gb} values obtained from extrapolations of Guy [33]

Temperature (°C)	D_{gb} (m^2/s)
125	1.15×10^{-17}
150	6.22×10^{-17}
200	1.05×10^{-15}
250	1.04×10^{-14}

From Figure 31, we have shown that almost complete densification occurs within a few seconds at an annealing temperature of 150 °C. We thus expect complete densification to also occur within 300 seconds for temperatures higher than 150 °C (200 and 250 °C). We have measured the density of films after rapid thermal annealing at temperatures of 150, 200 and 250 °C after 300 seconds of annealing. Using this boundary condition and the known ratio $\frac{Kpre \cdot K2}{K1}$ we can iteratively find the value of the pre-factor *Kpre*.

Using this analysis we determine the value of *Kpre* to be 36.5 ± 4.9. The procedure for calculating the error in *Kpre* is presented in Appendix A. With the known value of *Kpre* and *K2*, and the ratio $\frac{Kpre \cdot K2}{K1}$, we can determine *K1*. It is important to note here that it is quite possible that a pre-factor was associated with Equation 16 also. However, since *K1* is determined from the ratio $\frac{Kpre \cdot K2}{K1}$, any pre-factor associated with

Equation 16 is incorporated into *K1*. It is precisely for this reason why we need only one fitting parameter in this work. The procedure for calculating the error in *K1* is given in Appendix A.

With the known values of *K1* at different temperatures, it is now possible to calculate the values of D_s at these temperatures. Figure 37 shows a plot of $log(D_s)$ vs *1000/T*. The linear fit can be used to calculate the activation energy (E_a) of surface diffusion at low temperatures and pre-exponential factor D_o:

$$D_s = D_o e^{-\frac{Ea}{k \cdot T}} \qquad \text{Equation 27}$$

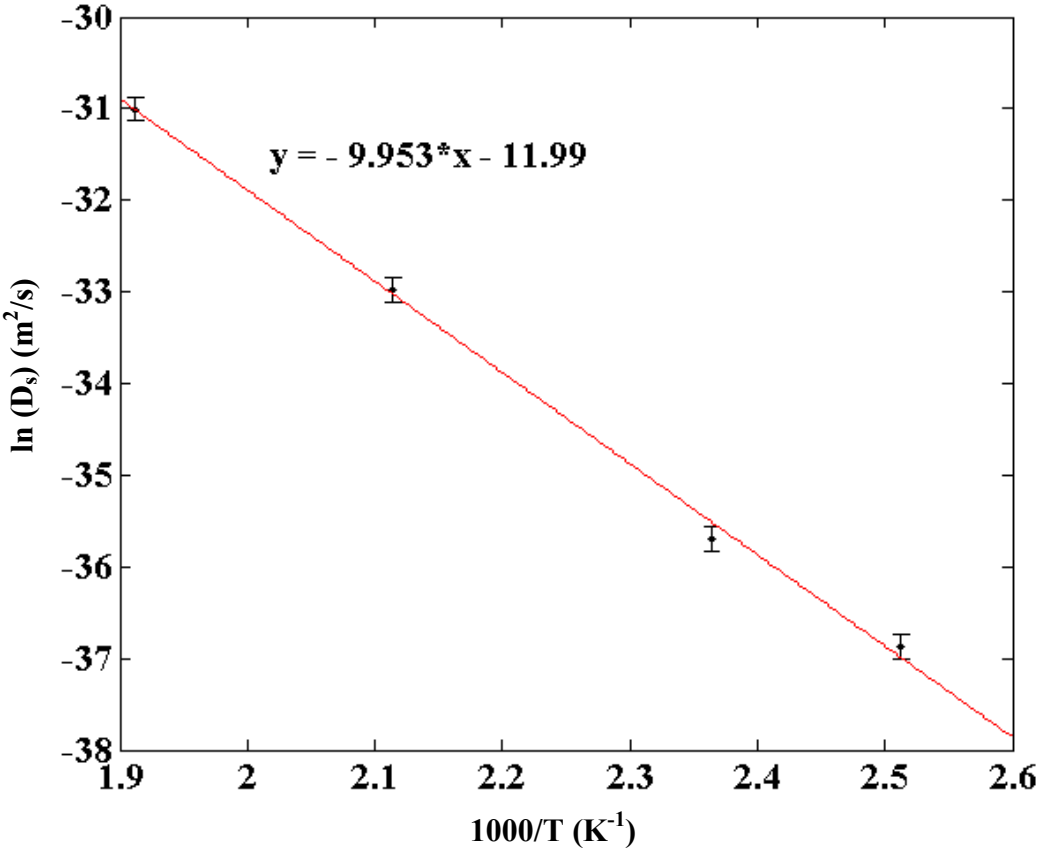

Figure 37: *ln(D_s)* vs 1000/*T* plotted for estimated values of D_s.

The value of E_a is found to be 0.77 ± 0.03 eV and the value of D_o is found to be $1.02 \cdot 10^{-6} \pm 0.2 \cdot 10^{-6}$ m^2/s and the values of D_s at different temperatures can be obtained using $D_s = D_o e^{-\frac{Ea}{k \cdot T}}$ Equation 27.

We have thus used our experimental data to determine the effective surface diffusivities at low temperatures (100-250 °C). It should be noted that we have assumed here that Equation 16 is correct and that it can describe grain growth in real systems. It is, however, quite likely that a pre-factor is associated with Equation 16 in the same way as it was for Equation 22. If that is the case, the pre-factor is automatically incorporated in D_o during our analysis. Since the pre-factor is incorporated in D_o, the accuracy of the value of D_o does not have any effect on the calculated values of *K1*. Table 4 lists the calculated values of D_s at low temperatures. The errors listed for the values of Ds are a minimum bound on the errors, and the actual error comes from the pre-factor associated with Equation 16. Figure 38 shows the calculated values of $log(D_s)$ plotted versus 1000/T along with the existing data from Guy[33].

Table 4: Values of D_s determined in this work at temperatures of interest

Temperature (°C)	D_s (m^2/sec)
100	$3 \times 10^{-17} \pm 1.3 \times 10^{-17}$
125	$1.6 \times 10^{-16} \pm 1.1 \times 10^{-17}$
150	$6 \times 10^{-16} \pm 4.3 \times 10^{-17}$

200	$5.71\times10^{-15} \pm 6.52 \times10^{-16}$
250	$3.5\times10^{-14} \pm 4.7\times10^{-15}$

Table 4 (continued): Values of D_s determined in this work at temperatures of interest

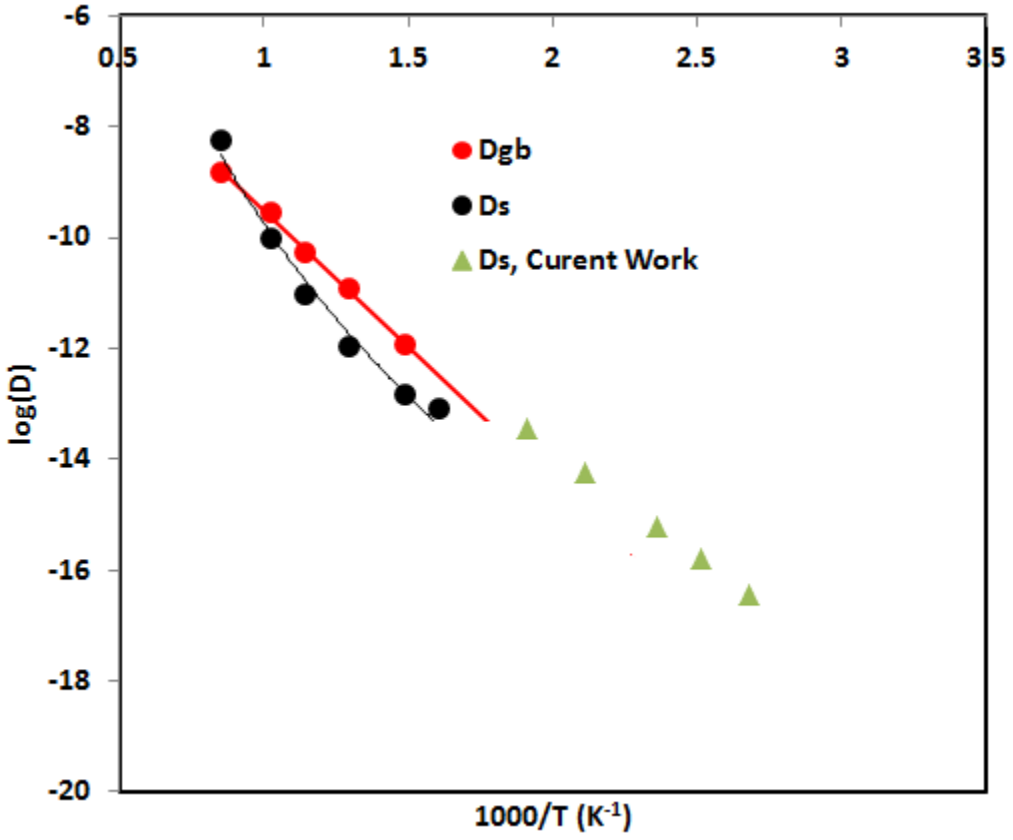

Figure 38: D_s obtained in this work (green). Also plotted are D_s and D_{gb} (black and red, respectively) from Guy[33]

6.3 Dependence of Conductivity on Annealing Treatment

Section 6.2 established the dependence of conductivity on grain size and density, while Section 6.3 demonstrated a method to calculate the effect of annealing temperature and time on the evolution of density and grain size. In this section, we combine these analyses and use Equations 13-27 to model the effect of annealing treatment on the conductivity of nanoparticulate silver thick films. A computer code was written using MATLAB®[82] to solve these equations numerically and thus study the effects of annealing treatment on the final density, grain size, conductivity, and grain-size density trajectory. The code is presented in Appendix A. The input parameters for the model are the initial NP size, initial relative film density, annealing temperature, type of annealing treatment (single step or multi-step) and annealing time. Using the model, it is thus also possible to individually evaluate the effects of initial NP size and initial relative film density on the final sintered density and conductivity of films, which is not possible using our present experimental setup.

6.4 Results of the model

6.4.1 Effect of Rapid Thermal Annealing

The effects of annealing temperature on grain-size, density, conductivity, and grain size-density trajectory is evaluated using the model. For this study, the annealing

time is fixed at 5 min, the initial NP size is taken to be 6 nm, and initial fractional density is taken as 0.7, which is the same as the initial conditions for the as-deposited films discussed that were evaluated experimentally for this work (Chapter 5). The results of the modeling for temperatures ranging from 100 – 250 °C are presented here.

a) 100 °C: Figure 39 shows the predictions of the model for annealing at 100 °C for 5 min.

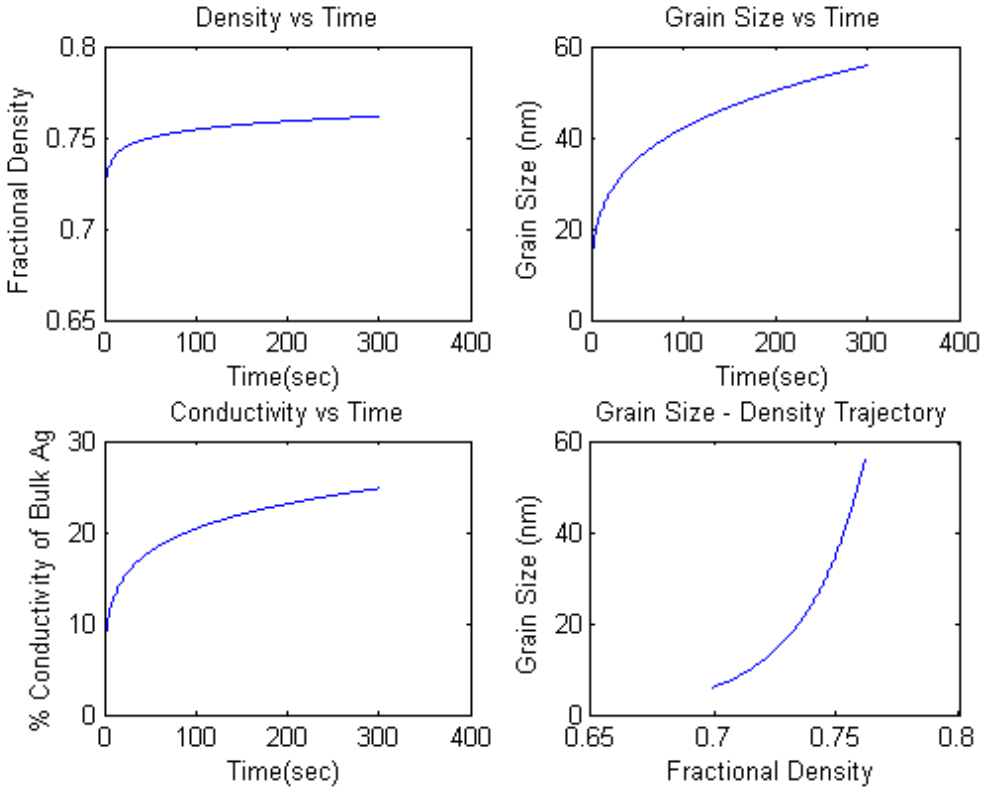

Figure 39: Predictions of the model for films annealed at 100 °C for 5 min.

b) 125 °C: Figure 40 shows the predictions of the model for annealing at 125 °C for 5 min.

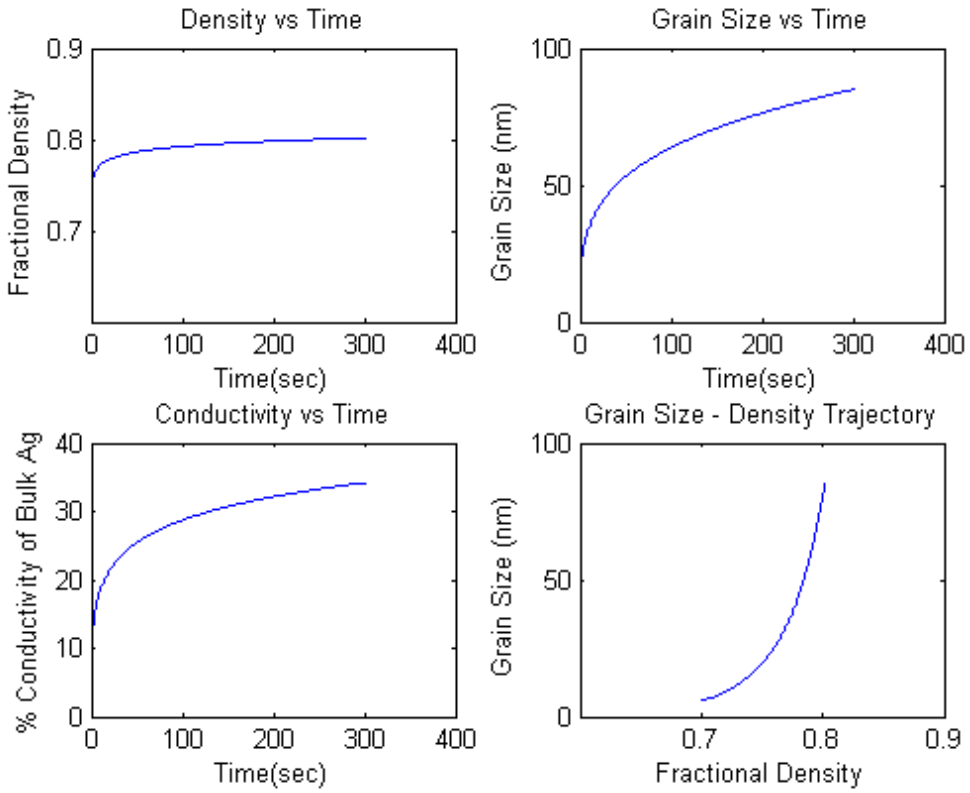

Figure 40: Predictions of the model for films annealed at 100 °C for 5 min.

c) 150 °C: Figure 41 shows the predictions of the model for annealing at 150 °C for 5 min.

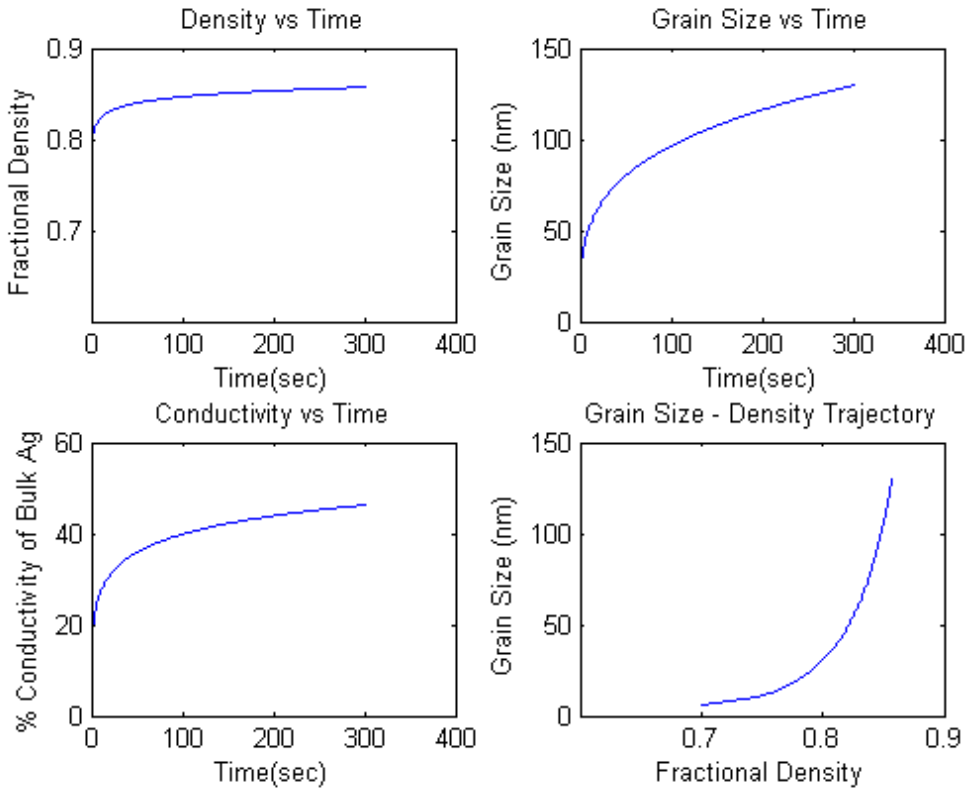

Figure 41: Predictions of the model for films annealed at 150 °C for 5 min.

d) 200 °C: Figure 42 shows the predictions of the model for annealing at 200 °C for 5 min.

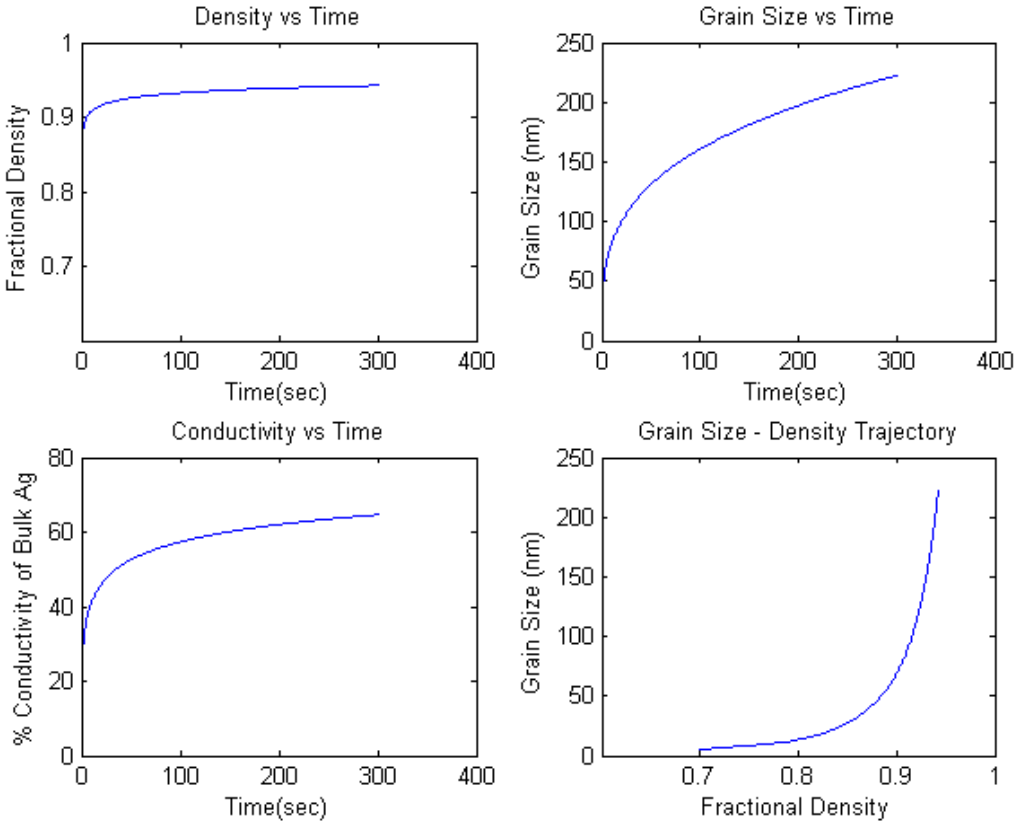

Figure 42: Predictions of the model for films annealed at 200 °C for 5 min.

e) 250 °C: Figure 43 shows the predictions of the model for at 250 °C for 5 min.

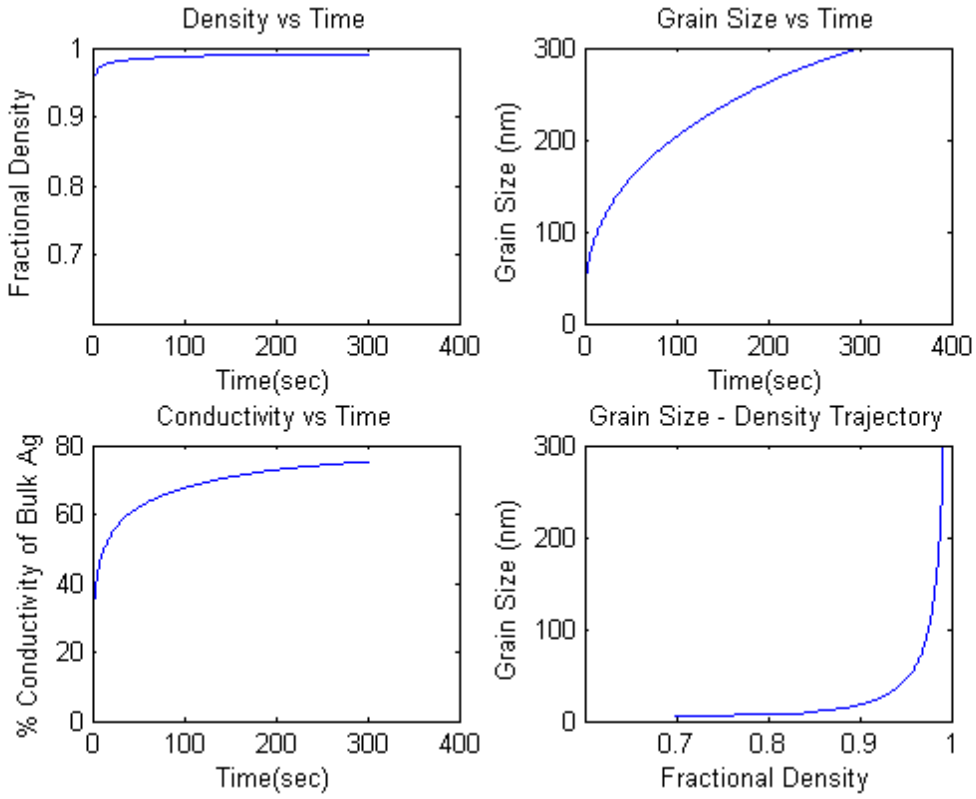

Figure 43: Predictions of the model for films annealed at 250 °C for 5 min.

6.4.1.1 Comparison with Experimental Data

Comparisons between the experimentally measured values of conductivity, density and grain size and those predicted from the model are shown in Figure 44. The results for densities and conductivities from the model fit very well with the experimentally measured values. There are, however, some minor discrepancies between

the predicted values of grain size and the experimentally measured values. It should be noted that conductivities at high relative densities are a stronger function of density than grain size. Thus, these discrepancies do not significantly affect the predicted conductivities.

a)

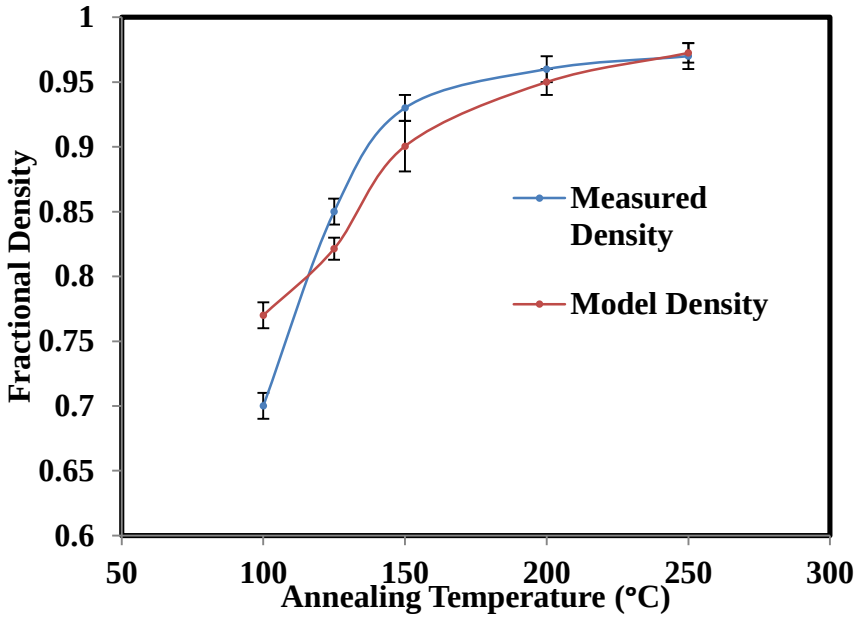

b)

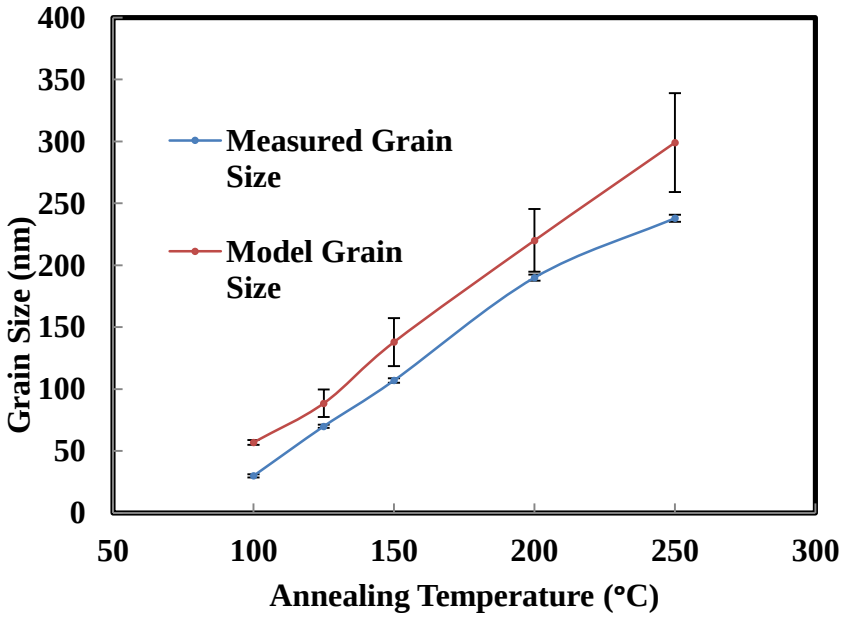

Figure 44: Comparison between the predicted and experimentally measured values of a) density, b) grain-size, and c) conductivity

c)

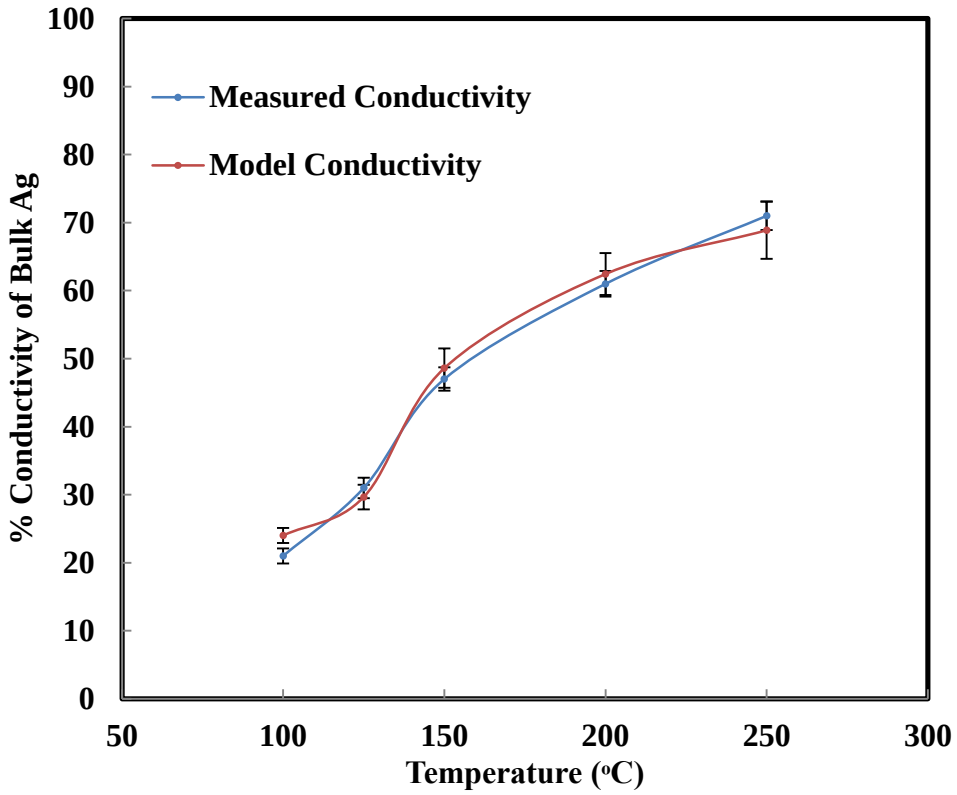

Figure 44: Comparison between the predicted and experimentally measured values of a) density, b) grain-size, and c) conductivity

6.4.2 Effect of Two-step Annealing Treatment

The effect of a two-step annealing treatment can also be evaluated using the model. To demonstrate, we modeled a two-step annealing treatment with the first annealing treatment at 100 °C for 5 min and the second annealing treatment at 150 °C for 5 min. The initial NP size is taken to be 6 nm and initial fractional density is taken as 0.7. Figure 45 shows the results of the predictions from the model. The annealing treatment

and initial conditions for the model were compared with the experimental results reported in Section 5.5 and the predictions match very well with the experimentally obtained values of density (experimentally measured value 0.8 compared to 0.81 calculated by the model) and conductivity (experimentally measured value of 37% compared to 40% of bulk conductivity calculated by the model).

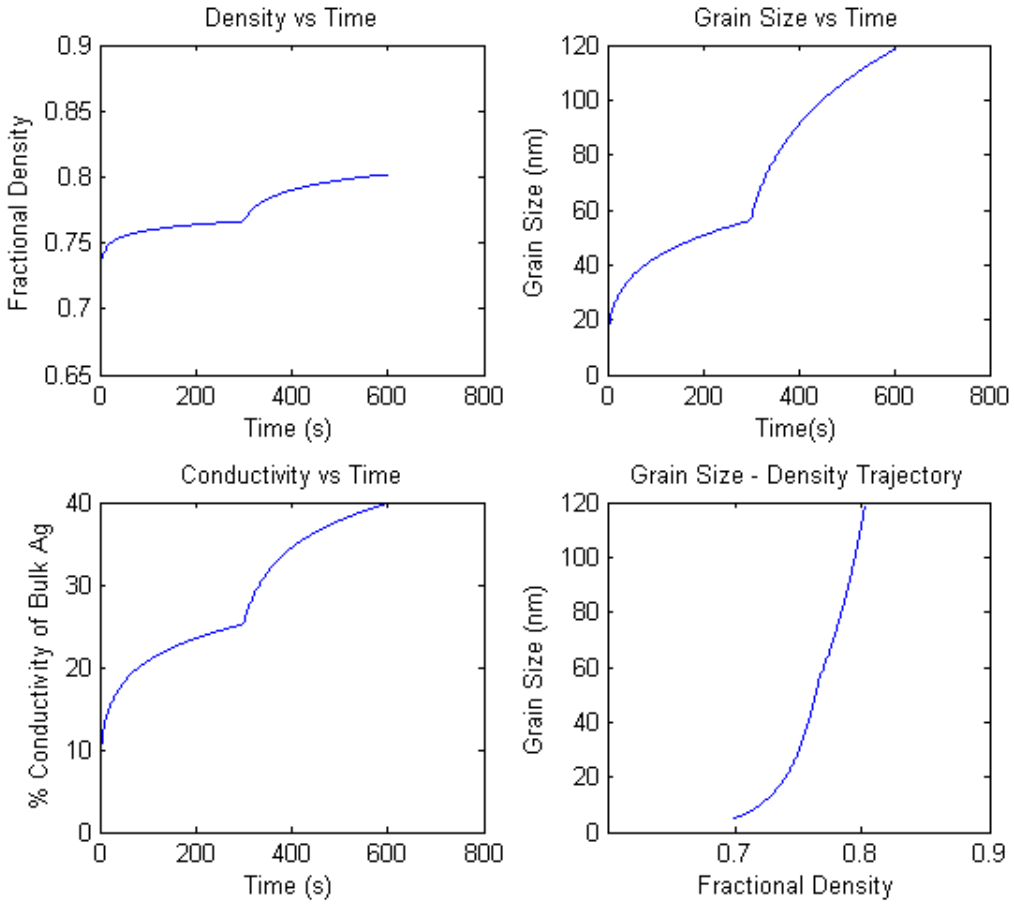

Figure 45: Predictions of the model for a two-step annealing treatment.

6.4.3 Influence of NP size

The model allows us to evaluate the effect of particle size on the evolution of density, grain size and conductivity, something which is not possible to evaluate experimentally using the present experimental setup. We assume an initial particle size of 60 nm while keeping the initial fractional density as 0.7, to predict the effect of particle size on the density, grain size, conductivity and grain size - density trajectory at 150 ^{o}C. The predictions of the model are shown in Figure 46. This plot shows that when the initial particle size is increased from 6 nm to 60 nm, the final density, grain size and conductivity after a 5 min annealing treatment at 150 ^{o}C are predicted to be significantly lower, which is expected in accordance with the Herrings law.

a)

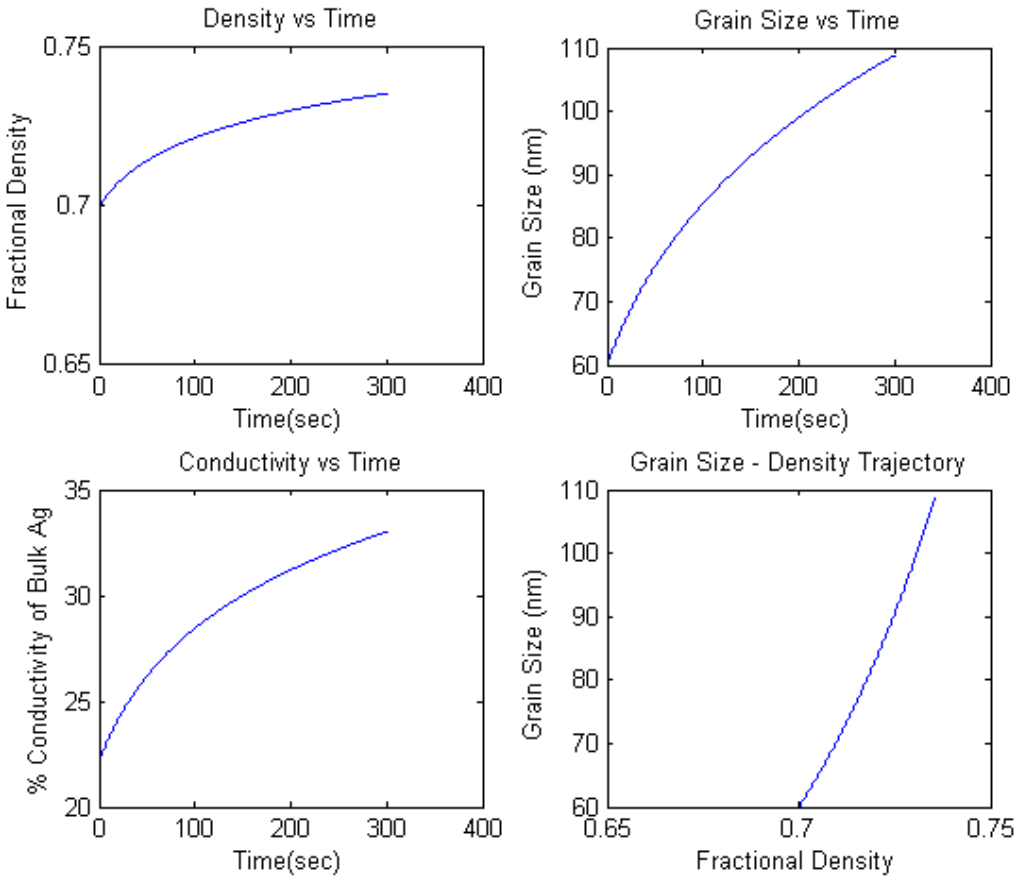

Figure 46: Predictions of the model for annealing at 150 °C with an initial fractional density of 0.7 and particle size a) 60 nm and b) 6 nm, 30 nm and 60 nm.

b)

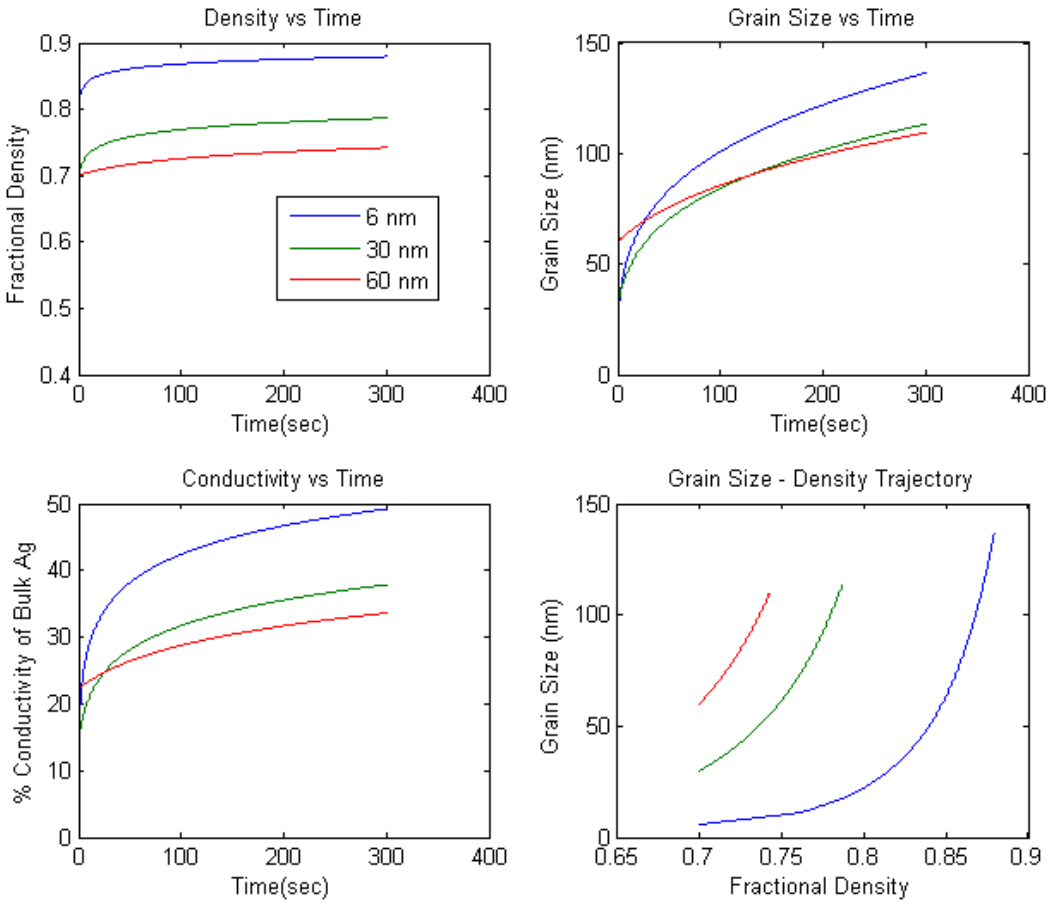

Figure 46: Predictions of the model for annealing at 150 °C with an initial fractional density of 0.7 and particle size a) 60 nm and b) 6 nm, 30 nm and 60 nm.

6.4.5 Effect of Initial Density

The model also allows us to predict the effects of initial density on the evolution of density, grain size and conductivity, which is not possible to evaluate experimentally using the present experimental setup. To demonstrate, predictions were made assuming an initial fractional density of 0.5 and 0.6 to compare with the previous predictions that assumed a relative density of 0.7. The predictions of the model are shown in Figure 47. The results show that when the initial density decreases the final density, grain size and conductivity decreases. As the initial fractional density is lowered to 0.5, the final densities and conductivity are significantly lower when compared to case where the fractional density was 0.7. After a 300 sec rapid thermal annealing treatment at 150 ^{o}C, the results of the model show that for initial densities of 0.6 and 0.5, the final densities were found to be respectively lower by 10.22% and 17.61%, than the case where initial fractional density was 0.7. Similarly the final conductivities were found to be lower by 16.3% and 30.4% for initial densities of 0.6 and 0.5 respectively, when compared to the case where the initial fractional density was 0.7.

a)

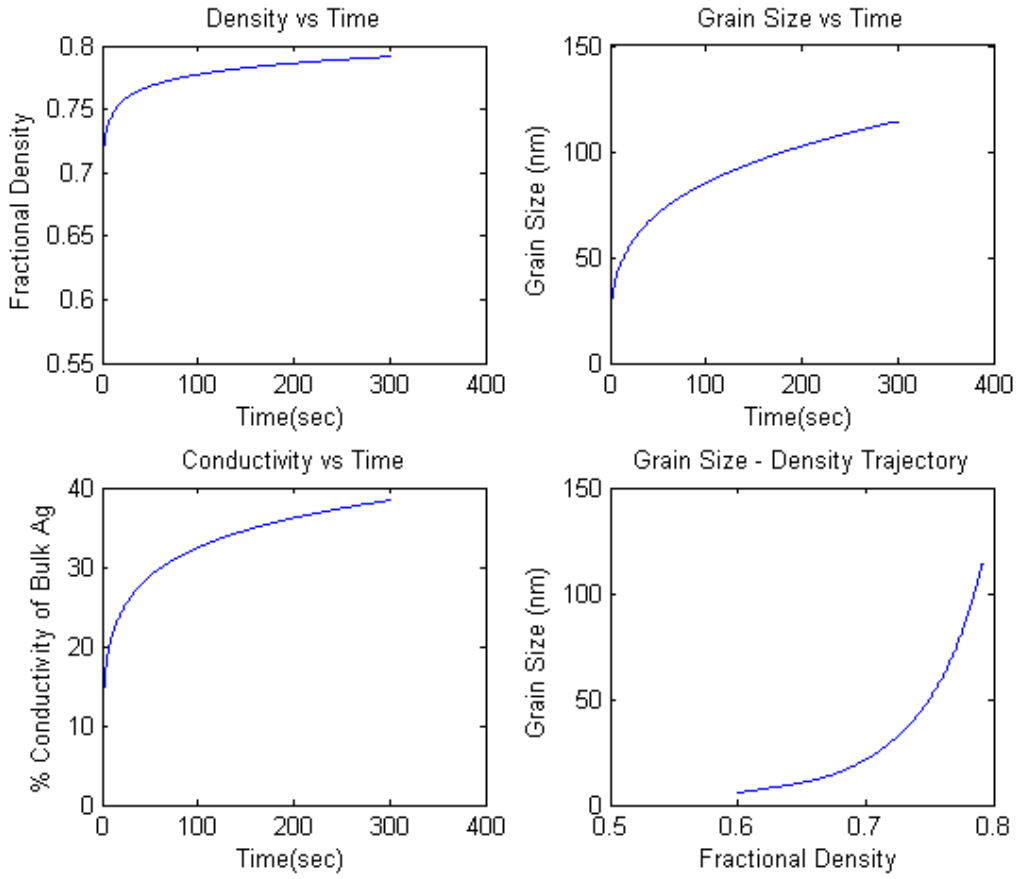

Figure 47: Predictions of the model for annealing at 150 °C with initial particle size of 6 nm and an initial fractional density of a) 0.6, and b) 0.5., c) 0.5, 0.6, and 0.7

b)

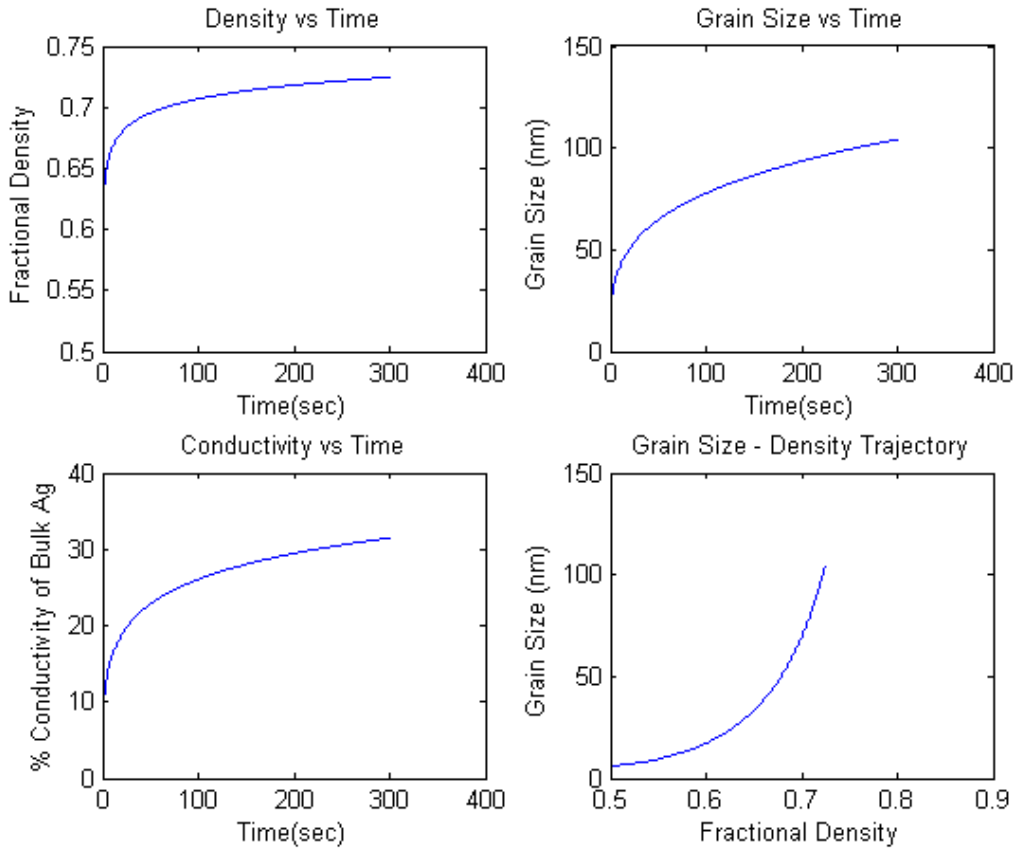

Figure 47: Predictions of the model for annealing at 150 °C with initial particle size of 6 nm and an initial fractional density of a) 0.6, and b) 0.5., c) 0.5, 0.6, and 0.7

c)

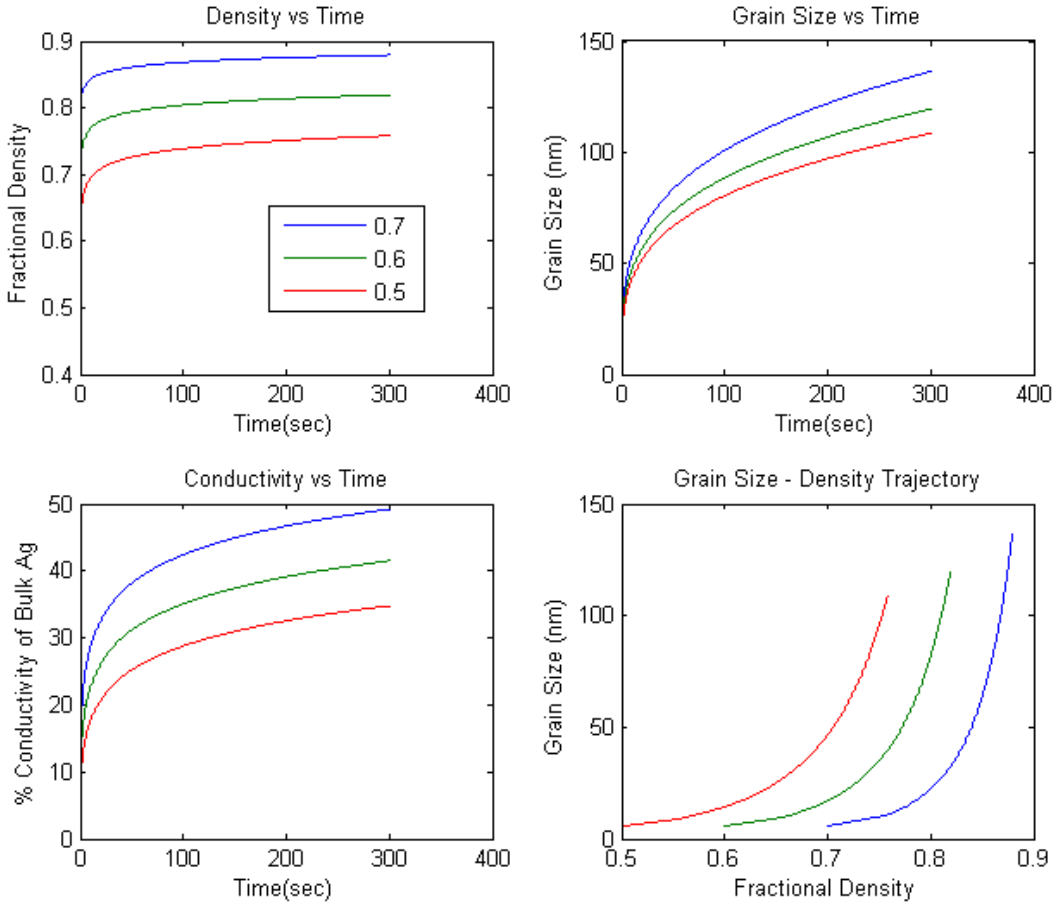

Figure 47: Predictions of the model for annealing at 150 °C with initial particle size of 6 nm and an initial fractional density of a) 0.6, and b) 0.5., c) 0.5, 0.6, and 0.7

6.5 CONCLUSIONS

We have presented a model that describes the evolution of the microstructures and conductivities of thick nanoparticulate silver films at low annealing temperatures as a

function of time. The model is derived based on existing theoretical models of the dependence of conductivity on density and grain size[29,30], a theoretical analysis of simultaneous densificaion and grain growth in the intermediate and final stages of sintering[48,50] and by fitting experimental data to the models. The use of a fitting parameter to the theoretical models is necessary since the theoretical models assume highly idealized geometries for the particle and pore geometries and thus fail to quantitatively predict the sintering behavior in real systems[44,45]. The uniqueness of the current model lies in the fact that it predicts the sintering behavior and the dependence of conductivity on the annealing treatment for a real system with reasonable accuracy. The effect of the type of annealing treatment, influence of NP size and influence of initial relative density on the final microstructures and conductivities of the sintered films are calculated using the model. We also were able to determine the effective surface diffusivity and activation energy for surface diffusion at low temperatures for silver, which is difficult to measure directly using other techniques. These results compare reasonably well with measured values of surface diffusivity and activation energy for surface diffusion that were determined at high higher temperatures and extrapolated to lower temperatures. The ability of this model to accurately predict sintering behaviors shows its utility in the development of low temperature annealing treatments to produce high conductivity, nanoparticulate films.

Chapter 7: Effect of Agglomeration

The attractive van der Waals forces between particles increases as the distance between particles decreases and so NPs have a very strong tendency to agglomerate[83]. Furthermore, as demonstrated earlier, when bare NPs touch, they can sinter at room temperature and form "hard" agglomerates which cannot be subsequently broken[84]. A negative consequence of particle agglomeration is a decrease in the packing density[85] which results in a lower sintered density on further annealing[86]. Also, agglomerates often pack non-uniformly, leaving high porosity regions surrounded by more dense regions[85]. These non-uniformites can give rise to differential densification and lead to porosity and cracks in the sintered product[87,88].

Aerosol-based methods for producing thick films, in particular, suffer from a lack of control of agglomeration because organic dispersants that can be effective at preventing agglomeration in suspension-based processes are not typically used in aerosol processes[89,90]. As a result, the films produced by aerosol methods are generally annealed at high temperatures to achieve adequate conductivity. Unfortunately, systematic experimental studies of the effect of agglomeration on conductivity of NPs that would be useful in addressing this issue do not exist. Gleason[26] studied the agglomeration dynamics on NPs and offered a way to quantitatively control agglomeration of NPs produce by the LAMA process which is utilized in this work to produce conductive lines with controlled agglomeration. While, characterizing the state of agglomeration is still a

difficult task, the density of the agglomerated compacts is a useful if indirect measure of the extent of agglomeration because films that contain high fractions of agglomerates have a low relative density. In this chapter we present an experimental investigation of the effects of agglomeration on the final microstructures, densities and conductivities of as-deposited and sintered nanoparticulate films. Films deposited at feed rates of 10 mg/hr, 20 mg/hr and 50 mg/hr were used for this study.

7.1 MICROSTRUCTURE

The plan-view microstructure of lines annealed at 150 ^{o}C for 5 min are shown in Figure 48. The levels of porosity in the annealed lines appear to increase with increasing MP feed rate, and the grain size appears to decrease. The grain sizes were quantified by image analysis and the results are shown in Figure 49, showing the effects of agglomeration on the grain size of lines annealed at 150 ^{o}C.

a)

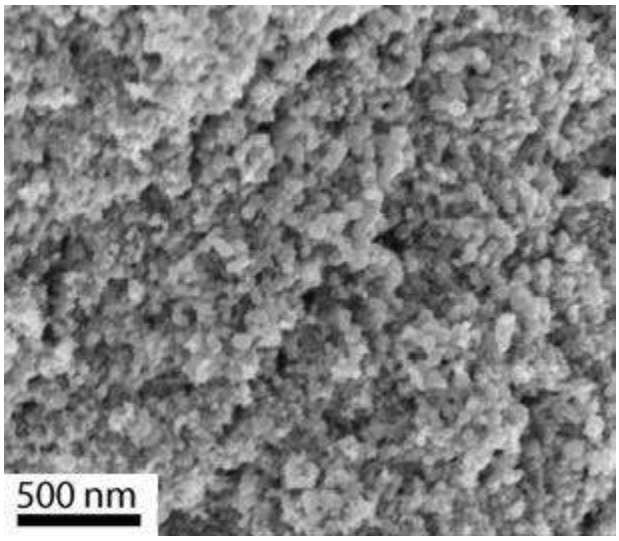

b)

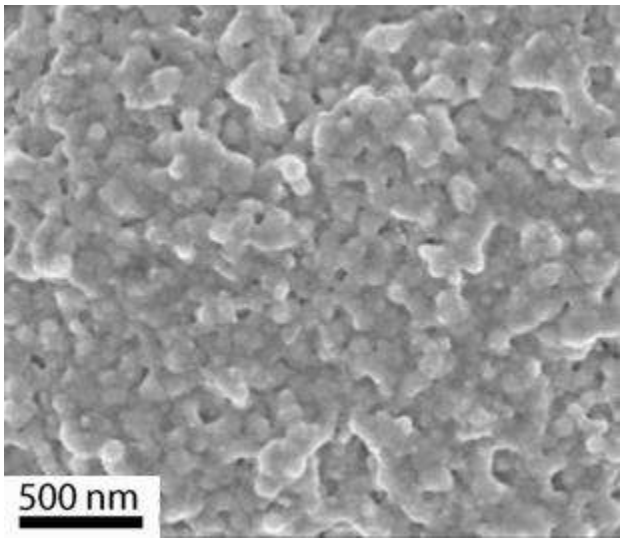

Figure 48: Plan-view microstructures of lines annealed at 150 °C. MP feed rates of a) 50 mg/hr, b) 20 mg/hr, c) 10 mg/hr

c)

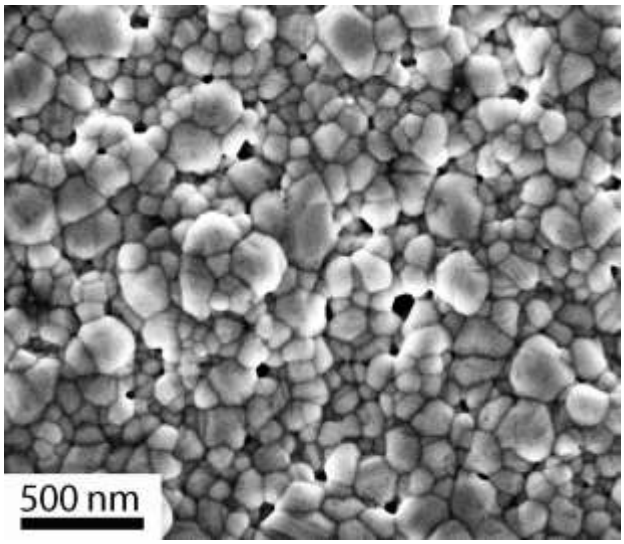

Figure 48: Plan-view microstructures of lines annealed at 150 °C. MP feed rates of a) 50 mg/hr, b) 20 mg/hr, c) 10 mg/hr

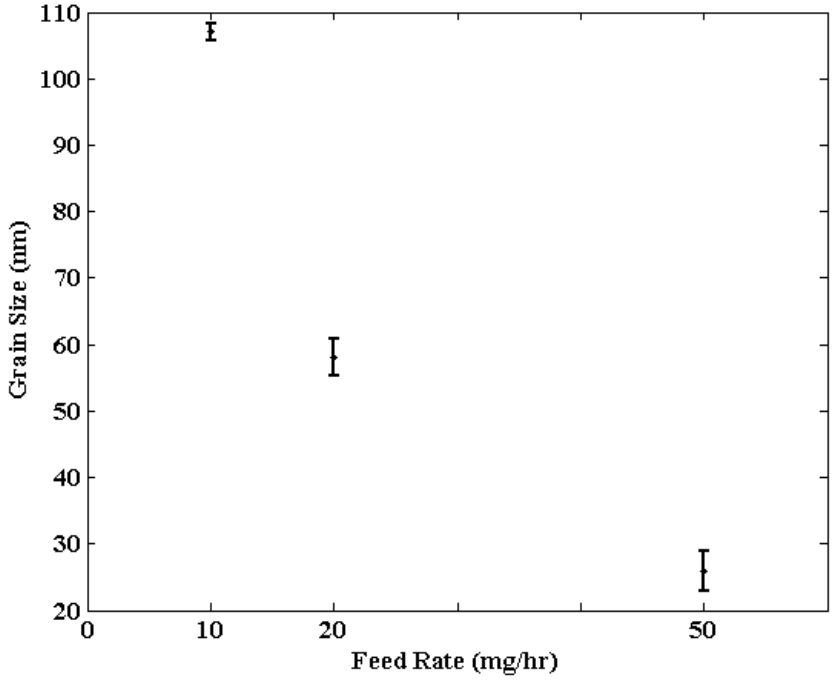

Figure 49: Grain size versus feed rate for films annealed at 150 °C

7.2 DENSITY

The densities of the lines were measured using the technique described in Chapter 3 and are presented as function of the MP feed rate in Figure 50 for both as-deposited and annealed lines.

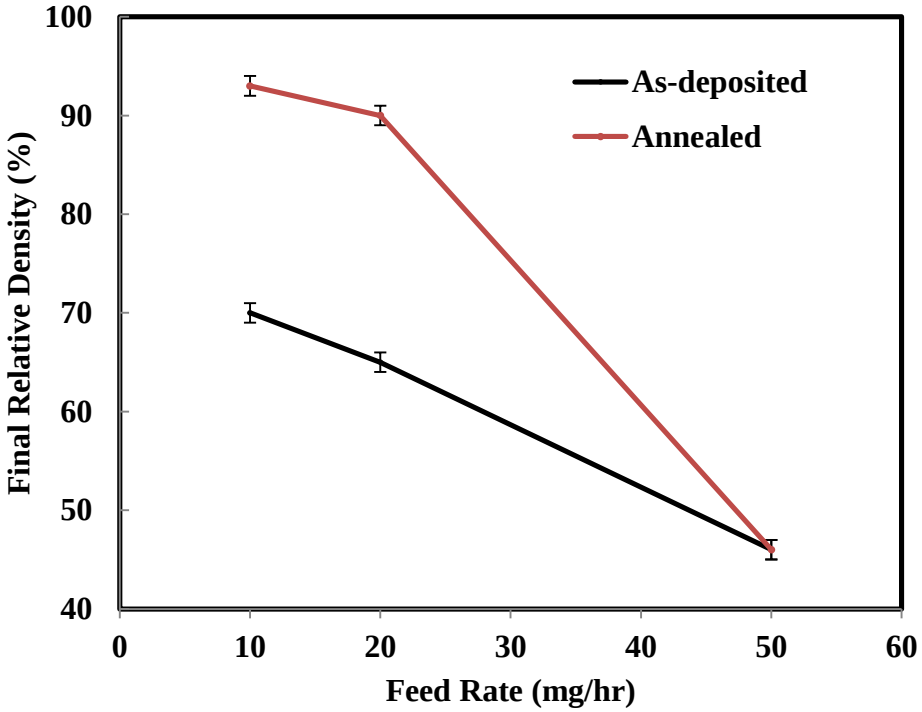

Figure 50: Dependences of the densities of as-deposited and annealed films on MP feed rates

The densities of the as-deposited lines decrease with feed rate because the packing efficiency decreases with the increase in the state of agglomeration. The density of the annealed lines decreases from 93% to 90% when the feed rate is increased from 10 to 20 mg/hr. The highly agglomerated films that were produced at an MP feed rate of 50 mg/hours do not show any measurable densification because of the very low initial densities of these films.

7.3 CONDUCTIVITY

Figure 51 shows the influence of feed rate on conductivities of the as-deposited and annealed lines. The lines exhibit a marked decrease in conductivity with increases in the MP feed rate. The conductivities obtained in this work suggest that highly agglomerated lines are the cause of the relatively low values of conductivities observed in previous lines produced by LAMA and reported by Albert *et al.*[24] and Huang *et al*[25].

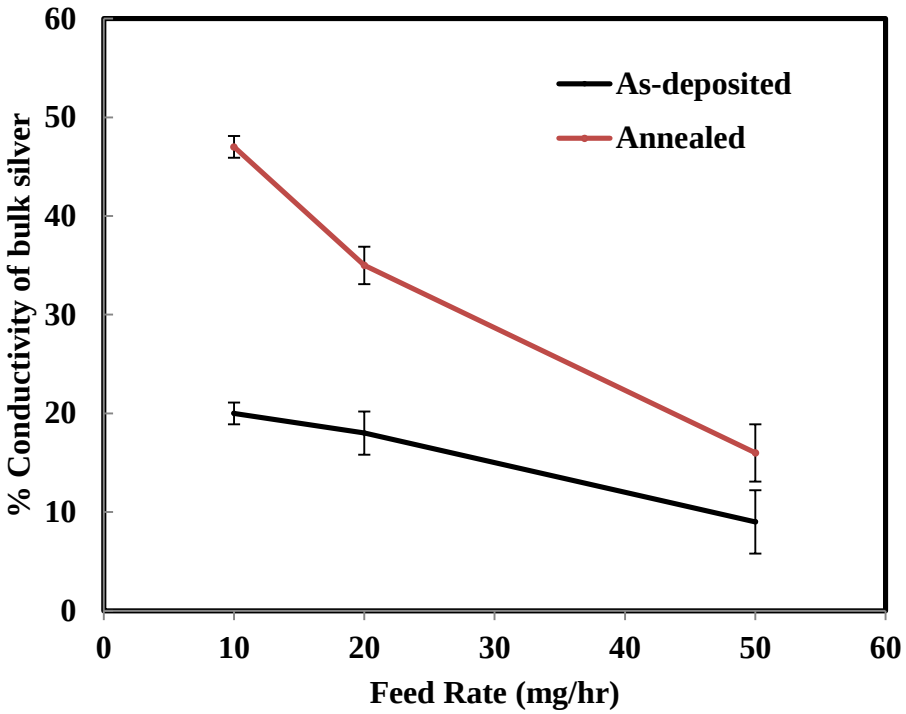

Figure 51: Dependences of feed rate on the conductivities of as-deposited and annealed films

7.4 CONCLUSIONS

Agglomeration was shown to have a significant effect on the properties, sintering behavior, and conductivity of the annealed lines. In the LAMA process, the MP feed rate controls the degree of agglomeration in the lines. We have presented an experimental study of the effects of MP feed rate on the density, grain size and conductivity of as-deposited and annealed films. The results of the study can be summarized as follows:

1. As the MP feed rate increases, the initial relative density and conductivity of the as-deposited lines decreases.
2. As the MP feed rate increases, the final density, grain size and conductivity of the annealed lines decreases.
3. An increase in the MP feed rate from 10 to 20 mg/hr significantly decreases the sinterability of the films. A further increase of the MP feed rate to 50 mg/hr produces films that show no measurable densification or increase in conductivity on annealing at a temperature of 150 ^{o}C.

From our experimental results we conclude that a maximum MP feed rate of 10 mg/hr should be used to produce films using the LAMA process, if high conductivity at low processing temperatures is desired.

Chapter 8: Comparative studies with low initial density films consisting of larger NPs

The films discussed in Chapters 4-6 consist of small NPs packed to high initial densities. A comparative study with larger NP films and low initial density films would elucidate the importance of particle size and packing efficiency in films. While it is not possible with the given setup to change the particle size and packing density in films independently, it is possible to produce larger NPs in the LAMA process by substituting Ar for He as the carrier gas which also results in lower particle impaction speeds and thus relatively porous films. A comparative study with such films is significant in qualitatively accessing the overall influence of NP size and initial density on the properties of the final sintered films, and the effects of deposition conditions of the LAMA process. In this chapter we present a comparison of the properties of the sintered films made in He and Ar gas.

8.2 Influence of Temperature

Nanoparticulate films were produced in He and Ar by maintaining a feed rate of 10 mg/hr, and were rapid thermally annealed at temperatures of 150, 200 and 250 ^{o}C for 5 minutes. The relative densities of the as-deposited films made in He and Ar were 70% and 42% respectively.

8.2.1 Microstructure

The plan-view microstructures of the as-deposited and sintered lines deposited with Ar as the carrier gas are shown in Figure 52. A comparison of the mean grain sizes of films produced in Ar and He are shown in Figure 53.

a)

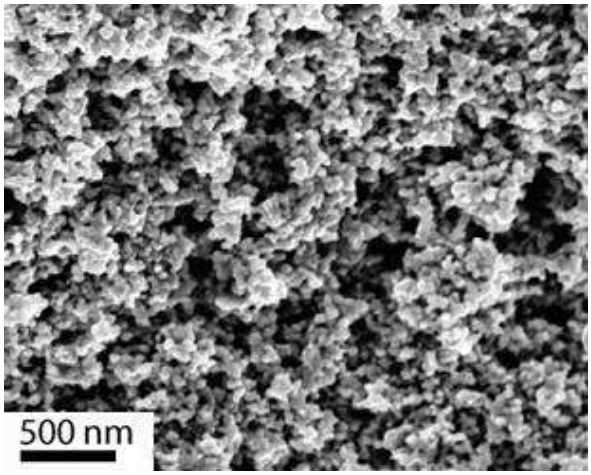

b)

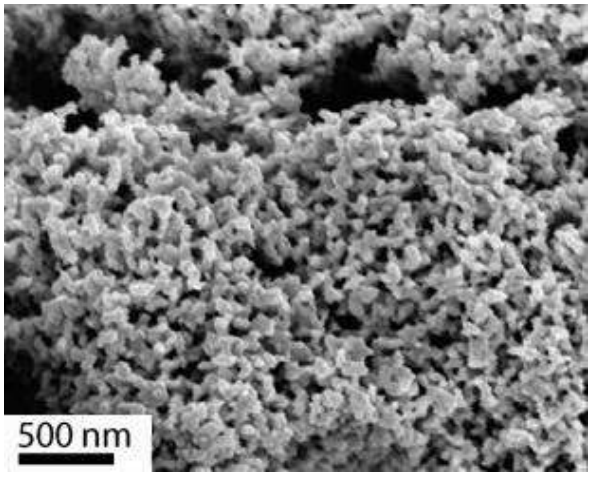

Figure 52: Plan-view microstructures of lines deposited in Ar as the carrier gas a) as-deposited, and annealed at b) 150 °C, c) 200 °C, d) 250 °C

c)

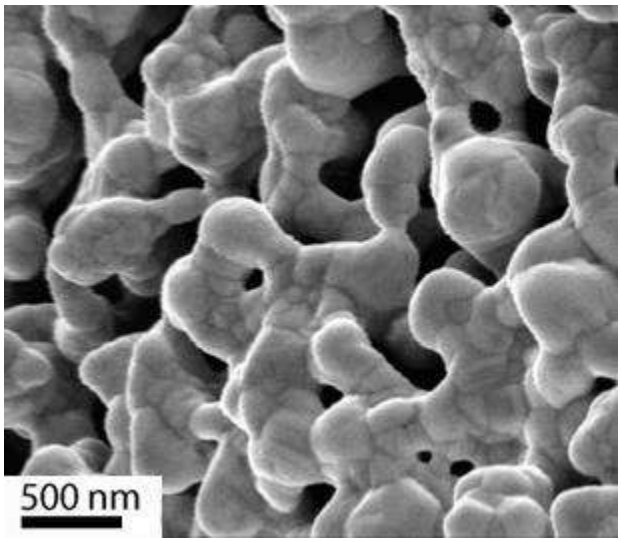

d)

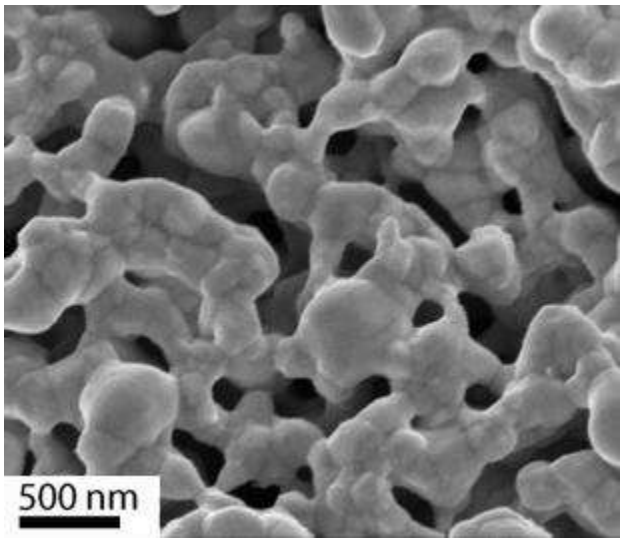

Figure 52: Plan-view microstructures of lines deposited in Ar as the carrier gas a) as-deposited, and annealed at b) 150 °C, c) 200 °C, d) 250 °C

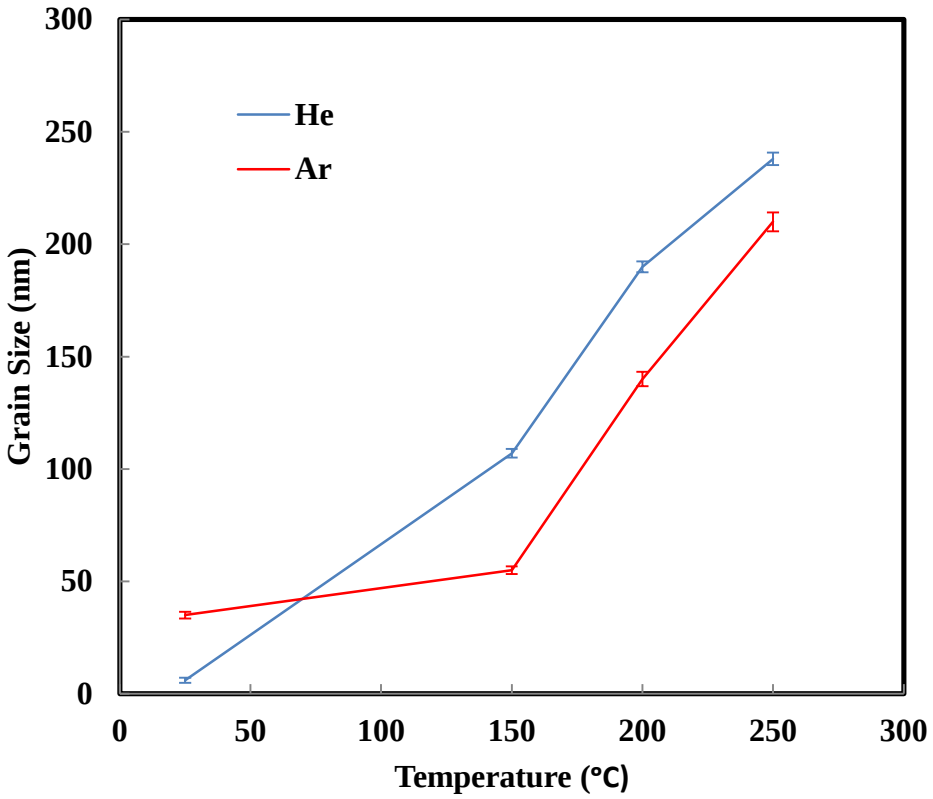

Figure 53: Comparison of grain sizes of sintered films produced using He and Ar carrier gas

It can be seen from Figure 53 that the grain sizes of the as-deposited lines produced using Ar are significantly larger than the those produced using He. However, the grain sizes of the annealed films produced with He are larger than those produced in Ar and annealed under the same conditions. We can explain these results by considering that the rate of grain growth is dependent on the grain size and density (Equation 20), and it increases with increasing density and decreasing grain size. Upon annealing, the lines deposited in He densify very quickly to near full densities, which increases the rate of grain growth (Equation 20). The films deposited in Ar on the other hand do not densify

significantly, and the rate of grain growth is always lower than the rate of grain growth in films deposited in He. The grain size of films deposited in He is therefore larger than the grain size of films deposited in Ar.

While we do not observe any measurable densification in films deposited in Ar, the films likely densify but my an amount that is below the detection limits for this technique. As the annealing temperature increases, densification for lines deposited in both Ar and He increase. However, since the films deposited in He have already densified to near full densities at 150 °C, the increase in density at temperatures higher than 150 °C is negligible. The difference in the density of films deposited in Ar at different temperatures is, however, significant. Thus, the rate of grain growth increases much more with temperature for lines deposited in Ar when compared to lines deposited in He. The differences in the grain sizes of Ar-deposited and He-deposited lines thus decrease as the annealing temperature increases.

8.2.2 Density

The annealed lines deposited in Ar exhibited no measurable change in density for annealing temperatures up to 250 °C. The relatively low sintered density of lines deposited in Ar can be attributed to the larger sized NPs from which the lines were produced and the low initial relative density of the lines. While the larger size of the NPs produced in Ar decreases the sintering kinetics when compared to smaller NPs produced in He, the low initial density also decreases the driving force for densification (Equation 23).

8.2.3 Conductivity

A comparison of the conductivities of the as-deposited and annealed lines deposited in He and Ar are shown in Figure 54. The conductivities of lines deposited in Ar are found to be substantially lower than the ones deposited in He.

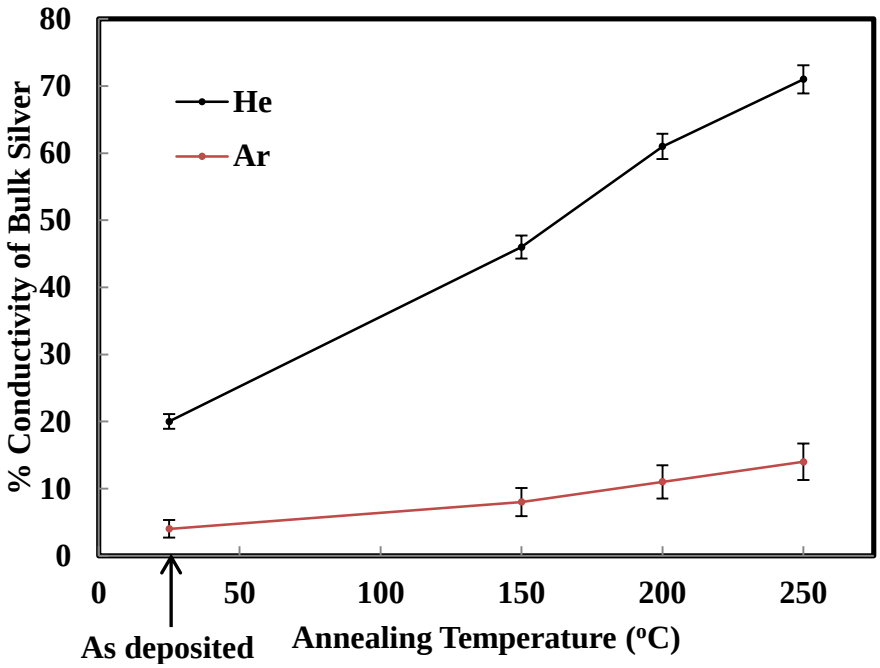

Figure 54: Comparison of conductivities of lines deposited in He and Ar.

8.3 CONCLUSIONS

Table 5: summarizes the major differences observed between films deposited in He and Ar gas using the direct write LAMA process.

Table 5: Comparison of Properties of films deposited in He and Ar carrier gas using the direct write LAMA process.

Property	He	Ar
Line width	Smaller FWHM	Larger FWHM
NP size	5-10 nm	30-40 nm
Initial density	70% relative density	42% relative density
Sintered density	~ 93-97% at annealing temperatures up to 250 ^{o}C	No measurable change in density on annealing
Microstructure	Larger grain size in annealed films. Low porosity in as-deposited and annealed films.	Smaller grain size in annealed films. High porosity in as-deposited and annealed films
Conductivity	High conductivity in as-deposited film which increased to very high values on annealing at low temperatures (150-250 ^{o}C)	Low conductivity and only marginal improvement in conductivity on annealing

Chapter 9: Conclusions

In this work the direct-write LAMA process has been used to deposit highly conductive thick lines/films of silver NPs. The conventional LAMA setup was used with a modified aerosol feeding mechanism[26], which gives control over the agglomeration characteristics of the NPs. While the conventional LAMA setup has the capability of producing organic dispersant-free, small NPs which are uniform in size, the use of the modified aerosol feeder adds the unique advantage of producing non-agglomerated NPs, which can be packed to very high relative densities. The capabilities of the modified LAMA process allow the production of films that do not suffer from the major deleterious factors that inhibit sintering.

An experimental study of the effect of rapid thermal annealing on such films at low temperatures of 150 – 250 °C, showed very high values of densification and grain growth, and a remarkable increase in conductivity when compared to existing techniques. These results establish that the true sintering kinetics of NPs is very high and it is possible to achieve high densification and growth at low temperatures, if the deleterious factors to sintering are minimized. An evaluation of the microstructure, density and conductivity of films in the temperature range of 75-250 °C, revealed two distinct transitions - one at about 150 °C, where densification became dominant and another at about 100 °C, where coarsening became dominant. At temperatures between these two

critical values both surface diffusion and grain boundary diffusion contribute significantly to sintering.

A model was developed by fitting existing theoretical models of the dependence of conductivity on density and grain size, and models of simultaneous grain growth and densification, to our experimental data. The model was solved numerically to predict the evolution of grain size, density and conductivity as a function of annealing treatment at low temperatures. The uniqueness of the model lies in the fact that it predicts the sintering behavior of a real powder system with reasonable accuracy. Since, the experimental results represent the true sintering kinetics of NPs, it was possible to use existing sintering models to calculate the fundamental diffusion parameters. The experimental data was used to determine the effective surface diffusivity and the effective activation energy for surface diffusion of silver at low temperatures. While the accuracy of the surface diffusivity of silver is dependent on the ability of the existing models to describe surface diffusion-limited grain growth for real systems[44], we believe our analysis of activation energy for surface diffusion does not suffer from this limitation.

To study the effect of agglomeration on the sinterability of films, films were deposited at higher feed rates. Grain size, density and conductivity of as-deposited and annealed films were evaluated as a function of MP feed rate. The results showed a significant decrease in sinterability with an increase in agglomeration, suggesting that a low MP feed rate of about 10 mg/hr is essential to produce films if a high final density and conductivity is desired.

Experimental studies and theoretical considerations in this work showed that to achieve high conductivity in films it is necessary to achieve high density in films. The major conditions required to achieve high density in films are a) High initial density in films, b) Low agglomeration of particles in films, c) absence of organic capping on constituent particles, and d) an annealing treatment in the grain boundary diffusion dominated regime.

Finally, we used the LAMA setup to produce films with larger NPs and low initial relative density, using Ar as the carrier gas to do a comparative study with films with small NPs and high initial density, produced using He as the carrier gas. The results showed the superior qualities of films deposited using He as the carrier gas for applications where a high density and conductivity is desired.

Chapter 10: Future Work

The following are recommendations for future work:

1. In the present work, films were deposited at room temperature and there is considerable evidence of room temperature sintering of NPs. The films deposited in this work consisted of NPs with well-developed necks before any annealing treatment was given. Since, these necks were developed in the surface diffusion-dominant regime, the driving force for densification was reduced when the annealing treatment was later performed in the grain boundary diffusion-dominant regime. It is postulated that depositing the lines on a cold substrate and then rapidly raising the temperature above 150 °C may yield even higher conductivity lines. This deposition strategy would densify the films significantly in the initial stage of sintering and further increase the rate of densification and grain growth in the intermediate and final stages of sintering.

2. *In-situ* TEM annealing experiments of cross-sections of the as-deposited films would give insights into the actual sintering processes that occur at low temperatures. The sintering processes are complex and a non-agglomerated array of uniform sized spherical NPs provide a unique opportunity to model sintering behavior of a many particle system.

3. Gleason reported a NP synthesis technique using the laser ablation of aqueous aerosols. The silver NPs synthesized using this route were found be non-agglomerated and much easier to feed when compared to metallic MPs. From a technological point of view, it would be worthwhile to evaluate the microstructures and conductivities of films produced with this feeder and using LAMA.

4. The biggest challenge the LAMA process faces for commercialization is the low efficiency and low yield of the process. J.W. Keto has suggested that the use of larger MPs may overcome the problem of low yield[91]. Currently, the setup wastes the majority of the input laser energy. A creative use of optics might help solve the problem and increase both the efficiency and yield of the process.

Appendix A

This appendix gives the general theory and calculations done for the error analysis of the various parameters used in the developed model described in this dissertation.

Estimating the error in the fitting parameter R

Since the conductivity of the films is an arbitrary function of density and grain size, and this arbitrary function cannot be reduced to a linear form, the error in the fitting parameter R is calculated by numerically calculating (chi-square) χ^2 as a function of R. The error in R simply corresponds to an increase in χ^2 by 1^{92} . A justification of this analysis to calculate errors in least square fitting of arbitrary functions can be found in Ref [93]. Figure 55 shows the plot of χ^2 vs R obtained for this work. Note the value of reduced chi-square is close to 1, indicating a good least square fit to the data.

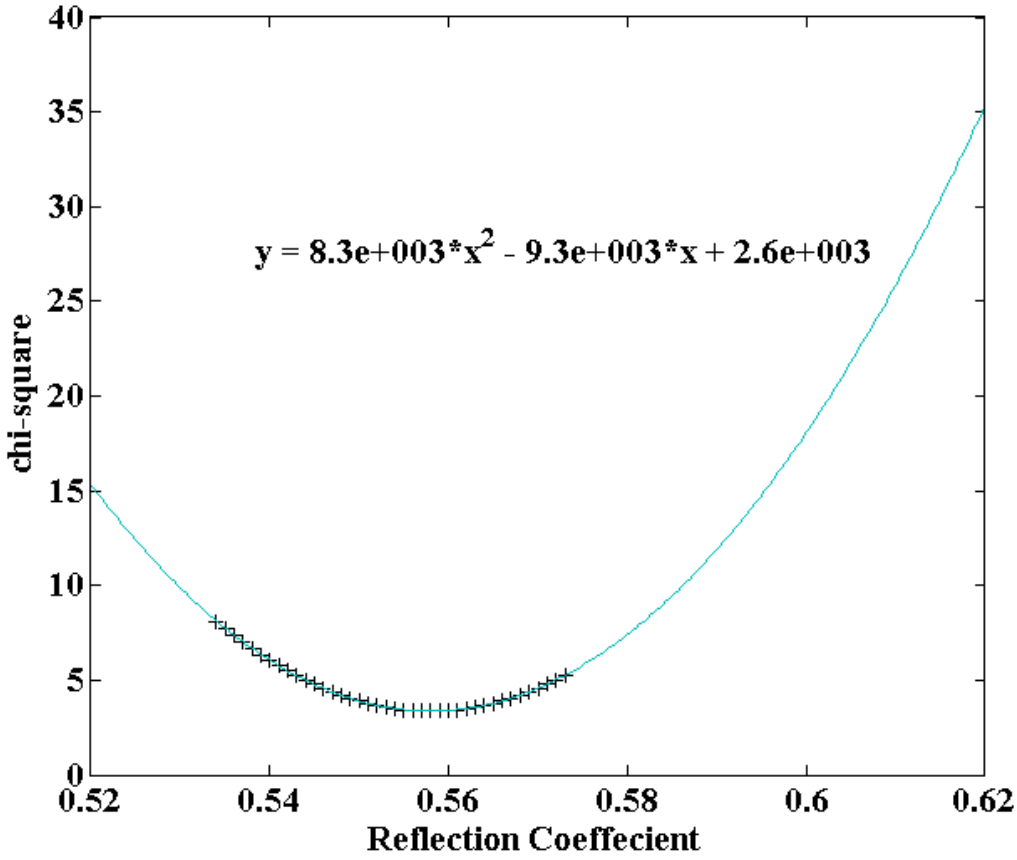

Figure 55: χ^2 vs R

R = 0.558 ± 0.0128

Calculating the error in K2

The major source of error in the value of K2 is the uncertainty in the extrapolated values of Dgb from Guy *et al.'s* work. Hoffman *et al.*[94] report the experimental data for the values of Dgb in the same temperature range as reported by Guy *et al*[33]. I estimate the error in the values of Dgb from the experimentally obtained values of log(Dgb) and fitted

values of log(Dgb), reported by Hoffman et al. σ(log(Dgb)) was found to be 0.09. Error in K2 was simply calculated using the following expression:

$$\left[\frac{\sigma(K2)}{K2}\right] = \left[\frac{\sigma(Dgb)}{Dgb}\right]$$

Calculating the error in the ratio K2.Kpre/K1

The error in the ratio K2.Kpre/K1 simply comes from the error in grain size measurement and density measurements. The error can be simply calculated by knowing the deviation in grain size measurements, density measurements and knowing the grain size – density trajectory .

Calculating the error in the pre-factor Kpre

The error in *Kpre* is calculated using the same procedure as used for calculating the error in the fitting parameter *R*. It was realized that the instrumental error in density measurements for samples that exhibited low densification was very high and not quantifiable; for this reason the sample annealed at 100 °C was omitted from the calculations of error in *Kpre*. The figure shows the plot of chi-square and Kpre for various iterations of *Kpre*.

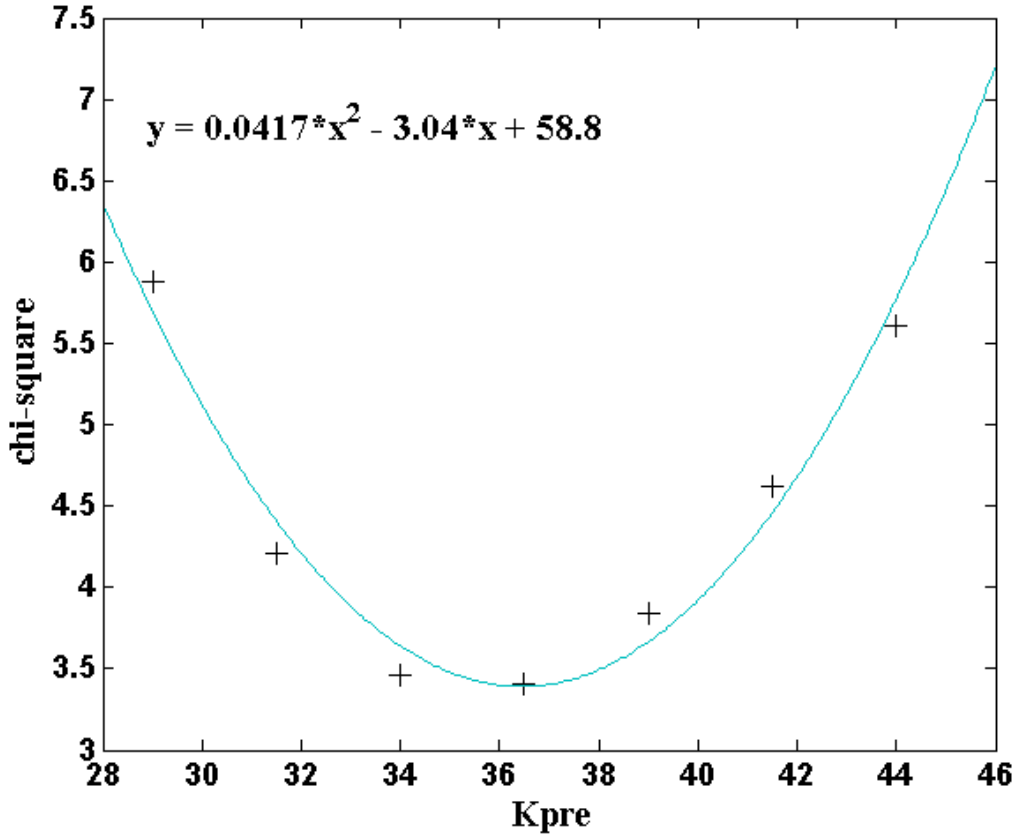

Figure 56: χ^2 vs Kpre

Kpre = 36.45 ± 4.9

Calculating the error in Ds, Do and Ea

The errorbars in the determined values of Ds can be calculated from:

$$\left[\frac{\sigma(Ds)}{Ds}\right] = \left[\frac{\sigma(K1)}{K1}\right]$$

Where the error in K1 can be estimated using

$$\left[\frac{\sigma(K1)}{K1}\right] = \left[\frac{\sigma(Kpre)}{Kpre}\right] + \left[\frac{\sigma(K2)}{K2}\right] + \left[\frac{\sigma(Kpre.K2/K1)}{Kpre.K2/K1}\right]$$

The activation energy and the pre-exponential factor Do is determined by doing a linear least-square fit of the values of ln(Ds) as a function of temperature. The error in the values of the activation energy and the pre exponential factor Do can be calculated by measuring the uncertainties in the fitted coefficients (-Ea/RT and ln(Do)).

Appendix B

This appendix gives the MATLAB codes written for the purpose of modeling in this work. There were 5 different codes that were used in this work, and are as follows:

1. To find the fitting parameter R, using the Maydas-Schatzkes equation and the Bruggeman effective medium approximation.
2. To calculate constant conductivity curves as a function of density and grain size.
3. To model the effect of heating rate on density, grain size, densification, grain growth rate, grain size-density trajectory and conductivity.
4. To model the effect of a two-step annealing treatment on density, grain size, densification, grain growth rate, grain size-density trajectory and conductivity.

The codes are divided into separate MATLAB m files and the file run.m summons the other m files in all the simulations. This is done to allow for an easy handling of codes and to give the codes the ability to shut off a particular feature if it is not desired.

Code to find the fitting parameter R:

```
% Run.m
% This m file gives the values of conductivity calculated
by Maydas-Shactzkes
```

```
% equations and Bruggeman effective medium approximation
based on the
% given grain size and desnity and the given value of R. It
also plots the
% experiemntally found values specified by the user. R is
set to 0.554
% right now.

D = [  107*10^-9 190*10^-9 238*10^-9 55*10^-9]; % grain
size from experimental data (nm)
fv = [ 0.07 0.05 0.03 0.15 ] ;   % fractional density from
experiemntal data
R = 0.554  ;    % reflection coeffecient
cond_bulk = 6.3*10^7;   % in /ohm.m
lamda = 52*10^-9;   % electron mean free path

% finding alpha in Maydas Schatzkes equation
n = 1;
for n = 1:4
alpha(n) = (lamda*(R))/(D(n)*(1-R));
n = n+1;
end
```

```
% finding grain boundary conductivity using Maydas
Schatzkes equation
n=1;
for n = 1:4
cond_gb (n) = cond_bulk*(1 - 1.5*alpha(n) + 3*alpha(n)^2 -
3*alpha(n)^3*log(1 +(1/alpha(n))));
n = n+1;
end

% finding actual conductvity using Bruggeman effective
medium approximation
n = 1;
for n = 1:4
q   % summons the m file to calcualte the roots of the
Bruggeman approximation
r = roots(p);
cond(n) = r(1)*100/cond_bulk;
n = n+1;
end
```

```
actual_cond = [47 61 71 31]; % actual conductivity from
experiments

% least square fitting. Just to check, the actual fitting
can be done by doing an iteration of hte values of R.

for n=1:4
    least (n) = (cond(n)- actual_cond(n))^2;
end

min_least = least(1) + least(2) + least(3) + least (4)  %
displays the least square fit paramter

% Sets grain size to nm
for n = 1:4
D(n) = D(n)*10^9;
n = n+1;
end

plot (D, cond, 'ko', D,actual_cond,'k+')
legend('Predicted Conductivity', 'Measured Conductivity')
xlabel('Grain Size (nm)');
```

```
ylabel ('Conductivity (% of Bulk Conductivity) ' )
cond    % displays the values of found conductivity based
on R

% q.m
% calculates the roots of the effective Bruggeman
approximation
a = fv(n);
b = 1 - fv(n);
p = [ (-2*(a/b + 1)) ((a/b)*(2-cond_gb(n)) + 2*cond_gb(n) +
1) (cond_gb(n)*(a/b))];
```

Code to find constant conductivity curves as a function of density and grain size:

```
% run.m
% finds the constant conductivity curve as a function of
density and grain
% size

cond_bulk = 6.30*10^7;  % bulk conductivity of Ag
actual_cond = 30;   % conductivity for which we want the
cosntant conductivity curve
```

```
cond = actual_cond*0.01*cond_bulk;     % converting to
percentage of bulk
lamda = 52*10^-9;    % mean free path of electron

% setting the values of grain size from 50-250 nm
n = 50;
for n=50:250
    D(n)= n*10^-9;    % grain size
    n = n+1;
end

R = 0.554  ;      % reflection coefficient

% finding alpha in Maydas Schatzkes equation
n = 50;
for n = 50:250
alpha(n) = (lamda*(R))/(D(n)*(1-R));
n = n+1;
end

% finding grain boundary conductivity using Maydas equation
n=50;
```

```
for n = 50:250
cond_gb (n) = cond_bulk*(1 - 1.5*alpha(n) + 3*alpha(n)^2 -
3*alpha(n)^3*log(1 +(1/alpha(n))));
n = n+1;
end

% Bruggeman effective medium approximation
n = 50
for n = 50:250
a(n) = (1-cond)/(1-2*cond);
b(n) = (cond_gb(n) - cond)/(cond_gb(n) + 2*cond);
fv(n) = b(n)/(b(n)+a(n));
end

% setting grain size in nm
n = 50;
for n=50:250
    D(n)= n;    % grain size
    n = n+1;
end

% setting conductivity
```

```
n = 50;
for n=50:250
    fv(n)= 100 - (100*fv(n));    % density
    n = n+1;
end

plot (D, fv, 'k')
%axis([50 250 0 0.3]);
legend('30%')
xlabel('Grain Size (nm)');
ylabel ('fv ' )
```

Code to model the effect of heating rate on density, grain size, rate of densification, grain growth rate, grain size-density trajectory and conductivity:

```
% run.m
clear all
go = 5*10^-9;    % set the intial grain size in nm
di = 0.70;  % set the initial fractional density here
variables;
initial_conditions;
density_grain_size;
```

```
conductivity;
% plot(g2,rho) % activate if you want to check what you
doing is right, the
% plot should be a straight line

% variables.m
cond_bulk = 6.3*10^7;          % in /ohm.m
lamda = 52*10^-9;    % mean free path of electrons in
background

% initial_condition.m
% this m file generates the values of the constants K1 and
K2 and sets the
% intial conditions of final temperature, initial
temperature, hodling
% time, heating rate and the time step.
% The time step is to be chosed depending on the accuracy
desired. In
% general a time step of 0.01 works for uptill 150 C. At
200 C it is
% required to use 0.001 and at 250 it is required to use
0.001. The time
```

```
% step is the step at which the code re-evalutaes all the
parameters. The
% time to run the simulation depends on the total time and
the time step.

Tf = 200 + 273 ; % final temperature in K
Ti = 200 + 273;    % initial temperature in K. Ti = Tf, for
rapid thermal annealing
heating_rate = inf ; % in kelvin per second. When set to
infinity gives the case of rapid thermal annealing.
holding_time = 300 ; % hodling time at the final
temperature in seconds
total_time = ((Tf-Ti)/heating_rate) + holding_time; % time
taken for the entire annealing treatment
t_step = 0.001; % steps at which the paramters will be
evaluated
simulation_steps = round(total_time/t_step); % total number
of simulations steps
n = 1;  % for the for loop
T(1) = Ti; % setting initial tempearture as Ti
```

```
% this loop sets the values of temperatures at all the time
steps / at all
% values of time
for n= 1:simulation_steps
    t(n) = n*t_step;
if t(n)<(total_time - holding_time);
    T(n+1)= T(n) + t_step*heating_rate;
    n = n+1;
else
    T(n+1) = Tf;
    n = n+1;
end
end

% variables for K1 and K2

Kpre = 36;  % prefactor determined by fitting
gb_energy = 0.79 % grain boundary energy in Joules/m2
sc_depth = 1 * 10^-9; % Surface depth in nm
at_vol = (10.3*10^-6)/(6.023*10^23) ;% atomic volume of the
material
k = 1.38*10^-23;    % Boltzmans constant in m2.kg.s-2.K-2
```

```
Na = 24/3.14;   % constant attached to the equation for no.
of pores
r_pore_factor = (48)^(4/3); % constant attached to the
equation for pore radius
gb_depth = 0.3*10^-9; % grain boudnary depth in nm
sc_energy = 1.14; % surface energy in Joules/m2
alpha = 2 ; % for spherical grains
Do_gb = (10)^(-4.575); % pre-factor for grain boundary
diffusion
Do_sc = (2.7182)^(-13.793); % pre-factor for surface
diffusion
Ea_gb = (4.9202*1000*k)/(0.434); % activation energy for
grain boundary diffusion
Ea_sc = 9018*k; % activation energy for surface diffusion

% setting the values of Dgb, Ds , K1 and K2

n =1;
for n = 1:(simulation_steps +1)
    Dgb(n)= Do_gb*(exp(-Ea_gb/(k*T(n))));
    Ds(n)= Do_sc*(exp(-Ea_sc/(k*T(n))));
```

```
    k1 =
(Kpre*Dgb(n)*gb_depth*sc_energy*at_vol*4)/(3*k*T(n));
    k2 =
(alpha*gb_energy*Ds(n)*sc_depth*at_vol*r_pore_factor)/(Na*3
.14*k*T(n));
    n = n+1;
end

% density_grain_size.m
% this m file generates the graphs for density, grain size,
grain growth
% rate, and densification rate. The constants used in this
file are
% generated in initial_condition.m
% the density and grain size values generated in this file
is used the
% conductivity.m to generate the graphs for conductivity vs
annealing time
% for particular temperatures.
```

```
% calculating rates of densification, grain growth, and
grain size and
% density at all time steps.

n=1;
for n =1:simulation_steps
    d(1) = di;  % setting initial density
    g(1) = go;  % setting initial grain size
    d_t(n) = (k1)/(((1-d(n))^(0.5))*(g(n)^4));  %
densification equation
    g_t(n) = (k2)/(((1-d(n))^(4/3))*((g(n)^3))); % grain
growth equation

    % In this if-else loop, only the if part will be used.
It is designed
    % to reject the values of densities if fractional
density shoots above
    % 1. However if a proper time step is used the else
part should never
    % actually be required.

    if d(n)<0.99
```

```
    d(n+1) = d(n)+ d_t(n)*t_step;
    g(n+1) = g(n) + g_t(n)*t_step;
    else
        d_t(n) = 0;
        d(n+1) = 0.99;
        g(n+1) = g(n) + g_t(n)*t_step;
    end
    t(n+1) = (n+1);
    n=n+1;
end

% setting times in seconds instead of time steps
n=1;
for n=1:(simulation_steps +1)
    t1(n) = n*t_step;
    n=n+1;
end

% setting times in seconds instead of time steps
n=1;
for n=1:simulation_steps
    t2(n) = t(n)*t_step;
```

```
    n=n+1;
end

% converting grain size in nm
n=1;
for n=1:(simulation_steps + 1);
    g1(n)=g(n)/(10^-9);
    n=n+1;
end

%%%%% the following paramters rho and g2 are not really
used. They can
%%%%% however be plotted again each other and should be a
straight line, if
%%%%% we are not making any mistakes. This is just to check
if what you are
%%%%% doing is right. a plot of rho and g2 is an indication
of K1/K2 and a
%%%%% straight line implies that K1/K2 are constants

n=1;
for n=(simulation_steps + 1);
```

```
    g2(n)=log((g(n))/(go*(10^-9)));
    n=n+1;
end
n=1;
for n=1:(simulation_steps + 1);
    rho(n)=(1-d(n))^(1/6);
    n=n+1;
end

%%%%%%

% plots density vs times
t(1) = 1;
subplot(3,3,1)
plot(t1,d),title('Density vs Time')
xlabel('t(sec)');
ylabel ('Fractional Density ' )
%axis([0 300 0.7 1])

% plots grain size vs time
subplot(3,3,2)
plot(t1,g1), title('Grain Size vs Time')
```

```
xlabel('t(sec)');
ylabel ('Grain Size (nm) ' )
%axis([1 1000 0.7 0.99])

% plots rate of densification vs time
subplot(3,3,3)
plot(t2,d_t), title('Densification vs Time')
xlabel('t(sec)');
ylabel ('Rate of Fractional Density Change (/sec) ' )

% plots grain size - density trajectory
subplot(3,3,5)
plot(d,g1),title('Grain Size - Density Trajectory');
xlabel('Fractional Density');
ylabel ('Grain Size (nm) ' )

% plots grain growth rate vs time
subplot(3,3,6)
plot(t2,g_t),title('Grain Growth Rate vs Time');
xlabel('t(sec)');
ylabel ('Grain Growth Rate (nm/s) ' )
```

```
% conductivity.m
% this m file give a plot of conductivity as a function of
time at a given
% temperature. The grain size and density required in these
plots come from
% density_grain_size.m. The file solves Maydas-Schatzkes
equation and the
% Bruggeman effective medium approximation simultaneously.

R = 0.554  ;     % reflection coeffecient

% setting values of Grain size
n=1;
for n=1:(simulation_steps + 1)
    D(n) = g(n);        % grain size
    n=n+1;
end

% calculating alpha

n = 1;
for n = 1:(simulation_steps + 1)
```

```
alpha(n) = (lamda*(R))/(D(n)*(1-R));
n = n+1;
end

% calculating grain boundary conductivity
n=1;
for n = 1:(simulation_steps + 1)
cond_gb (n) = cond_bulk*(1 - 1.5*alpha(n) + 3*alpha(n)^2 -
3*alpha(n)^3*log(1 +(1/alpha(n))));
n = n+1;
end

% calculating void fraction
n=1;
for n=1:(simulation_steps + 1)
    fv(n) = 1- d(n);        % fractional density
    n=n+1;
end

% calcualting the roots of the effective bruggeman
approximation equation.
```

```
% The for loop calls on the m film q, where the equation is
actually
% solved.
n = 1;
for n = 1:(simulation_steps + 1)
q
r = roots(p);
cond(n) = r(1);
n = n+1;
end

% actual_cond = [47 61 71 31]; %is shut off, activate if
you want to see
% the actual conductivities for comparison

% finding the values of % conductivity of bulk. I denote
cond1 as %
% conductivity of bulk
n=1;
for n=1:(simulation_steps + 1)
    cond1(n) = (cond(n)*100)/(cond_bulk);
    n=n+1;
```

```
end

% plotting conductivity vs time

subplot (3,3,4)
plot(t1,cond1)
%axis([0 30  0 100])
title('Conductivity vs Time');
xlabel('t(sec)');
ylabel ('% Conductivity of Bulk Ag ' )

% conductivity_5min = cond1(simulation_steps) % activate if
you want to see
% the final conductivity
```

Code to model the effect of a two-step annealing treatment on density, grain size, densification, grain growth rate, grain size-density trajectory and conductivity:

```
% run.m
clear all
go = 5*10^-9;% setting initial grain size
di = 0.7;    % setting intial desnity
```

```
variables;  % calling on the variables
initial_conditions; % intial conditions
density_grain_size;
conductivity;

% variables.m
cond_bulk = 6.3*10^7;         % in /ohm.m
lamda = 52*10^-9;    % mean free path of electrons in
background



% density_grain_size.m
% this m file generates the graphs for density, grain size,
grain growth
% rate, and densification rate. The constants used in this
file are
% generated in initial_condition.m
% the density and grain size values generated in this file
is used the
% conductivity.m to generate the graphs for conductivity vs
annealing time
% for particular temperatures.
```

```
% calculating rates of densification, grain growth, and
grain size and
% density at all time steps.
n=1;
for n =1:simulation_steps
    d(1) = di;
    g(1) = go;
    d_t(n) = (k1(n))/(((1-d(n))^(0.5))*(g(n)^4));
    g_t(n) = (k2(n))/(((1-d(n))^(4/3))*((g(n)^3)));

    % In this if-else loop, only the if part will be used.
It is designed
    % to reject the values of densities if fractional
density shoots above
    % 1. However if a proper time step is used the else
part should never
    % actually be required.

    if d(n)<0.99
    d(n+1) = d(n)+ d_t(n)*t_step;
    g(n+1) = g(n) + g_t(n)*t_step;
```

```
    else
        d_t(n) = 0;
        d(n+1) = 0.99;
        g(n+1) = g(n) + g_t(n)*t_step;
    end

    t(n+1) = (n+1);
    n=n+1;
end

% setting times in seconds instead of time steps
n=1;
for n=1:(simulation_steps +1)
    t1(n) = n*t_step;
    n=n+1;
end

% setting times in seconds instead of time steps
n=1;
for n=1:simulation_steps
    t2(n) = t(n)*t_step;
    n=n+1;
```

```
end

% converting grain size in nm
n=1;
for n=1:(simulation_steps + 1);
    g1(n)=g(n)/(10^-9);
    n=n+1;
end

%%%%% the following paramters rho and g2 are not really
used. They can
%%%%% however be plotted again each other and should be a
straight line, if
%%%%% we are not making any mistakes. This is just to check
if what you are
%%%%% doing is right. a plot of rho and g2 is an indication
of K1/K2 and a
%%%%% straight line implies that K1/K2 are constants

n=1;
for n=(simulation_steps + 1);
    g2(n)=log((g(n))/(go*(10^-9)));
```

```
    n=n+1;
end
n=1;
for n=1:(simulation_steps + 1);
    rho(n)=(1-d(n))^(1/6);
    n=n+1;
end

% plots density vs times
t(1) = 1;
subplot(3,3,1)
plot(t1,d),title('Density vs Time')
xlabel('t(sec)');
ylabel ('Fractional Density ' )
%axis([0 300 0.7 1])

% plots grain size vs time
subplot(3,3,2)
plot(t1,g1), title('Grain Size vs Time')
xlabel('t(sec)');
ylabel ('Grain Size (nm) ' )
%axis([1 1000 0.7 0.99])
```

```
% plots rate of densification vs time
subplot(3,3,3)
plot(t2,d_t), title('Densification vs Time')
xlabel('t(sec)');
ylabel ('Rate of Fractional Density Change (/sec) ' )

% plots grain size - density trajectory
subplot(3,3,5)
plot(d,g1),title('Grain Size - Density Trajectory');
xlabel('Fractional Density');
ylabel ('Grain Size (nm) ' )

% plots grain growth rate vs time
subplot(3,3,6)
plot(t2,g_t),title('Grain Growth Rate vs Time');
xlabel('t(sec)');
ylabel ('Grain Growth Rate (nm/s) ' )



% conductivity.m
% this m file give a plot of conductivity as a function of
time at a given
```

```
% temperature. The grain size and density required in these
plots come from
% density_grain_size.m. The file solves Maydas-Schatzkes
equation and the
% Bruggeman effective medium approximation simultaneously.

R = 0.554  ;     % reflection coeffecient

% setting values of Grain size
n=1;
for n=1:(simulation_steps + 1)
    D(n) = g(n);        % grain size
    n=n+1;
end

% calculating alpha

n = 1;
for n = 1:(simulation_steps + 1)
alpha(n) = (lamda*(R))/(D(n)*(1-R));
n = n+1;
end
```

```
% calcualting grain boundary conductivity
n=1;
for n = 1:(simulation_steps + 1)
cond_gb (n) = cond_bulk*(1 - 1.5*alpha(n) + 3*alpha(n)^2 -
3*alpha(n)^3*log(1 +(1/alpha(n))));
n = n+1;
end

% calculating void fraction
n=1;
for n=1:(simulation_steps + 1)
    fv(n) = 1- d(n);        % fractional density
    n=n+1;
end

% calculating the roots of the effective bruggeman
approximation equation.
% The for loop calls on the m film q, where the equation is
actually
% solved.
n = 1;
```

```
for n = 1:(simulation_steps + 1)
q
r = roots(p);
cond(n) = r(1);
n = n+1;
end

% actual_cond = [47 61 71 31]; %is shut off, activate if
you want to see
% the actual conductivities for comparison

% finding the values of % conductivity of bulk. I denote
cond1 as %
% conductivity of bulk
n=1;
for n=1:(simulation_steps + 1)
    cond1(n) = (cond(n)*100)/(cond_bulk);
    n=n+1;
end

% plotting conductivity vs time
```

```
subplot (3,3,4)
plot(t1,cond1)
%axis([0 30  0 100])
title('Conductivity vs Time');
xlabel('t(sec)');
ylabel ('% Conductivity of Bulk Ag ' )

% conductivity_5min = cond1(simulation_steps) % activate if
you want to see
% the final conductivity
```

References

1 Araki, T., Nogi, M., Suganuma, K., Kogure, M., Kirihara, O., "Printable and Stretchable Conductive Wirings Comprising Silver Flakes and Elastomers," Electron Device Letters, IEEE , Vol.32, No.10, pp.1424-1426, (2011)

doi:10.1109/LED.2011.2161663

2 Zhang, Z., Zhang, X., Xin, Z., Deng, M., Wen, Y., and Song, Y., "Synthesis of monodisperse silver nanoparticles for ink-jet printed flexible electronics", Nanotechnology Vol. 22 425601 (2011)

doi:10.1088/0957-4484/22/42/425601

3 Kim, D.H., Song, J., Choi, W.M., Kim, H.S., Kim, R.H., Liu, Z., Huang, Y.Y., Hwang, K.C., Zhang, Y.W., and Rogers, J.A., "Materials and Noncoplanar Mesh Designs for Integrated Circuits with Linear Elastic Responses to Extreme Mechanical Deformations" Proceedings of the National Academy of Sciences of the United States of America, Vol. 105, No. 48 pp. 18675-18680 (2008)

4 Hodgson, A., "The role of paper in the future of printed Electronics", 2nd International Workshop on Collaborating over Paper and Digital Documents, Vol. 2, 3-6 (2011)

5 Kempa, H., Trnovec, B., Stanel, M., and Huebler, A.C., "Printed Elecronics on paper", Proceedings of OEC07, 1-3, (2007)

6 Lin, C.P., Chang, C.H. , Cheng, Y.T. , and Jou, C.F., "Development of a Flexible SU-8/PDMS-Based Antenna," Antennas and Wireless Propagation Letters, IEEE , vol.10, pp.1108-1111, (2011)

doi: 10.1109/LAWP.2011.2170398

7 Judy, J.W., “Microelectromechanical system (MEMS): fabrication, design and applications”, Smart Materials and Structures, Vol. 10, 1115-1134, (2001)

8 Qin, X.Y., Zhang, W., Zhang, L.D., Jiang, L., Liu, X.J. & Jin, D. “Low-temperature resistance and its temperature dependence in nanostructured silver”, Physical Review B Vol. 56, No. 16, (1997)

9 Yamamoto, M., Kasbiwagi Y., Kakiuchi H., Tsujimoto T., Yoshida, Y, “A variety of silver nanoparticle pastes for fine electronic circuit pattern formation”, 6th International IEEE Conference on Polymers and Adhesives in Microelectronics and Photonics, Proceedings 105-109 (2007)

10 Groza, J.R., “Nanosintering”, Nanostructured Materials, Vol. 12, No. 5-8, 987-992, (1999)

11 Hu, A., Guo, J.Y., Patane, G., Zhou, Y., Compagnini, G., and Xu,.X..C., :Low temperature sintering of Ag nanoparticles for flexible electronics packaging”, Applied Physics Letters, Vol. 97, 153117, (2010)

12 Coatanéa, E., Kantola, V., Kulovesi, J., Lahti, L., Lin, R., & Zavodchikova, M., “Printed Electronics, Now and Future”, In Neuvo, Y., & Ylönen, S. (eds.), Bit Bang – Rays to the Future. Helsinki University of Technology (TKK), MIDE, Helsinki University Print, Helsinki, Finland, 63-102.(2009)

13 Lee, H., Chou, K.S., and Huang. K.C., “ Inkejet printing of nanosized silver colloids”, Nanotechnology, Vol. 16, 2436-2441 (2005), doi:10.1088/0957-4484/16/10/074

14 Piner, R. D.; Zhu, J.; Xu, F.; Hong, S.; Mirkin, C. A. "Dip Pen Nanolithography," Science, Volume. 283, 661-663 (1999)

15 Lebedev, M. , Akedo, J., Mori, K. and Eiju, T., "Simple self-selective method of velocity measurement for particles in impact-based deposition," Journal of Vacuum Science Technology A, Vol. 18, 563-566, (2000).

16 Rida. H. A, Conductive Inkjet Printed antennas on flexible low cost paper base substrates for RFID and WSN applications, Dissertation, Georgia Institute of Technology 2009

17 Ginger, D.S., Zhang, H., Mirkin, C.A., "The Evolution of Dip-Pen Nanolithography". Angewandte Chemie, Vol. 43, No.1, 30-45, (2003)

18 Piner, R. D.; Zhu, J.; Xu, F.; Hong, S.; Mirkin, C. A. "Dip Pen Nanolithography," Science, Vol. 283, 661-663, (1999)

19 Sourabh S.K and Culpepper, M.L. Characterization of the dip pen nanolithography process for nanomanufacturing. Journal of Manufacturing Science and Engineering. Vol. 133, No.4, 041005, (2011)

20 Kashu, S., Fuchita, I., Manabe, T., and Hayashi, C. "Deposition of ultra fine particles using a gas jet", Journal of Applied Physics, Vol. 23, 910-912, (1984).

21 Oda, M.; Fuchita, E.; Tsuneizumi, M.; Kashu, S.; Hayashi, C. Gas deposition films of ultra fine particles Nanostructured Materials Vol. 1, 203-206 (1991)

22 Hayashi, C.; Kashu, S.; Oda, M.; Naruse, F. Use of nanoparticles as coatings 12th International Vacuum Congress, Oct 12-16 1992 Materials Science & Engineering A: Structural Materials: Properties, Microstructure and Processing A163, 157-161, (1993).

23 Becker, M. F. , Brock, J. R. , and Keto, J. W. , U.S. Patent No. 5 585 020, December 17, (1996)

24 Albert, A., "Nanostructured Ag produced by LAMA", Dissertation, The University of Texas at Austin (2007)

25 Huang, C.," Supersonic Deposition of Laser Ablated Silver Nanoparticles for Mesoscale Structures", Dissertation, The University of Texas at Austin (2006)

26 Gleason, K., "Engineering Nanocomposite Polymer Membranes for Olefin/Paraffin Separation", Dissertation, The University of Texas at Austin (2011)

27 Plombon, J.J., Andideh, E., Dubin, V.M., and Maiz, J. "Influence of phonon, geometry, impurity, and grain size on Copper line resistivity", Applied Physics Letters, Vol. 89, 113124-113127, (2006)

28 Sondeimer, E.H., The influence of a Transverse Magnetic Field on the Conductivity of Thin Metallic Films, Physics Review, Vol 80. 401-406 (1950)

29 Maydas, A.F., and Shatzkes, M., "Electrical-Resistivity Model for Polycrstalline Films: the Case of Arbitrary Reflection at External Surfaces", Physical Review B, Vol 1. No. 4, (1970)

30 Choy, T.C. (1999). Effective Medium Theory. Oxford: Clarendon Press. ISBN 978-0-19-851892-1

31 Song, P., and Wen, D., “Molecular dynamics simulation of sintering of metallic nanoparticles” Journal of Nanoparticle Research, Vol. 12 Issue 3, p823-829 (2010)DOI 10.1007/s11051-009-9718-7

32 Lenel, F.V., “Mechanism of material transport in sintering”, Powder Metallurgy and Metal Ceramics, Vol. 3, 6, 523-529 (1964)

33 Guy, A.G., “The Essentials of Materials Science”, McGraw-Hill, New York (1976)

34 Winegrad, W.C., Chalmers, B., “Self-Diffusion at Silver Surfaces”, Canadian Journal of Physics, Vol. 30, (1952)

35 Rhead, G.E., “Surface self-diffusion of silver in various atmospheres”, Acta Metallurgical, Vol. 13, 223-236, (1965)

36 Hough, R.R., :An invrestigation of the surface self diffusion coefficient of pure copper and silver by grain boundary grooving technique”, Scripta Metallurgica, Vol. 4, 559-562, (1970)

37 Shewmon, P., “Diffusion in Solids”, The Minerals, Metals and Materials Society, Warrendale, PA (1989)

38 Yaws, C.L., Nijhawan, S., and Bu, L., “Handbook of Vapor Pressure”, Gulf Publishiing Co., Houston, Texas (1994)

39 Carlton, C.E., Rabenberg, L. and Ferreira, P.J., “On the Nucleation of Partial Dislocations in Nanoparticles” , Phil. Mag. Let. Vol. 88, 715-724 (2008).

40 Kuczynski, G.C.,"Self-diffusion in sintering of metallic particles", Transactions of AIME,, Vol. 85, 169 - 178 (1949)

41 Bruke, J.E., "Role of Grain Boundaries in Sintering", The Journal of American Ceramic Society, Vol. 40, No. 3, 80-85, (1957)

42 Coble, R.L, "Initial sintering of Alumina and Haematite", Journal of American Ceramic Society, Vol. 41, 55 (1958)

43 Exner, H.E., and Arzt, E., "Sintering Processes", Physical Metallurgy, 3rd enition, Elsevier Science Publishers BV, Amsterdam, Chapter 30, pp 1885-1912, (1983)

44 Johnson, L.D., "Solid state sintering models", Materials Science Research, Vol 13, Plenum Press, new York and London, pp 97 – 107 (1979)

45 Kuczynski, G.C., "Model Experiments and the Theory of Sintering", 4th International Symposium of Science and Technology of Sintering, Tokyo, Japan, 4-6, (1987)

46 Kang, S.J.L., "Sintering: densification, grain growth and microstructure", Elseview Butterworth-Heinemann, Oxford (2005)

47 Coble, R.L., "Sintering Crystalline Solids. I. Intermediate and Final State Diffusion Models", Journal of Applied Physics, Vol. 32, No. 5, 787-92, (1961)

48 Yan, M.F., Cannon, R.M., Chowdhry, U. and Bowen,K.., "Effect of grain size distribution on sintered density", unpublished research, Bell Laboratories, Murray Hill, NJ, (1980)

49 Greskovich, C., and Lay, K.W., "Grain growth in very porous Al2O3 compacts", Journal of American Ceramic Society, Vol. 55, No.3, (1972)

50 Rahaman, M.N., “Ceramic Processing and Sintering”, Marcel Dekker, Inc., New York, USA (2003)

51 Annamalai, A.R., Upadhaya, A., and Agarwal, D., “ Effect of heating mode on sintering of ferrous compacts through powder metallurgy route”, International Heat Treatment and Surface Engineering, Vol. 5, No. 4, (2011)

52 Kodash, V.Y., Groza, J.R., Cho, K.C., Klotz, B.R., Dowding, R.J., “Field-assisted sintering of Ni nanopowders”, Materials Science and Engineering A, Vol. 385, 367-371, (2004)

53 Xu, G, Lloyd, I.K., Olorunyolemi, T., Carmel, Y., Wilson, O.C., “Microwave sintering of ZnO at ultra high heating rates”, Journal of Materials Research, Vol. 16, No. 10, (2011)

54 Herring, C., “Effects of Change of Scale on Sintering Phenomena”, Journal of Applied Physics, 21, 301–3 (1950)

55 German, R.M., “Prediction of sintered density for bimodal powder mixtures”, Metallurgical Transactions A, Vol. 23 A, 1458, (1992)

56 Liu, D.M, Ling, J.T., Tuan, W.H., “Interdependence between green compact property and powder agglomeration and their relation to the sintering behavior of zirconia powder”, Ceramics International, Vol. 25, 551-559, (1999)

57 Ring, T.A.,”Fundamentals of Ceramic Powder Processing and Synthesis” ISBN: 978-0-12-588930-8

58 Stanciu, L.A., Kodash, V.Y., and Groza, J.R., " Effects of Heating Rate on Densification and Grain Growth during Field-Assisted Sintering of Al2O3 and MoSi2 Powders", Metallurgica and Materials Transactions A, Vol. 32A, 2633, (2001)

59 Lakshminarayana, P., Manga, K.K., Cao, H.D., Loh, K.P. & Xu, "Q.H. Preparation of Conductive Silver Films at Mild Temperatures for Printable Organic Electronics." Chemistry of Materials, Vol. 23, 3273–3276 (2011)

60 Huang, C., Nichols, W.T., O'Brien, D.T., Becker, M.F., Kovar, D. and Keto, J.W., "Supersonic Jet Deposition of Silver Nanoparticle Aerosols: Correlations of Impact Conditions and Film Morphologies," Journal of Applied Physics Vol. 101, 064902 (2007)

61 Huang, C., Becker, M.F., Keto, J.W., and Kovar, D. "Annealing of Nanostructured Silver Films Produced by Supersonic Deposition of Nanoparticles," Journal of Applied Physics, Vol. 102, 054308 (2007)

62 Malyavanatham, G., O'Brien,D.T., Becker, M.F., Nichols, W.T., Keto,J.W., Kovar,D, Euphrasie, S., Loue, T. and Pernod, P., "Thick films fabricated by laser ablation of PZT microparticles" Journal of Materials Process Technology Vol. 168, No. 2, 273-279, (2005)

63 Ma,J., Becker, M.F., Keto, J.W. and Kovar, D., "Compositional and Microstructural Evolution During Annealing of Terfenol-D Nanoparticulate Films, Journal of Materials Research, Vol. 26, No. 20, 2672-2681 (2011)

64 Chen, B. T. and Yeh, H. C., "An improved virtual impactor: Design and performance," Journal of Aerosol Science, Vol. 18, pp. 203-214, (1987)

65 W. T. Nichols, "Production and controlled collection of nanoparticles toward manufacturing of nanostructured materials," Ph.D. dissertation, Physics, The University of Texas, Austin, TX, (2002).

66 Private communications with Benedikt Biechele.

67 C. Huang, W. T. Nichols, D. T. O'Brien, M. F. Becker, J. W. Keto, and D. Kovar, J. Appl. Phys. 101, 064902 2007.

68 National Institutes of Health (2004), Retrieved Jan. 2007 from http://rsbweb.nih.gov/ij/

69 Henneke, D.E, Malyavanatham, G, Kovar, D., Nichols, W.T., Keto, J.W., O'Brien, D.T., and Becker, M.F, "Stabilization of Silver Nanoparticles in Nonanoic Acid: A Temperature Activated Conformation Reaction Observed with Surface Enhanced Raman Spectroscopy," Journal of Chemical Physics, Vol. 119, No. 13, 6802-6809 (2003)

70 Private Communications with Becker, M.F., Department of Electrical and Computer Engineering, The University of Texas at Austin

71 Davis, C, " An Electrostatic Approach for Producing Nanoparitculate Membranes using Laser Ablation of Microparticles", Master's Thesis, The University of Texas at Austin (2011)

72 Wakuda, D. et al., "Novel method for room temperature sintering of Ag nanoparticle paste in air," Chemical Physics Letters, Vol. 441, pp. 305-308 (2007)

73 A. P. Weber and S. K. Friedlander, "In situ determination of the activation energy for restructuring of nanometer aerosol agglomerates," Journal of Aerosol Science, Vol. 28, pp. 179-192, 1997.

74 Schwartz, G.C., Srikishnan, K.V., “Handbook of Semiconductor Interconnection Technology”, CRC Press, Taylor and Francis Group, Boca Raton, FL, p. 89, (2006)

75 Lee, H.H., Chou, K.S., Huang, K.C.,” Inkjet printing of nanosized silver colloids:, Nanotechnology, Vol. 16, 2436-2441 (2005)

76 Artunc, N., Bilge, M.D., Utlu, G., “The effects of grain boundary scattering on the electrical resistivity of single-layered silver and double-layered silver/chromium thin films”, Surface and Coating Technology, Vol. 201, 8377-8381, (2007)

77 Vancea, J., Pukowietz, S., Reiss, G., and Hoffman, H., Physical Review. B35, 9067, (1987)

78 Cao, G., “Nanostructures and Nanomaterials”. Imperials College Press, (2004)

79 Kittel, C., “Introduction to Solid State Physics”, 5th edition, Wiley, New York, (1976)

80 Brook, R.J., “Ceramic Fabrication Processes: Vol 9”, In Treatise of Materials Science and Technology, New York p 331-364, (1976)

81 Handwerker, C.A., “Sintering and Grain Growth of MgO”, Dissertation, Massachusetts Institute of Technology (1978)

82 MATLAB 6.1, The Mathworks Inc., Natick, MA, 2000

83 Seipenbusch, M., Rothenbacher, S., Wever, A.P., and Kasper, G., “Interparticle forces in nanoparticle Agglomerates”, European Aerosol Conference 2007

84 Seipenbusch, M., Toneva, P., Peukert, W., Weber,A.P., “Impact fragmentation of Metal Nanoparticle Agglomerates”, Particle and Particle Systems Characterization, Vol. 24, 193-200 (2007)

85 German, R.M., “Particle Packing Characteristics”, Metal Powder Industries Federation, Pinceton, new Jersey (1989)

86 Liu, D.M., “Interdependence between green compact property and powder agglomeration and their relation to the sintering behavior of zirconia powder”, Ceramics International, Vol. 25, 551-599 (1999)

87 Oh, K.S., Kim, D.Y., Cho, S.J, “Generation of crack like voids during sintering of Al2O3-10ZrO2 ceramics and their prevention by presintering with low pressure (2Mpa)”, Journal of Americal Ceramic Society ,Vol. 79, No. 9, 1723-1725 (1996)

88 Vekatachari, K.R., Raj, R., “Shear Deformation and Densification of Powder Compacts”, Journal of the American Ceramic Society, Vol. 69, No. 9, 499-506 (1986)

89 Lehtinen, K.E.J., “Theoretical studies on aerosol agglomeration processes”, Dissertation, Technical Research Centre of Finland (1997)

90 Matsoukas, T., Friedlander, S.K., “Dynamics of aerosol agglomerate formation”, Journal of colloid and interface science, Vol. 146, No. 2, 495-506, (1991)

91 Private communications with Dr. John W. Keto

92 Bevington, P.R., “Data Reduction and Error Analysis for Physical Sciences”, Mc-Graw Hill Book Company, New York (1969)

93 Arndt, R.A., and Malcolm, H., "Nucleon-Nucleon Phase Shift Analyses by Chi-Squared Minimization", Methods in Computational Physics, Academic Press Inc., New York, Vol. 6., pp 253-296. (1996)

94 Hoffman, R.E., and Turnbull, D., "Lattice and Grain Boundary Diffusion in Silver", Journal of Applied Physics, Vol. 22, pp. 634 (1951)

Vita

Manuj Nahar (Manu), son of Sunita Nahar and Narendra Kumar Nahar, was born in Jodhpur, Rajasthan, India on November 3rd, 1985. He obtained his Bachelor of Technology in Materials Science and Metallurgical Engineering from Indian Institute of Technology Madras, Chennai in June 2007. He started his Master's program in Materials Science and Engineering at the University of Texas at Austin in September 2007 and continued for a Ph.D. degree under the supervision of Dr. Desiderio Kovar.

Email Address: nahar.manuj@gmail.com

This dissertation was typed by the author.